

# THÈSE

UNIVERSITE DE PAU ET DES PAYS DE L'ADOUR  
École doctorale Sciences Exactes et leurs applications

Présentée et soutenue le 19 juin 2015  
par Maria Luisa BRAUNGER

pour obtenir le grade de docteur  
de l'Université de Pau et des Pays de l'Adour  
Spécialité : Doctorat en Chimie des Polymères

## FABRICATION ET CARACTERISATIONS ELECTRIQUES DE FILMS MINCES POUR LES CELLULES SOLAIRES ORGANIQUES

### MEMBRES DU JURY

#### RAPPORTEURS

- Roberto Koji ONMORI
- Henrique DE SANTANA

Professeur / Universidade de São Paulo  
Professeur / Universidade Estadual de Londrina

#### EXAMINATEURS

- Carlos Frederico DE OLIVEIRA GRAEFF
- Roger C. HIORNS

Professeur / Universidade Estadual Paulista  
Chargé de Recherches / Université de Pau et des Pays de l'Adour

#### DIRECTEURS

- Clarissa DE ALMEIDA OLIVATI
  - Christine DAGRON-LARTIGAU
- l'Adour

Professeur / Universidade Estadual Paulista  
Maître de Conférences/HDR / Université de Pau et des Pays de



International joint supervision of thesis

UNIVERSIDADE ESTADUAL PAULISTA “JÚLIO DE MESQUITA FILHO”

Programa de Pós-graduação em Ciência e Tecnologia de Materiais

and

UNIVERSITÉ DE PAU ET DES PAYS DE L’ADOUR

Ecole Doctorale Sciences Exactes et leurs Applications

Maria Luisa Braunger

FABRICATION AND ELECTRICAL CHARACTERIZATION OF SOLAR CELLS FROM  
ORGANIC THIN FILMS

Brazilian supervisor: Prof. Dr. Clarissa de Almeida Olivati

French supervisor: Dr. Christine Dagron-Lartigau

2015

UNIVERSIDADE ESTADUAL PAULISTA “JÚLIO DE MESQUITA FILHO”

Programa de Pós-graduação em Ciência e Tecnologia de Materiais

Maria Luisa Braunger

**FABRICAÇÃO E CARACTERIZAÇÃO ELÉTRICA DE CÉLULAS  
SOLARES A PARTIR DE FILMES FINOS ORGÂNICOS**

PRESIDENTE PRUDENTE

2015

Maria Luisa Braunger

Fabricação e caracterização elétrica de células solares a partir de filmes finos orgânicos

Tese apresentada como requisito à obtenção do título de Doutora à Universidade Estadual Paulista "Júlio de Mesquita Filho" - Programa de Pós-Graduação em Ciência e Tecnologia de Materiais, sob a orientação da Profa. Dra. Clarissa de Almeida Olivati e co-orientação do Prof. Dr. Carlos José Leopoldo Constantino.

Presidente Prudente

2015

Braunger, Maria Luisa.

Fabricação e caracterização elétrica de células solares a partir de filmes finos orgânicos / Maria Luisa Braunger, 2015  
120 f. : il.

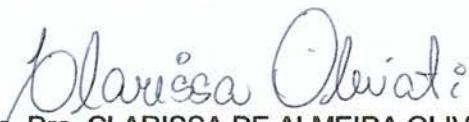
Orientador: Clarissa de Almeida Olivati

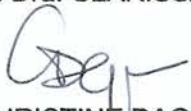
Tese (Doutorado)- Universidade Estadual Paulista. Faculdade de Ciências e Tecnologia, Presidente Prudente, 2015

1. Politiofeno. 2. Langmuir-Schaefer. 3. Medidas elétricas. 4. Dispositivo fotovoltaico orgânico. I. Universidade Estadual Paulista. Faculdade de Ciências e Tecnologia. II. Título.

**ATA DA DEFESA PÚBLICA DA TESE DE DOUTORADO DE MARIA LUISA BRAUNGER, DISCENTE DO PROGRAMA DE PÓS-GRADUAÇÃO EM CIÊNCIA E TECNOLOGIA DE MATERIAIS, DO(A) FACULDADE DE CIÊNCIAS DE BAURU.**

Aos 19 dias do mês de junho do ano de 2015, às 09:00 horas, no(a) Sala de videoconferência - FUNDACTE, reuniu-se a Comissão Examinadora da Defesa Pública, composta pelos seguintes membros: Profa. Dra. CLARISSA DE ALMEIDA OLIVATI do(a) Departamento de Física, Química e Biologia / Faculdade de Ciências e Tecnologia de Presidente Prudente, Dr. CHRISTINE DAGRON-LARTIGAU do(a) Institut Des Sciences Analytiques Et de Physico-Chimie Pour L'Environnement Et Les Matériaux / Université de Pau Et Des Pays de L'Adour, Prof. Dr. ROBERTO KOJI ONMORI do(a) Escola Politécnica / Universidade de São Paulo, Prof. Dr. CARLOS FREDERICO DE OLIVEIRA GRAEFF do(a) Departamento de Física / Faculdade de Ciências de Bauru, Prof. Dr. HENRIQUE DE SANTANA do(a) Departamento de Química / Universidade Estadual de Londrina, sob a presidência do primeiro, a fim de proceder a arguição pública da TESE DE DOUTORADO de MARIA LUISA BRAUNGER, intitulada "Fabricação e caracterização elétrica de células solares a partir de filmes finos orgânicos". Após a exposição, a discente foi arguida oralmente pelos membros da Comissão Examinadora, tendo recebido o conceito final: APROVADO. Nada mais havendo, foi lavrada a presente ata, que, após lida e aprovada, foi assinada pelos membros da Comissão Examinadora.

  
Profa. Dra. CLARISSA DE ALMEIDA OLIVATI

  
Dr. CHRISTINE DAGRON-LARTIGAU

  
Prof. Dr. ROBERTO KOJI ONMORI

  
Prof. Dr. CARLOS FREDERICO DE OLIVEIRA GRAEFF

  
Prof. Dr. HENRIQUE DE SANTANA

*To my grandmother Gertha Margarida Braunger,  
who saved my first child painting in a styrofoam board.*

*I'm sure, she would be very proud.*

## Acknowledgments

I would like to leave here my sincere acknowledgment to all those who, directly or indirectly contributed to the development of this PhD research. In particular, I would like to thank:

My Brazilian supervisor Prof. Dr. Clarissa de Almeida Olivati, who I followed from Rio Claro to Presidente Prudente to start a research in a new area for me, for the guidance and friendship.

My French supervisor Dr. Christine Dagron Lartigau for accepting to guide a physicist girl in a chemistry lab, for always being optimistic about hard tasks. *Merci!*

My Brazilian co-supervisor Prof. Dr. Carlos J. L. Constantino for the advices and help making critical decisions.

My research group (LOFF – UNESP) and especially Edilene Assunção da Silva, my friend inside and outside of the lab.

Prof. Dr. Marystela Ferreira for the use of the cyclic voltammetry technique and to Dr. Anerise Barros for the support during these measurements and friendship.

The DFQB (UNESP) members, especially the groups: LaDSOr, Noix and LLuMeS, my “neighbors” in the DFQB 2 building.

All the EPCP group (IPREM – UPPA), in especial to Dr. Hussein Awada without whom I would not have succeed with my internship project.

All the friends I made when I was in France, especially the ones from international scientific exchange programs, who made me feel closer to my home.

Prof. Dr. Carlos F. O. Graeff and Dr. Felipe J. Pavinatto for the valuable advices and corrections in the “*Exame geral de qualificação*”.

Dr. Priscila Alessio and José Diego Fernandes for the collaboration in the use of the organic macromolecules we have characterized together.

Dr. Debora T. Balogh and Bruno B. M. Torres for the perylene derivative used at the beginning of this research and for the support in the profilometry and photoluminescence measurements.

The *Laboratório Nacional de Nanotecnologia* (LNNano/CNPEN – Brazil) for providing interdigitated electrodes, especially Maria Helena de Oliveira Piazzetta and Ângelo Luiz Gobbi.



Prof. Dr. Henrique de Santana, Prof. Dr. Roberto Koji Onmori, Prof. Dr. Carlos F. O. Graeff and Dr. Roger Hiorns for the valuable advices and corrections for the final version of this thesis.

My family, my parents Bruno and Aidê, my siblings Matias and Helena and my fiancé Igor, for everything. You are my solid ground.

FAPESP and CAPES/Cofecub for the financial support.

*“My life experience tells me that  
when you don't find blacks, when you don't find women in the sciences,  
I know that these forces are real.  
And I had to survive them in order to get where I am today.”*

*Neil DeGrasse Tyson*

**BRAUNGER, M. L. Fabrication and electrical characterization of solar cells from organic thin films.** 2015. 120pp. Thesis (PhD in Science and Technology of Materials) - UNESP and (PhD in Polymer Chemistry) - UPPA, Presidente Prudente, 2015.

## **ABSTRACT**

In the area of organic photovoltaics, there is a continuous effort to improve the efficiency of the devices. In order to reach this goal, it is necessary to evaluate the characteristics that influence their performance. Although thin films of conjugated polymers (polythiophene derivatives and low bandgap polymers) have been widely investigated for applications in photovoltaic devices, few studies relate the influence of the nanostructuring of the films in such devices. In this context, the general objective of this work was to analyze the influence of deposition technique of thin films of polythiophene derivatives in organic photovoltaic devices. The Langmuir-Schaefer (LS) technique was compared to the more common spin-coating. The polythiophene films were characterized by electrical transport measurements (current vs. voltage, photoconductivity, cyclic voltammetry and impedance spectroscopy), optical spectroscopy (UV-visible and fluorescence) and morphological techniques (atomic force and Brewster angle microscopies, and profilometry). From the direct current electrical measurements, it could be observed that the LS films are more conducting than the spin-coating ones. From the morphologic point of view, the deposition technique revealed itself to influence on the photovoltaic device's performance, due to the organization and nanostructuring provided by the LS technique. Preliminary studies were also undertaken on thin films made of low bandgap polymers based on cyclopentadithiophene by using the Langmuir-Blodgett technique.

Keywords: polythiophene, Langmuir-Schaefer, electrical measurements, organic photovoltaic device.

**BRAUNGER, M. L. Fabricação e caracterização elétrica de células solares a partir de filmes finos orgânicos.** 2015. 120f. Tese (Doutora em Ciência e Tecnologia de Materiais) - UNESP e (Doutora em Química de Polímeros) - UPPA, Presidente Prudente, 2015.

## **RESUMO**

Na área de fotovoltaicos orgânicos há um esforço contínuo no aumento da eficiência dos dispositivos. Para alcançar esse objetivo, é necessária a avaliação das características que influenciam seu desempenho. Embora filmes finos de polímeros conjugados (derivados do politiofeno e polímeros de baixo bandgap) tenham sido amplamente estudados para aplicação em dispositivos fotovoltaicos, são encontrados poucos estudos investigando a influência da nanoestruturação dos filmes nestes dispositivos. Dentro deste contexto, o objetivo geral deste trabalho foi analisar a influencia da técnica de deposição de filmes finos de derivados do politiofeno em um dispositivo fotovoltaico orgânico. Para isto utilizamos a técnica de Langmuir-Schaefer (LS) em comparação à técnica spin-coating comumente utilizada. Os filmes de politiofeno foram caracterizados por medidas de transporte elétrico (corrente vs. tensão, fotocondutividade, voltametria cíclica e espectroscopia de impedância), espectroscopia óptica (UV-visível e fluorescência) e técnicas morfológicas (microscopias de força atômica e de ângulo de Brewster, e perfilometria). Através das medidas elétricas em corrente contínua observou-se que os filmes LS apresentam maior condutividade elétrica quando comparados com filmes spin-coating. Do ponto de vista morfológico, a técnica de deposição utilizada mostrou ter influencia no desempenho do dispositivo fotovoltaico, devido à organização e nanoestruturação provida pela técnica LS. Estudos preliminares foram também realizados em filmes finos de polímeros de baixo bandgap baseados em ciclopentaditiofeno usando a técnica de Langmuir-Blodgett.

Palavras-chave: politiofeno, Langmuir-Schaefer, medidas elétricas, dispositivo fotovoltaico orgânico.

**BRAUNGER, M. L. Fabrication et caractérisations électriques de films minces pour les cellules solaires organiques.** 2015. 120f. Thèse (Docteur en Science et Technologie de Matériaux) - UNESP et (Docteur en Chimie des Polymères) - UPPA, Presidente Prudente, 2015.

## **RÉSUMÉ**

Dans le domaine du photovoltaïque organique, il y a un effort continu pour améliorer l'efficacité des dispositifs. Afin d'atteindre cet objectif, il est nécessaire d'évaluer les caractéristiques qui influencent leur performance. Bien que les films minces de polymères conjugués (dérivés de polythiophène et polymères à faible bande interdite) aient été largement étudiés pour des applications dans des cellules photovoltaïques, peu d'études concernent l'influence de la nanostructuration des films dans de tels dispositifs. Dans ce contexte, l'objectif général de ce travail était d'analyser l'influence de la technique de dépôt de couches minces de dérivés de polythiophène dans des dispositifs photovoltaïques organiques. La technique de dépôt de Langmuir-Schaefer (LS) a été comparée à celle de spin-coating, plus fréquente. Les films de polythiophène ont été caractérisés par des mesures de transport électrique (courant-tension, photoconductivité, voltampérométrie cyclique et spectroscopie d'impédance), spectroscopies optique (UV-visible et fluorescence) et des techniques morphologiques (à force atomique et techniques de microscopie à angle de Brewster, et profilométrie). A partir des mesures électriques à courant continu, il peut être observé que les films LS sont plus conducteurs que ceux obtenus par spin-coating. D'un point de vue morphologique, il s'avère que la technique de dépôt influence la performance du dispositif photovoltaïque, en raison de l'organisation et de la nanostructuration fournies par la technique de la LS. Une étude préliminaire a également été réalisée sur des films de polymères à faible bande interdite à base de cyclopentadithiophène, réalisés par la technique de Langmuir-Blodgett.

Mots-clés: polythiophène, Langmuir-Schaefer, mesures électriques, cellule photovoltaïque organique.

## LIST OF FIGURES

Figure 1: Schematic diagram of the heterojunction types in an OPV device: (a) planar heterojunction and (b) BHJ. Adapted from <sup>59</sup> .....	28
Figure 2: Characteristic <i>J</i> vs. <i>V</i> curve for a photovoltaic device. ....	29
Figure 3: Molecular structure for the BuPTCD. ....	31
Figure 4: Structural formula for fullerene-C <sub>60</sub> . Image from <sup>67</sup> . ....	31
Figure 5: Condensed structural formula for the regioregular alkyl-substituted polythiophene derivatives. ....	32
Figure 6: Molecular structure of the low-bandgap polymers (a) PCPDTBT and (b) PDTSTBT. ....	33
Figure 7: Molecular structure of 4 <i>H</i> -cyclopenta[2,1- <i>b</i> :3,4- <i>b'</i> ]dithiophene (CPDT). ....	34
Figure 8: Synthesis route of 4,4-bis(2-ethylhexyl)-2,6-bis(trimethylstannyl)-4 <i>H</i> -cyclopenta[2,1- <i>b</i> :3,4- <i>b'</i> ]dithiophene, CPDT branched chains derivative. ....	34
Figure 9: (a) The NMR analysis allows for the deducing of the molecular structure of the compounds obtained at each of the steps of the monomer synthesis route, (b) part of the Bruker UltraShield 400 Magnet NMR instrument and (c) some NMR tubes with different products inside dissolved in CDCl <sub>3</sub> . ....	35
Figure 10: (a) experimental apparatus for chemical reaction using liquid nitrogen and (b) time of dropwise addition of thiophene-3-carboxaldehyde. ....	36
Figure 11: (a) removal of the solvent using the rotary evaporator system and (b) solid product obtained after recrystallization procedure. ....	37
Figure 12: (a) experimental apparatus for the chemical reaction using the reflux system and (b) filtering the remaining Cu after the reaction. ....	37
Figure 13: (a) experimental apparatus for the chemical reaction at 180 °C and (b) resulting product left under vacuum after removal of the solvent by the rotary evaporator system. ....	38
Figure 14: Polymerization reaction (a) before and (b) after heating and (c) the resulting polymer, PCPDTBT, precipitated in methanol. ....	39
Figure 15: (a) experimental apparatus for the Soxhlet extraction, (b) reduction in volume of the chloroform soluble fraction using the rotary evaporator system and (c) filtering the clean polymer PCPDTBT after precipitation in methanol. ....	40
Figure 16: TGA thermogram of PCPDTBT. ....	41
Figure 17: $\pi$ -A isotherm obtained for stearic acid and its chemical structural formula shown in details. ....	44

Figure 18: Langmuir-Blodgett deposition scheme for amphiphilic molecules. ....	45
Figure 19: Langmuir-Schaefer deposition scheme for amphiphilic molecules. ....	46
Figure 20: Langmuir film of P3HT derivative in the solid phase at 20 mN/m, indicating a region of lack of material due to previous deposition of LS film.....	47
Figure 21: AFM image of the ITO substrate, where films were deposited for morphological analysis. ....	50
Figure 22: Electrochemical cell and experimental setup for CV measurements.....	51
Figure 23: Impedance $Z^*$ plotted as a planar vector using rectangular and polar coordinates.	52
Figure 24: (a) Common RC parallel circuit and (b) its corresponding impedance plane.....	55
Figure 25: Experimental apparatus used to carry out electrical measurements in dark and under illumination of the halogen lamp of 150 mW/cm <sup>2</sup> power. ....	58
Figure 26: Experimental apparatus used to carry out photovoltaic measurements in dark and under illumination of the Oriel VERASOL solar simulator (100 mW/cm <sup>2</sup> – AM 1.5).....	59
Figure 27: Schematic representation of an interdigitated electrode being $N = 10$ digits, height $h$ , length $L$ and $w$ the width of digits. ....	60
Figure 28: (a) Photoaligner used to expose the photoresist to UV light. (b) Metal film deposited onto the glass substrates, with patterns previously formed by the presence of the photoresist.....	61
Figure 29: Lift-off step under acetone, to remove the photoresist and metal film, the last process of the fabrication of the IDE.....	62
Figure 30: Schematic view of an ITO/film/Al, showing how the electrical contacts are made. The circled region emphasizes the area where the ITO was partially removed. ....	63
Figure 31: Schematic representation of the OPV devices forming planar heterojunctions between thin films of P3AT derivatives (spin-coating or Langmuir-Schaefer deposition providing ~100 nm thick) and BuPTCD (PVD deposition providing ~50 nm thick). ....	64
Figure 32: $\pi$ -A isotherms for regioregular P3AT: P3BT, P3HT, P3OT and P3DT. In the inset, pictures of P3OT Langmuir film showing the condensed phase and the collapse of the film. ....	65
Figure 33: BAM images of Langmuir films for regioregular P3AT at deposition pressures: SP = 30 mN/m for P3BT and SP = 20 mN/m for P3HT, P3OT and P3DT.....	66
Figure 34: Absorption spectra in the UV-visible range for P3AT thin films deposited by (a) spin-coating and (b) LS onto an ITO substrate. (c) UV-visible spectra performed during the growth of seven layers for P3OT LS film. ....	67
Figure 35: Optical absorption spectra with polarized light for the LS devices of P3AT. ....	69

Figure 36: Photoluminescence spectra for regioregular P3AT films deposited by (a) spin-coating and (b) LS technique.....	70
Figure 37: $\pi$ -stacks of the regioregular P3AT, where R represents an alkyl group. Adapted from <sup>133</sup> .....	71
Figure 38: AFM topographic images of the films of P3BT, P3HT, P3OT and P3DT deposited by (a) spin-coating and (b) LS techniques onto ITO substrate. The roughness values $R_q$ are contained inside of each image.....	71
Figure 39: $I$ vs. $V$ electrical measurements of the regioregular P3AT comparing LS and spin-coating techniques. ....	73
Figure 40: $I$ vs. $t$ plots in dark and illuminated conditions of P3BT, P3HT, P3OT and P3DT LS films on IDE.....	75
Figure 41: $I$ vs. $F$ plots for the ITO/P3AT/Al devices, where P3BT, P3HT, P3OT and P3DT were deposited by (a) spin-coating and (b) LS techniques. Image from <sup>157</sup> .....	77
Figure 42: Energy diagram for a hypothetical ITO/polymer/Al device.....	78
Figure 43: CV data for the P3AT films deposited by (a) spin-coating and (b) LS technique. (c) CV results for the P3OT spin-coated film showing the oxidation potentials onset ( $E'_{ox}$ ) estimated from the intersection of the two tangents drawn at the rising oxidation current and background current in the cyclic voltammograms. Image from <sup>157</sup> .....	78
Figure 44: UV-visible absorption spectra for the P3DT spin-coated film where the red lines intersection show the wavelength used to calculate the $E_{gap}$ for the thin film.....	80
Figure 45: Images from the color changing of P3BT spin-coated film during the CV measurements around (a) 0.4 V, (b) 0.6 V and (c) 0.8 V for the oxidation process and (d) 0.6 V and (e) 0.4 V for the reduction one. Image from <sup>157</sup> .....	81
Figure 46: Absorption spectra in the UV-visible range for the LS films of P3BT, P3HT, P3OT and P3DT obtained in different voltages during the oxidation and reduction (inset) processes. In the graphs, the black, red, green, dark blue, blue, pink and orange lines are related with the electric potential 0, 0.2, 0.4, 0.6, 0.8, 1.0 and 1.2 V, respectively. Image from <sup>157</sup> .....	83
Figure 47: $Z'$ vs. $f$ plots for the ITO/P3AT/Al devices for (a) spin-coated and (b) LS films...	84
Figure 48: $-Z''$ vs. $f$ plots for the ITO/P3AT/Al devices for (a) spin-coated and (b) LS films.	86
Figure 49: Argand diagrams for the ITO/P3AT(spin-coating)/Al devices.....	87
Figure 50: Argand diagrams for the ITO/P3AT(Langmuir-Schaefer)/Al devices. ....	88
Figure 51: Equivalent electrical circuits used in the theoretical fitting for the ITO/P3AT/Al devices. ....	89



Figure 52: $\pi$ -A isotherms for (a) PCPDTBT and (b) PDTSBT of neat and SA:polymer mixtures of 2:1, 4:1 and 8:1 (mmol).....	92
Figure 53: $I$ vs. $V$ electrical measurements for the LB mixed films of the low-bandgap polymers (a) PCPDTBT and (b) PDTSBT. ....	94
Figure 54: $J$ vs. $V$ curves for the planar heterojunction devices (ITO/P3AT/C <sub>60</sub> /Al) under illumination of a halogen lamp (150 mW/cm <sup>2</sup> ). In the devices, the donor layers were deposited by (a) spin-coating and (b) Langmuir-Schaefer techniques. ....	96
Figure 55: $J$ vs. $V$ curves for the planar heterojunction devices (ITO/PEDOT:PSS/P3AT/BuPTCD/Al) under illumination of a solar simulator (100 mW/cm <sup>2</sup> - AM 1.5). In the devices, the donor layers were deposited by (a) spin-coating and (b) Langmuir-Schaefer techniques. ....	98
Figure 56: $J$ vs. $V$ curves measured under illumination of a solar simulator for the OPV devices using P3DT spin-coated film as donor layer with (light blue curve) and without (dark blue curve) LiF used as cathode window layer. $J$ vs. $V$ result for the OPV device simply using P3DT LS film (orange curve) as donor layer. ....	100

## LIST OF TABLES

Table 1: Electrical properties of P3AT films deposited by spin-coating and LS techniques...	74
Table 2: Results obtained by CV and UV-visible optical absorption measurements for the P3AT films deposited by spin-coating and LS technique. ....	80
Table 3: Parameters obtained through the theoretical fittings of components $Z'$ and $Z''$ by Equation 9 for the ITO/P3AT(spin-coating)/Al and ITO/P3AT(LS)/Al devices.....	89
Table 4: Electrical conductivity values for thins films of P3AT derivatives deposited by spin-coating and LS. ....	91
Table 5: Deposition parameters for the LB films of PCPDTBT and PDTSBT. ....	93
Table 6: Electrical properties for the LB films of low-bandgap polymers in IDE devices. ....	94
Table 7: Photovoltaic parameters obtained for the OPV devices of P3AT (spin-coating or Langmuir-Schaefer) and BuPTCD in planar heterojunctions. ....	98

## LIST OF SYMBOLS

$A$	effective electrode area	$\text{cm}^2$
$C$	capacitance	F
$d$	thickness	nm
$\mathcal{D}$	dispersity	dimensionless
$E'_{\text{ox}}$	oxidation potential onset	eV
$E_{\text{gap}}$	gap energy	eV
$E_{\text{HOMO}}$	HOMO energy	eV
$E_{\text{LUMO}}$	LUMO energy	eV
$f$	frequency	Hz
$F$	electric field	V/m
$FF$	fill factor	dimensionless
$h$	height of the IDE digit	nm
$I$	electric current	A
$I_0$	intensity of incident light	$\text{W}/\text{cm}^2$
$J$	density of current	$\text{A}/\text{cm}^2$
$J_{\text{max}}$	density of current that maximize $FF$	$\text{A}/\text{cm}^2$
$J_{\text{SC}}$	density of current at short circuit	$\text{A}/\text{cm}^2$
$k_{\text{cell}}$	cell constant	$\text{m}^{-1}$
$L$	length of the IDE digit	mm
$M_{\text{n}}$	number-average molar masses	g/mol
$M_{\text{w}}$	weight-average molar masses	g/mol
$N$	number of digits of the IDE	dimensionless
$R$	electrical resistance	$\Omega$
$R_{\text{q}}$	RMS roughness	nm
$SP$	surface pressure	mN/m
$V$	electric tension	V
$V_{\text{max}}$	voltage that maximize $FF$	V
$V_{\text{OC}}$	open-circuit voltage	V
$w$	width of the IDE digit	$\mu\text{m}$
$Z^*$	electrical impedance	$\Omega$
$\eta$	efficiency of the photovoltaic device	dimensionless
$\lambda_{\text{ex}}$	excitation wavelength	nm
$\lambda_{\text{max}}$	wavelength of maximum absorption	nm
$\rho$	electrical resistivity	$\Omega\text{m}$
$\sigma^*$	AC electrical conductivity	S/cm
$\sigma_{\text{DC}}$	DC electrical conductivity	S/cm
$\tau$	dielectric relaxation time	s
$\tau_0$	time constant	s
$\omega$	angular frequency	rad/s

The symbols indicated by \* are complex quantities.

## SUMMARY

Presentation .....	22
CHAPTER 1: Introduction .....	24
1.1. Electronic transport in semiconducting organic materials .....	26
1.2. Organic photovoltaic devices .....	27
1.3. Electrical characterization of photovoltaic devices .....	29
CHAPTER 2: Organic Materials .....	31
2.1. Electron acceptors .....	31
2.2. Electron donors .....	32
2.3. Organic synthesis .....	33
2.3.1. Monomer synthesis .....	34
2.3.2. Polymer synthesis .....	39
CHAPTER 3: Fabrication of films and characterization .....	43
3.1. Fabrication of thin solid films .....	43
3.1.1. Spin-coating .....	43
3.1.2. Langmuir and Langmuir-Blodgett .....	43
3.1.3. Langmuir-Schaefer .....	46
3.1.4. Physical vapor deposition .....	47
3.2. Brewster angle microscopy .....	48
3.3. UV-visible absorption spectroscopy .....	48
3.4. Photoluminescence spectroscopy .....	49
3.5. Atomic force microscopy .....	49
3.6. Perfilometry analysis .....	50
3.7. Cyclic voltammetry .....	50
3.8. Impedance spectroscopy .....	51
3.8.1. The Solartron impedance analyzer .....	53
3.8.2. Analysis of impedance data using equivalent circuits .....	54
3.9. Electrical measurements in direct current .....	56
3.9.1. The Keithley source-measure unit .....	56
3.9.2. Analysis of the $I$ vs. $V$ curves .....	57
3.10. Electrical measurements in organic thin films .....	58
3.10.1. Parallel contact: interdigitated electrodes .....	59
3.10.2. Perpendicular contact: diode-like structure .....	62

3.10.3. Photovoltaic devices in planar heterojunction .....	63
CHAPTER 4: Thin films of alkyl-substituted polythiophene derivatives.....	65
4.1. P3AT Langmuir films .....	65
4.2. Spin-coated and Langmuir-Schaefer films of P3AT .....	67
4.2.1. UV-visible absorption .....	67
4.2.2. Photoluminescence spectroscopy .....	70
4.2.3. AFM morphology.....	71
CHAPTER 5: Electrical properties of thin films.....	73
5.1. Electrical measurements in IDE devices.....	73
5.2. Electrical measurements in ITO/P3AT/Al devices.....	76
5.3. Electrochemical measurements and energy diagrams .....	77
5.4. Impedance analysis in ITO/P3AT/Al devices.....	83
CHAPTER 6: Low-bandgap polymers.....	92
6.1. Langmuir and Langmuir-Blodgett films of low-bandgap polymers.....	92
6.2. Electrical characterization of low-bandgap polymers.....	94
CHAPTER 7: Electrical measurements in organic heterojunction devices .....	96
7.1. Preliminary results in the homemade dark box.....	96
7.2. P3AT derivatives and perylene in planar heterojunctions .....	97
CHAPTER 8: Conclusions .....	101
COMPLEMENTARY INFORMATION .....	103
REFERENCES .....	105
APPENDIX.....	118

## Presentation

This thesis is about the results obtained from March 2011 and June 2015. The research was conducted most of the time at *Departamento de Física, Química e Biologia* (DFQB) of *Faculdade de Ciências e Tecnologia* (FCT) in UNESP (Presidente Prudente - SP, Brazil) under supervision of Prof. Dr. Clarissa de Almeida Olivati and co-supervision of Prof. Dr. Carlos José Leopoldo Constantino. From June 2011 this PhD research was supported by the Brazilian funding agency FAPESP (2010/20094-1). A research period abroad was funded by the Brazilian agency CAPES (BEX 18580/12-2) for one year at *Equipe Physique et Chimie des Polymères* (EPCP) of *Institut des Sciences Analytiques et de Physico-chimie pour l'Environnement et les Matériaux* (IPREM) in UPPA (Pau, France), under supervision of Dr. Christine Dagron-Lartigau. Considering the contribution of the period abroad in this PhD research, the agreement for the international joint supervision of thesis (with double degree) between the Brazilian and French universities was approved. The thesis is divided into eight chapters that are briefly described below.

Chapter 1 is about the motivations and goals of this PhD research. Besides, some important concepts for the organic electronic area and photovoltaic devices are also defined. In Chapter 2 are presented the organic materials studied in this thesis. These materials are considered as electron acceptors (perylene and fullerene) or donors (polythiophene derivatives) in organic photovoltaic devices. Also in this chapter, the synthesis route for a low-bandgap polymer is shown.

Chapter 3 is basically about the fabrication of thin films of the organic materials presented in Chapter 2 and their characterization. Distinct deposition techniques for the films were studied, such as spin-coating, Langmuir-Blodgett, Langmuir-Schaefer and physical vapor deposition. Several techniques were applied in order to characterize these films in relation to optical, morphological and electrical properties. The techniques and the equipment used for the optical and morphological characterization were briefly described in this chapter. A bit further discussion was conducted for the electrical characterization, once these kinds of measurements are the specialty of the *Laboratório de Optoeletrônica e Filmes Finos* (LOFF) at UNESP. The fabrication of the devices used for the electrical characterization, as well as the organic photovoltaic devices were also described in this chapter.

The results for the film fabrication of the polythiophene derivatives are shown in Chapter 4, as well as their optical (UV-visible absorption and photoluminescence spectroscopies) and morphological (atomic force microscopy) characterization. The results

obtained for the electrical characterization of the polythiophene films are shown in Chapter 5. DC electrical measurements were performed in order to find the electrical conductivity of the polythiophene films, electrochemical measurements were performed to estimate the energy diagrams and impedance spectroscopy were also performed in order to separate the contributions of interfaces and bulk in a diode-like device. Each electrical characterization requires different devices, as stated in Chapter 3.

Chapter 6 shows the results obtained for the low-bandgap polymers in the Langmuir trough. The polymers were deposited by Langmuir-Blodgett technique onto interdigitated electrodes to perform electrical characterization. The results presented here are the preliminary results obtained from the partnership between Prof. Olivati and Dr. Dagron-Lartigau. Further characterizations of the low-bandgap polymers will be carried out for other students in the LOFF group.

In Chapter 7 the results obtained for the organic heterojunction devices are shown. Few preliminary results obtained with a halogen lamp also are shown, despite the heterojunction devices do not present photovoltaic effect. Later, the results obtained with a solar simulator are shown and discussed. Finally, in Chapter 8 the main conclusions are presented. The differences in optical, morphological and electrical properties of polythiophene derivatives due to different deposition techniques were disclosed. These distinct properties of polythiophene films influenced the results obtained in the photovoltaic devices, which is the most important conclusion of this research.

## CHAPTER 1: Introduction

As the technologic development evolves, the exploitation of environmentally harmful energy sources increases proportionally. In recent years, new technologies that avail renewable energy have been introduced. Solar energy is one of the most important and successful sources of renewable energy <sup>1</sup>. Photovoltaic or solar cells are promising tools for converting solar energy into electricity, but some of its parameters still need to be improved <sup>2</sup>.

In recent years, it has been noticed a great progress in the field of organic photovoltaics (OPV) and results from devices with more than 10 % efficiency have been achieved by the main companies in the area: Toshiba (11.0 %) and Mitsubishi Chemical (11.1 %) <sup>3</sup>. Nevertheless, in order to become competitive for commercial applications, the OPV devices should perform 15 % efficiency <sup>4</sup>. Apart from efficiency, another hurdle to overcome in OPV area is the lifetime of the devices due to the degradation of organic compounds <sup>4,5</sup>.

Recent researches worldwide have shown alternatives to improve the performance of OPV devices, such as use of a cathode window layer <sup>6</sup> and an anode buffer layer <sup>7</sup>; use of [6,6]-phenyl C<sub>61</sub> butyric acid methyl ester (PCBM) on blends with polymers <sup>8</sup>; better understanding of the structure <sup>9</sup> and electronic transport mechanisms <sup>10</sup> on devices with bulk heterojunction (BHJ); use of C<sub>70</sub> fullerene derivative for greater chemical stability of the device <sup>11</sup>; synthesis of low bandgap polymers and application of multilayer devices (tandem cells) <sup>12</sup>; improved organization of the organic layer at molecular level via thermal treatments <sup>13</sup> and use of donor multilayer in energy cascades <sup>14</sup>. Alternatives to reduce the cost of devices through deposition of films and electrodes without the use of masks <sup>15</sup> and use of gridlines of silver nanoparticles and transparent polymer grid electrode as the anode <sup>16</sup> have also been in the focus of development.

Conducting polymers, mainly polythiophene derivatives, in different structured devices are widely studied nowadays as electron donor layers in OPV area <sup>17,18</sup>. The transport properties of conducting polymers are dominated by the disorder due to the partial crystallinity, non-homogeneous doping or by the disorder that is created during the synthesis and material processing <sup>19</sup>. In a polymer, the conjugation along the backbone leads to the formation of molecular orbitals, which are equivalent to the electronic bands in an inorganic semiconductor, where the HOMO (highest occupied molecular orbital) and the LUMO (lowest unoccupied molecular orbital) are the analogous to the valence and conduction bands, respectively. The energy difference between HOMO and LUMO levels, several times defined



as the separation between  $\pi$  and  $\pi^*$  orbitals, is a forbidden energy scale (band gap)  $E_{\text{gap}}$ <sup>20</sup>, which determines the intrinsic electronic properties of the material<sup>21</sup>.

The electrical conductivity of organic materials is heavily reliant on its nanomorphology<sup>22</sup>, which in the case of thin films, can be varied by employing different deposition techniques<sup>23</sup>. Thin films of organic materials can be fabricated by distinct experimental methods<sup>24,25</sup>, including Langmuir techniques<sup>26,27</sup>, which are particularly suitable if some degree of molecular control is required<sup>28,29</sup>. However, regioregular polythiophene derivatives often form poorly stable multilayer of stacked polymer (aggregate clusters) instead of true monolayers in the Langmuir trough<sup>30,31</sup>. The high degree of film rigidity usually associated with this type of Langmuir film makes it extremely difficult to transfer the neat polymers into multilayer structures by Langmuir-Blodgett technique (vertical dipping method)<sup>32</sup>. In this case, the Langmuir film can be transferred to a solid substrate by the Langmuir-Schaefer technique (horizontal lifting method)<sup>33,34</sup>.

Thin films of neat polythiophene derivatives prepared by Langmuir techniques have been widely characterized by optical, structural and morphological measurements<sup>34,35</sup>. Due to deposition issues mentioned above, it is difficult to obtain large area uniformity to coat electrodes, hence the lack of electrical characterization data. A comparative study considering the effect of different deposition techniques on the electrical properties of polythiophene derivatives is not found. This is an important parameter to be investigated since distinct supramolecular arrangements in thin films can be induced by the deposition method applied, affecting the charge mobility and very likely the photovoltaic performance.

Although polythiophene derivatives are widely studied in the OPV area<sup>36-39</sup>, other materials are emerging as alternatives to overcome the barriers in the organic photovoltaic area<sup>40</sup>. Some of the prerequisites to achieve higher efficiencies is to design donor and acceptor materials with optimized energy levels (HOMO and LUMO), provide efficient charge transport in the donor-acceptor blend, efficient charge generation and limited recombination losses<sup>41</sup>. Many low-bandgap conjugated copolymers with structures containing alternating sub-units with electron donating and accepting properties have proven themselves particularly efficient for these purposes<sup>42,43</sup>.

The present study deals with the influence of the deposition technique of the electron donor layer in an OPV device. The nanostructured thin films of four regioregular alkyl-substituted polythiophene derivatives (P3AT) deposited by the Langmuir-Schaefer technique are compared herein to the widely used spin-coated ones. The electrical conductivity characterization of these films was complemented by optical (UV-visible and fluorescence),

morphological (atomic force and Brewster angle microscopies) and electrochemical (cyclic voltammetry) measurements. Additionally, a low-bandgap polymer widely used in OPV devices was synthesized. The behavior of this polymer in the Langmuir trough and the formation of Langmuir-Blodgett films were investigated.

### 1.1. Electronic transport in semiconducting organic materials

It is known that many of the concepts concerning electronic transport phenomena that are well established for traditional inorganic materials also apply to the organics, such as metal-semiconductor interface effects in disordered media, hopping and tunneling conduction. Nevertheless, the organic materials usually also exhibit special features such as low dimensionality of polymer chains, which can lead to a highly anisotropic conduction<sup>44</sup>. In a polymer, although a small region can be crystalline, its global behavior is typically comparable to the one of an amorphous system<sup>45</sup>. Despite of this fact, the alignment in these crystalline sites can tune the maximum achievable value of conductivity<sup>44</sup>, which is also another distinct feature of the electronic transport in this class of materials.

After the Discovery by Heeger, MacDiarmid, Shirakawa and collaborators that the conductivity of polyacetylene could be increased to more than seven orders of magnitude upon doping with iodine or arsenic pentafluoride (AsF<sub>5</sub>)<sup>46</sup> there has been a great interest in this class of materials, along with the Nobel Prize of Chemistry in the year 2000. Some examples of the most remarkable conducting polymers are the polyacetylene, polyaniline, polypyrrole, polythiophene and polyphenylene vinylene, which behave as semiconductors in their neutral form, but can reach metallic conduction values after doping<sup>47</sup>. All of these compounds present alternating double and single bonds along the polymer chain as a common feature, which are called conjugated double bonds<sup>48</sup>. As a contrast to the high strength of single bonds between individual atoms and molecules, the double bonds are usually weak, since the  $\pi$  electrons are loosely bound to the neighboring carbon atoms. Consequently, one of these electrons can be easily dissociated from its carbon atom by a small amount of energy coming e.g. from a thermal source<sup>20</sup>, and then accelerated by an external electric field.

The transport properties of conducting polymers are dominated by the disorder due to the partial crystallinity, non-homogeneous doping or by the disorder that is created during the synthesis and material processing<sup>19</sup>. These charges self-localize to form non-linear configurations: solitons, polarons, bipolarons<sup>49</sup> which are concepts that were developed during the mid-80's<sup>21,50</sup> initially to explain the increase of conductivity of the conjugated

polymers up to the metallic regime upon doping. Semiconducting polymers are more susceptible to suffer structural distortions than their inorganic counterparts. In this manner, the electronic excitations tightly relate to distortions of the chain<sup>50</sup>, and hence the charge carrier in a polymer is different from a free electron in a metal or the electron/hole in an inorganic semiconductor<sup>48</sup>.

Usually, solitons are invoked as charge carriers to help understand the electronic transport in a degenerate conjugated polymer, whereas polarons and bipolarons represent charge carriers in a non-degenerate conjugated polymer<sup>48</sup>. Polythiophene is a specific example of a non-degenerated conjugated polymer at ground state, in which polarons and especially bipolarons (confined soliton pairs) are important excitations and the dominating charge storage configurations<sup>49</sup>. Due to the ease of intra-chain transfer, it is believed that the charge transfer happens mainly along the conjugated chains<sup>49</sup>, thus making it necessary to stress that the terms soliton, polaron and bipolaron are only employed to interpret the movement of electrons along a segment of the polymer chain<sup>48</sup>, being the inter-chain hopping a secondary step<sup>49</sup>.

## 1.2. Organic photovoltaic devices

Photovoltaic devices are a good example of a traditional applications area where organic and inorganic materials work together to sum their characteristics up in a same device<sup>51</sup>. The structure of an OPV device is similar to those of the organic light emitting diodes (OLEDs). The active organic layer stands between a metallic cathode and a transparent conducting anode, the latter being usually Indium-Tin oxide (ITO), deposited onto a glass substrate. The light illuminates the active layer through the ITO, and the photocurrent or electric tension is measured between the ITO and the cathode, which is usually made from metals like aluminum, magnesium or calcium<sup>52</sup>.

When the device is illuminated, most of the photons absorbed by the organic material will lead to the formation of excitons. In inorganic semiconductors, the excitons consist of an electron-hole pair, coupled by coulombian interaction<sup>53</sup> whereas in organic semiconductors, the exciton is formed by two paired polarons of opposite sign<sup>48</sup>. They migrate in organic materials through diffusion along a conjugated chain, through hopping between different segments of a chain, and even between chains, possibly due to defect sites originated from a dense packing or even inter-chain interactions<sup>54,55</sup>. Since they are formed by a positive and a negative polaron, excitons are neutral in charge, meaning that they have to be dissociated in

order to promote charge generation within the device. To make this dissociation happen, the exciton must find a potential barrier along its way, which can be promoted by the interface between the organic material and the electrode, or even by the presence of impurities in the active layer.

Like an OLED, the photovoltaic devices formed by a single layer (homojunction) of polymer or conjugated organic molecules is not usually very efficient<sup>56</sup>. One of the causes is that the electric field generated by two different electrodes is rarely high enough to completely dissociate the electrostatic bonds of about 100 to 500 meV between the polarons of the photogenerated excitons<sup>20</sup>. In addition, since the device is made up by a single layer, even the excitons dissociated by the application of an external electric field will recombine before reaching the electrodes. This ease of recombination happens because both positive and negative polarons are dissociated and transported in a same active layer.

A bi-layer OPV device fabricated between materials with different work functions<sup>57</sup> is called planar heterojunction, and increases the efficiency of a solar cell<sup>20</sup>. In a planar heterojunction, the donor-acceptor organic interface dissociates the exciton more efficiently than in organic-metallic interfaces of a homojunction device<sup>56</sup> and the dissociated charges are transported through their related layer (positive polaron by the donor layer, and negative polaron by the acceptor layer), conducted by internal electric field all the way to the electrode<sup>58</sup>.

A third, and more recent kind of device is based on the BHJ, which is formed by an interpenetrating network (blend) of donor and acceptor materials, thus producing a large interfacial area and favoring the dissociation of excitons<sup>59</sup>. In contrast to the plain heterojunction devices, the charge carriers in a BHJ are generated through the entire volume of the device<sup>58</sup>. Figure 1 shows a sketch of both devices.

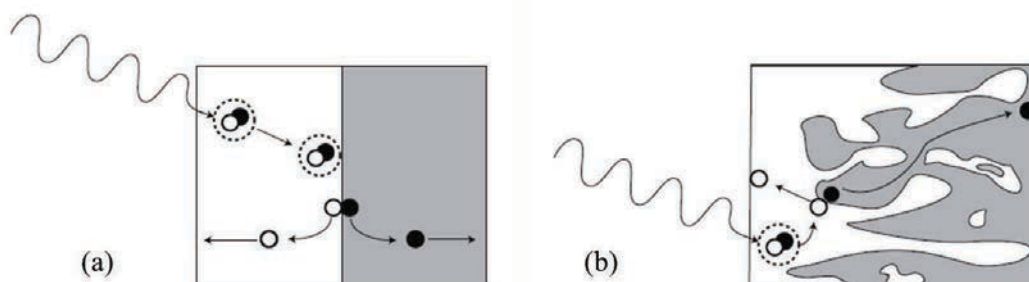


**Figure 1:** Schematic diagram of the heterojunction types in an OPV device: (a) planar heterojunction and (b) BHJ. Adapted from<sup>59</sup>.

### 1.3. Electrical characterization of photovoltaic devices

The electrical response of each photovoltaic device is obtained through characteristic curves of density of current *vs.* applied electric tension (*J vs. V*). Figure 2 shows a hypothetical characteristic curve for a device in the dark and under illumination. This represents the ideal behavior of a photovoltaic cell<sup>60</sup>. The curve in the dark represents the response of a rectifying diode, which presents electric current only when forward biased, i.e. when the electrode of higher work function is connected to the positive terminal of the power supply and the electrode of smaller work function is connected to the negative terminal. The open-circuit voltage,  $V_{OC}$ , and the density of current at short circuit,  $J_{SC}$ , are represented in the curve under illumination<sup>61</sup>.

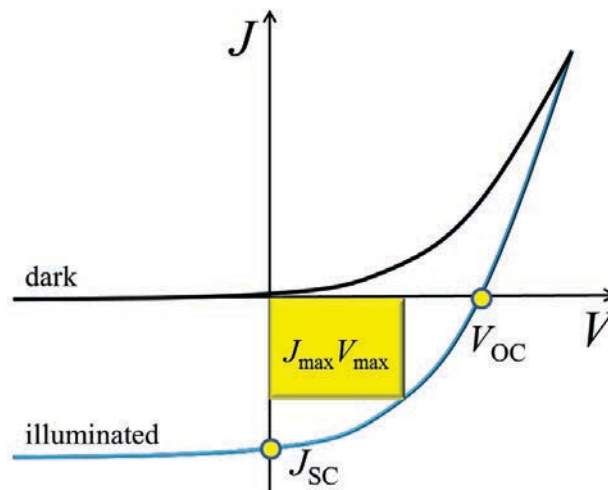


**Figure 2:** Characteristic *J vs. V* curve for a photovoltaic device.

The amount of electrical energy that can be obtained from a photovoltaic cell is given by the ratio between the maximum power delivered by the device (represented by the area of the rectangle in Figure 2) and the power relative to the values of  $J_{SC}$  and  $V_{OC}$ . This ratio is a measure of how far the *J vs. V* curve of a photovoltaic device differs from the ideal situation<sup>62</sup> and is called fill factor (*FF*), which can be calculated using the expression:

$$FF = \frac{J_{\max} V_{\max}}{J_{SC} V_{OC}} \quad (1)$$

where  $J_{\max}$  and  $V_{\max}$  are the values of the density of current and voltage that maximize the product <sup>56</sup>, leading to the rectangle of larger area in the fourth quadrant of the  $J$  vs.  $V$  curve. The conversion efficiency of a photovoltaic device,  $\eta$ , relates the maximum power generated by the cell to the power of the incident light, according to:

$$\eta = FF \frac{J_{sc} V_{oc}}{I_0} \quad (2)$$

where  $I_0$  is the intensity of incident light on the device in  $\text{W}/\text{cm}^2$ .

Other relevant parameters to the characterization of solar cells are the spectral response and quantum efficiency <sup>60</sup>. The former is defined by the ratio between the output current at the cell and the wavelength and intensity of the incident light beam, whereas the latter is determined by the number of electron-hole pairs that are collected for each incident photon.

## CHAPTER 2: Organic Materials

The results presented in this thesis were chosen to be from the materials which presented the most interesting results of electrical measurements during the earlier years of the PhD research. Both acceptor and donor organic materials were chosen for the study, aiming to broaden the possibilities of combinations in the fabrication of photovoltaic devices.

### 2.1. Electron acceptors

Organic macromolecule of perylene tetracarboxylic derivative, PTCD, was chosen to be employed as the acceptor electron layer in the organic heterojunction. The bisbutylimido perylene (BuPTCD) was provided by Dr. J. Duff from the Xerox Resource Centre of Canada. The molecular structure for the BuPTCD is shown in Figure 3.

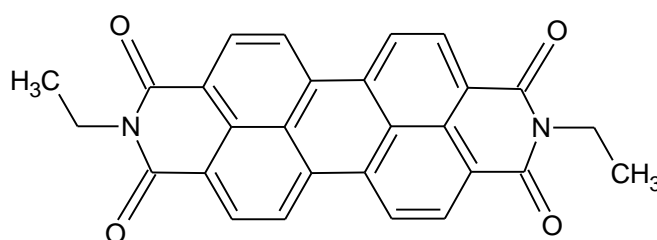


**Figure 3:** Molecular structure for the BuPTCD.

An important compound used in the field of photovoltaic devices is the fullerene- $C_{60}$ <sup>63,64</sup> and also its derivatives<sup>65,66</sup>, thus summing up possibilities of combination in the choice of heterostructures. The fullerene- $C_{60}$  shown in Figure 4 was obtained commercially by Sigma-Aldrich<sup>67</sup> and used as acceptor electron layer.

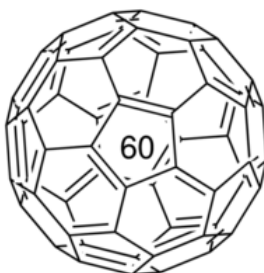


**Figure 4:** Structural formula for fullerene- $C_{60}$ . Image from<sup>67</sup>.

## 2.2. Electron donors

Several polymers of alkyl-substituted polythiophene derivatives (P3AT) were used to probe the viability of deposition in the form of thin films, and later their electrical characteristics. The regioregular derivatives poly(3-butylthiophene), poly(3-hexylthiophene), poly(3-octylthiophene) e poly(3-decylthiophene), abbreviated herein as P3BT, P3HT, P3OT and P3DT, were obtained commercially from Sigma-Aldrich. These derivatives present molar masses for the repeating units in crescent number of carbons in the side chain of 138, 166, 194 and 222 g/mol, respectively. In Figure 5, sketches of the structural formulae of the monomers are shown for these compounds, together with their acronyms to ease the reference to each one along the text.

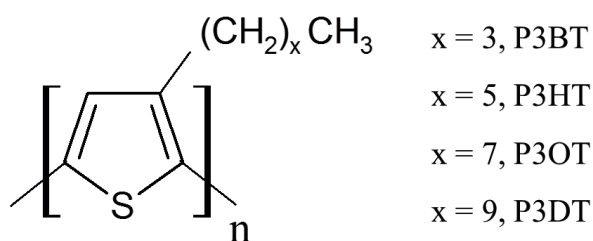


**Figure 5:** Condensed structural formula for the regioregular alkyl-substituted polythiophene derivatives.

Although the derivative P3HT is widely studied in the OPV area <sup>36-38</sup>, recently other polymeric materials were given focus for the application in devices, such as the low-bandgap polymers <sup>8,68</sup>. From March 2013 to February 2014, the student started an internship in the research group entitled “*Equipe Physique et Chimie des Polymères*” (EPCP) which is part of the IPREM (*Institut des Sciences Analytiques et de Physico-chimie pour l'Environnement et les Matériaux*) at *Université de Pau et des Pays de l'Adour* (UPPA) in the city of Pau, France. It counted with the partnership of the researchers involved in the CAPES/COFECUB project, entitled “*Fabricação e caracterização de células solares baseadas em polímeros orgânicos nanoestruturados*”, coordinated in Brazil by Prof. Dr. Carlos Frederico Graeff. While overseas, the student was advised by Dr. Christine Dagron-Lartigau during the development of the project entitled “*Síntese e fabricação de filmes finos de polímeros semicondutores com baixo valor de bandgap para aplicação em dispositivos fotovoltaicos*”.

The polymer chosen to be synthesized during the internship abroad was the poly[(4,4-bis(2-ethylhexyl)-cyclopenta-[2,1-b:3,4-b']dithiophene)-2,6-diyl-alt-(2,1,3-benzothiadiazole)-4,7-diyl], PCPDTBT, shown in Figure 6(a). The PCPDTBT is a low-bandgap polymer usually



employed in photovoltaic devices, leading to conversion efficiencies over 3 % in blends with PCBM<sup>69</sup>. In order to obtain this polymer, two monomers are required: 4,4-bis(2-ethylhexyl)-2,6-bis(trimethylstannyl)-4H-cyclopenta[2,1-b:3,4-b']dithiophene which is a derivative of CPDT with branched chains, and the 4,7-dibromo-2,1,3-benzothiadiazole, BT. The synthesis of CPDT is made in 7 steps that were the main focus of the internship, while the BT monomer was previously synthesized by a research fellow, Junping Du, at EPCP (IPREM, UPPA - Pau - France). The synthesis of the CPDT monomer and the PCPDTBT polymer will be described in the section 2.3.

Besides the PCPDTBT, another low-bandgap polymer was studied. The poly[(4,4'-dioctyldithieno[3,2-b:2',3'-d]silole-2,6-diyl)-*alt*-(2,1,3-benzothiadiazole)-4,7-diyl)], PDTSBT, was synthesized by Hussein Awada during his PhD at EPCP (IPREM, UPPA - Pau - France). The molecular structure of PDTSBT is shown in Figure 6(b) and its synthesis was previously reported<sup>70</sup>.

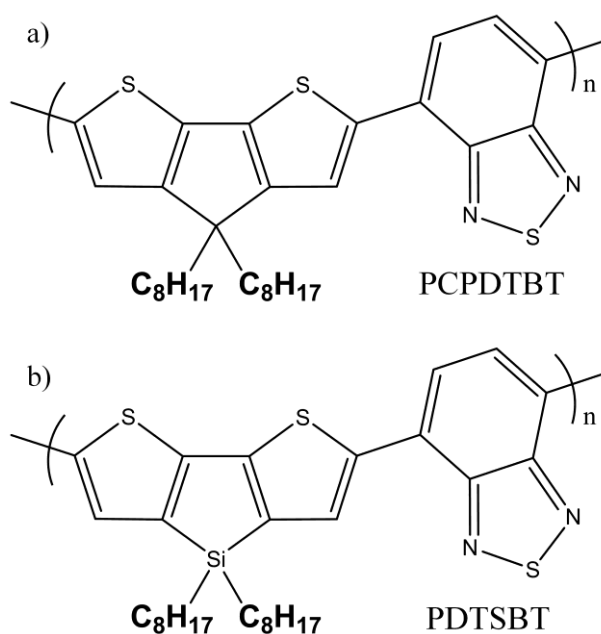


**Figure 6:** Molecular structure of the low-bandgap polymers (a) PCPDTBT and (b) PDTSBT.

### 2.3. Organic synthesis

This section will present the steps for synthesizing the monomer derived from CPDT with branched chains and the polymer PCPDTBT. Each step of the synthesis shown in this section had to be repeated for several times until achieving success, or even the amount and yield needed to proceed to the next step of the synthesis route.

### 2.3.1. Monomer synthesis

To synthesize the 4*H* cyclopenta[2,1-*b*:3,4-*b'*]dithiophene, CPDT, shown in Figure 7, plus its derivatives, several synthesis routes based on scientific papers<sup>42,71-73</sup> were probed, tested and adapted to obtain the best possible results using the available tools in our laboratory (IPREM, UPPA - Pau - France). The synthesis of CPDT takes five steps. After obtaining this same compound, two more steps are required in order to end up with the desired chain, before polymerizing the monomers. The synthesis route to obtain the CPDT and its branched chains derivative is shown in Figure 8.

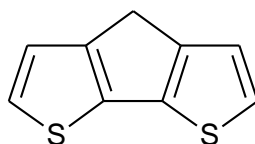


**Figure 7:** Molecular structure of 4*H*-cyclopenta[2,1-*b*:3,4-*b'*]dithiophene (CPDT).

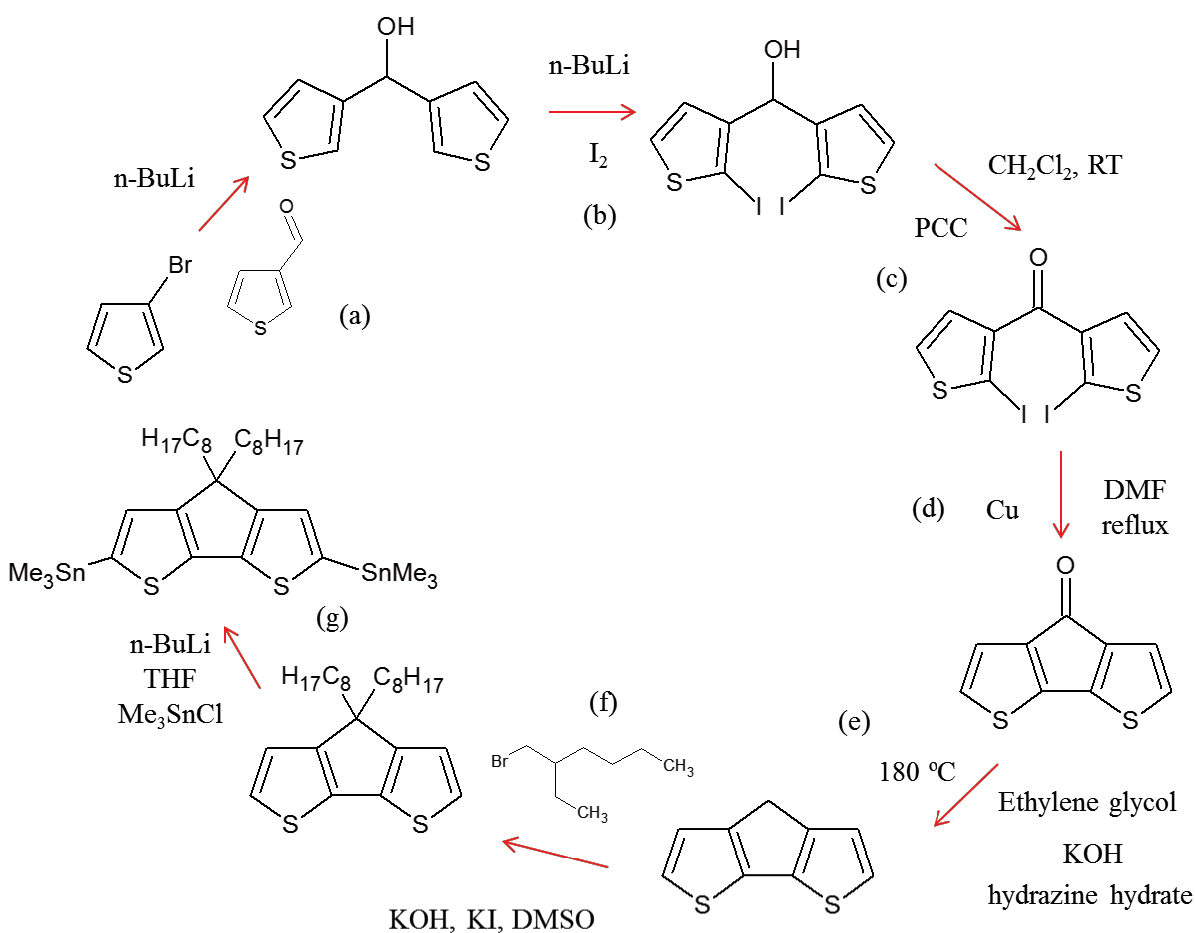


**Figure 8:** Synthesis route of 4,4-bis(2-ethylhexyl)-2,6-bis(trimethylstannyl)-4*H*-cyclopenta[2,1-*b*:3,4-*b'*]dithiophene, CPDT branched chains derivative.

The nuclear magnetic resonance spectroscopy, NMR, is a technique that allows the determination of molecular structure from the magnetic properties of the atomic nuclei and the surrounding electrons. For this reason it is the most important tool employed during the organic synthesis to evaluate the monomer structures (Figure 9(a)) and move on with the synthesis route. Common components for the NMR instrumentations are (i) a magnet to supply the static magnetic field  $B_0$ , (ii) devices to generate a second magnetic field at radio frequencies and receive the resulting NMR signal, (iii) a probe for positioning the sample in the magnet, (iv) hardware for stabilizing the  $B_0$  field and optimizing the signal and (v) computers for controlling much of the operation and for processing the NMR signals<sup>74</sup>. The NMR spectra were recorded using a Bruker® Advance 400 MHz spectrometer (Figure 9(b)) in  $\text{CDCl}_3$  and ambient conditions under supervision of the technician Abdel Khoukh. Chemical shifts of the  $^1\text{H}$  NMR were reported in ppm relative to TMS (tetramethyl silane) at 0 ppm. To perform the analysis, a small quantity of the product should be well dissolved and then transferred into an NMR tube (Figure 9(c)).



**Figure 9:** (a) The NMR analysis allows for the deducing of the molecular structure of the compounds obtained at each of the steps of the monomer synthesis route, (b) part of the Bruker UltraShield 400 Magnet NMR instrument and (c) some NMR tubes with different products inside dissolved in  $\text{CDCl}_3$ .

(a) and (b) *Bis(2-iodo-3-thienyl)methanol*

n-Butyllithium solution (BuLi) in hexane (16 ml, 2.5 M, 40 mmol) was added dropwise to a stirred solution of 3-bromothiophene (6.52 g, 40 mmol) in dry ether (50 ml) at  $-78\text{ }^\circ\text{C}$ . Stirring was continued at  $-78\text{ }^\circ\text{C}$  for 3 hours (Figure 10(a)) and subsequently a solution of thiophene-3-carboxaldehyde (4.48 g, 40 mmol) in dry ether (50 ml) was added dropwise (Figure 10(b)). The reaction mixture was stirred at  $-78\text{ }^\circ\text{C}$  for 1 h, allowed to reach room temperature, and stirred overnight. After cooling to  $-78\text{ }^\circ\text{C}$ , BuLi solution in hexanes (32 ml, 2.5 M, 80 mmol) was added dropwise. Stirring at  $-78\text{ }^\circ\text{C}$  was continued for 2 hours, and then

the resulting mixture was allowed to reach room temperature and stirred for 1h. After cooling to  $-78\text{ }^{\circ}\text{C}$ , a solution of iodine (32 g, 126 mmol) in ether (200 ml) was added dropwise. The reaction mixture was allowed to warm-up to room temperature and stirred overnight. A 10% w/w aqueous solution of  $\text{Na}_2\text{SO}_3$  (10 g in 100 ml) was added with vigorous stirring and the mixture was acidified with a 10% w/w aqueous solution of hydriodic acid (HI) to pH  $\sim 5$ . The mixture was washed with mili-Q water and diethyl ether. The organic layer was extracted and dried over anhydrous  $\text{MgSO}_4$ . The solvent was distilled-off under reduced pressure to obtain a dark brown mixture of oil and solid (14.7 g, yield 82%).  $^1\text{H}$  NMR ( $\text{CDCl}_3$ , 400 MHz)  $\delta$  (ppm): 7.45 (d, 2H), 6.95 (d, 2H), 5.80 (s, 1H), 2.25 (s, 1H). The bis(2-iodo-3-thienyl)methanol was used without further purification.



**Figure 10:** (a) experimental apparatus for chemical reaction using liquid nitrogen and (b) time of dropwise addition of thiophene-3-carboxaldehyde.

(c) *Bis(2-iodo-3-thienyl)ketone*

A mixture of bis(2-iodo-3-thienyl)methanol (4.48 g, 10 mmol) in  $\text{CH}_2\text{Cl}_2$  (100 ml) was stirred for one hour. To this solution, solid pyridinium chlorochromate (3.23 g, 15 mmol) was added in one portion at room temperature. Stirring was continued at room temperature for 15 hours under  $\text{N}_2$ . The solvent was distilled-off under reduced pressure and the crude product was purified by flash chromatography using  $\text{CH}_2\text{Cl}_2$  as eluent. The solvent was distilled-off under reduced pressure (Figure 11(a)) and the solid obtained was recrystallized with methanol. The product was obtained as a yellow solid (Figure 11(b)) (2.8 g, yield 62%).  $^1\text{H}$  NMR ( $\text{CDCl}_3$ , 400 MHz)  $\delta$  (ppm): 7.50 (d, 2H), 7.11 (d, 2H).

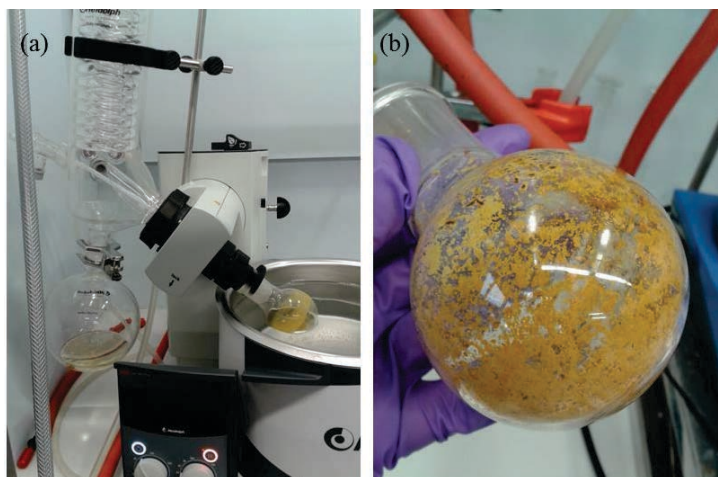


**Figure 11:** (a) removal of the solvent using the rotary evaporator system and (b) solid product obtained after recrystallization procedure.

(d) *4H-cyclopenta-[2,1-b:3,4-b']dithiophen-4-one*

To a stirred solution of bis(2-iodo-3-thienyl)ketone (4.2 g, 9.4 mmol) in DMF (30 ml), Cu powder (1.8 g, 28.3 mmol) was added in one portion at room temperature. The reaction mixture was heated under reflux (155 °C) for 15 hours under N<sub>2</sub> (Figure 12(a)). After cooling to room temperature, the solid was filtered off (Figure 12(b)) and washed with diethyl ether. The solution was washed with H<sub>2</sub>O and diethyl ether. The organic layer was extracted and dried over anhydrous MgSO<sub>4</sub>. The solvent was distilled-off under reduced pressure and the resulting product was purified by flash chromatography using a mixture of petroleum ether and ethyl acetate. The product was obtained as a purple solid (1.5 g, yield 83%). <sup>1</sup>H NMR (CDCl<sub>3</sub>, 400 MHz)  $\delta$  (ppm): 7.07 (d, 2H), 7.01 (d, 2H).



**Figure 12:** (a) experimental apparatus for the chemical reaction using the reflux system and (b) filtering the remaining Cu after the reaction.

(e) *4H-cyclopenta[2,1-b:3,4-b']dithiophene*

4H-cyclopenta-[2,1-b:3,4-b']dithiophen-4-one (1 g, 5.2 mmol) was suspended in 20 ml of ethylene glycol. Potassium hydroxide (1 g) and hydrazine hydrate (2 ml) were added under N<sub>2</sub>. The mixture was heated to 180 °C (Figure 13(a)) and stirred for 24 hours. The resulting brown solution was allowed to cool down to room temperature and washed with water, brine, saturated ammonium chloride solution and CH<sub>2</sub>Cl<sub>2</sub>. The organic phase was extracted with and dried over anhydrous MgSO<sub>4</sub>. The solvent was distilled-off under reduced pressure. The resulting was left under vacuum (Figure 13(b)) for 72 hours and the desired product was obtained as brown oil (570 mg, yield 62%). <sup>1</sup>H NMR (CDCl<sub>3</sub>, 400 MHz) δ (ppm): 7.20 (d, 2H), 7.12 (d, 2H), 3.56 (s, 1H).



**Figure 13:** (a) experimental apparatus for the chemical reaction at 180 °C and (b) resulting product left under vacuum after removal of the solvent by the rotary evaporator system.

(f) *4,4-bis(2-ethylhexyl)-4H-cyclopenta[2,1-b:3,4-b']dithiophene*

To a suspension solution of 4H-cyclopenta[2,1-b:3,4-b']dithiophene (570 mg, 3.2 mmol) in DMSO (30 mL), potassium hydroxide (650 mg, 12 mmol) and potassium iodide (10 mg) were added, followed by 2-ethylhexyl bromide (1.44 g, 7.5 mmol). The mixture was stirred for 15 h at room temperature and under N<sub>2</sub> atmosphere. The resulting was washed with water, brine and hexane. The organic layer was extracted, dried over MgSO<sub>4</sub> and the solvent was removed under reduced pressure. The crude resulting was purified by flash chromatography using hexane as eluent and three different products were obtained. From the NMR results, the first fraction is related to the desired product, a light-yellow oil (1.2 g, yield 93%). <sup>1</sup>H NMR (CDCl<sub>3</sub>, 400 MHz) δ (ppm): 7.11 (d, 2H), 6.95 (d, 2H), 1.9 (d, 4H), 0.6-1.1 (m, 30H).



(g) *4,4-bis(2-ethylhexyl)-2,6-bis(trimethylstannyl)-4H-cyclopenta[2,1-b:3,4-b']dithiophene*

n-Butyllithium solution (BuLi) in hexane (1.9 ml, 2.5 M, 4.8 mmol) was added dropwise to a stirred solution of 4,4-bis(2-ethylhexyl)-4H-cyclopenta[2,1-b:3,4-b']dithiophene (500 mg, 1.2 mmol) in dry THF (15 ml) at -78 °C. The reaction mixture was stirred at -78 °C for 1 h, allowed to reach room temperature, and stirred for 2 hours. After cooling to -78 °C, trimethyltin chloride, Me<sub>3</sub>SnCl, (8.4 ml, 1M, 8.4 mmol) was added dropwise. The reaction mixture was allowed to warm-up to room temperature and stirred overnight (725 mg, yield 97% according to <sup>1</sup>H NMR). <sup>1</sup>H NMR (CDCl<sub>3</sub>, 400 MHz) δ (ppm): 6.96 (s, 2H), 1.85 (d, 4H), 0.6-1.1 (m, 30H).

### 2.3.2. Polymer synthesis

A solution of an equimolar amount of the CPDT derivative (293.5 mg, 0.403 mmol) and BT (118.47 mg, 0.403 mmol) was prepared in chlorobenzene (3 mL) under N<sub>2</sub>. To the stirred solution, tris(dibenzylideneacetone)dipalladium(0) (7.4 mg, 8 x 10<sup>-3</sup> mmol) and tri(o-tolyl)phosphine (12.27 mg, 4 x 10<sup>-3</sup> mmol) were added. The resulting solution was heated at 150 °C for 15 hours. Figure 14(a) and (b) show, respectively, the reaction system before heating (red mixture) and after 15 hours of reaction (dark green solution). After cooling to room temperature, the resulting blue viscous liquid was dissolved in hot chlorobenzene then added slowly into a vigorously stirred cold methanol (Figure 14(c)).

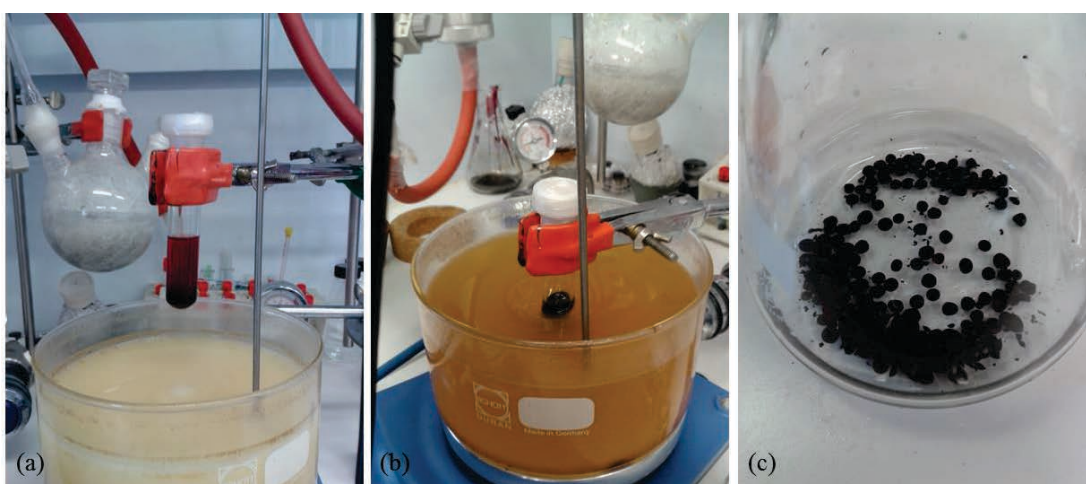


**Figure 14:** Polymerization reaction (a) before and (b) after heating and (c) the resulting polymer, PCPDTBT, precipitated in methanol.

The purification by Soxhlet extraction (Figure 15(a)) was carried out using methanol, acetone, hexane and chloroform until the extracts were colorless. In the first two fractions we got clear solutions meaning that the monomers reacted totally. For the hexane fraction we got 8 mg of low molar mass polymer. The chloroform soluble fraction was concentrated (Figure 15(b)) and precipitated in methanol. The polymer was collected after filtering (Figure 15(c)) and dried to yield a dark blue solid (200 mg,  $M_n = 18000$  g/mol,  $\mathcal{D} = 1.57$ , yield 92%). Another polymerization was performed under similar conditions to obtain 300 mg of  $\text{CHCl}_3$  soluble fraction ( $M_n = 17000$  g/mol,  $\mathcal{D} = 1.14$ ). The results for number-average molar masses ( $M_n$ ), weight-average molar masses ( $M_w$ ) and dispersity ( $\mathcal{D} = M_w/M_n$ )<sup>75</sup> mentioned above were obtained through a chromatographic method.

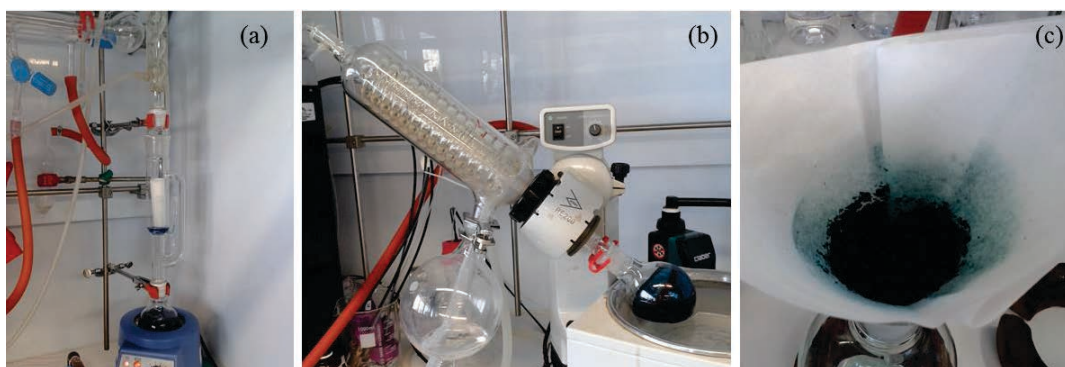


**Figure 15:** (a) experimental apparatus for the Soxhlet extraction, (b) reduction in volume of the chloroform soluble fraction using the rotary evaporator system and (c) filtering the clean polymer PCPDTBT after precipitation in methanol.

Gel permeation chromatography (GPC) is a chromatographic method in which macromolecules in solution are separated by their hydrodynamic volume (related to the size of the macromolecules). The chromatographic column is filled with a porous media. When a solution of molecules of different sizes flow into the column, the smaller ones get trapped in the pores, but the larger ones do not. Consequently, larger molecules elute from the column, separated from the smaller ones. This is the separation principle of GPC method<sup>76</sup>.

Historically the porous medium was made of a gel and therefore gel permeation chromatography (GPC) was coined, a term still prevalent in the industry today. Low pressure analysis of biological compounds is often referred to as gel filtration chromatography (GFC)<sup>77</sup>. The  $M_n$ ,  $M_w$  and  $D$  values were estimated against polystyrene standards by GPC using a bank of 4 columns (Shodex KF801, 802.5, 804 and 806) each 300 mm x 8 mm at 30 °C with THF eluent at a flow rate of 1.0 mL/min controlled by a Malvern pump (Viskotek, VE1122)



and connected to Malvern VE3580 refractive index (RI) and Malvern VE3210 UV-visible detectors.

The polymer thermal and chemical stability are important parameters supposing application in organic electronic area. Thermogravimetric analysis (TGA) is a technique in which the mass of a substance is monitored as a function of temperature or time as the sample specimen is subjected to a controlled temperature program in a controlled atmosphere<sup>78</sup>. The TGA measurement was performed on a TGA-Q50 from TA Instruments at a heating rate of 10 °C/min under nitrogen atmosphere. The polymer chemical stability is an important parameter supposing applications in organic electronic area. The TGA result (Figure 16) shows a mass loss about 6% until 150 °C, possibly due to a solvent evaporation (chlorobenzene), and a good stability until 350 °C. Furthermore, the thermogram shows thermal decomposition from 380 to 580 °C with weight loss about 40%.

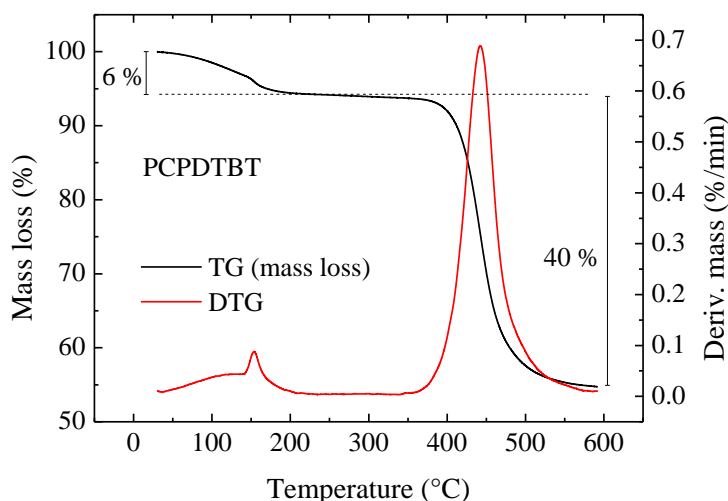


**Figure 16:** TGA thermogram of PCPDTBT.

Differential scanning calorimetry (DSC) is a thermal analysis technique probes the temperature variation of the material's heat capacity ( $C_p$ ). A sample of known mass is heated or cooled and the changes in its  $C_p$  are tracked as changes in the heat flow. This allows the detection of transitions like melts, glass transitions, phase changes and curing<sup>79</sup>. The DSC measurement was carried out with DSC-Q100 from TA Instruments operating under a nitrogen atmosphere with heating and cooling rate of 10 °C/min. Until 140 °C the DSC curve of PCPDTBT (data not shown) does not show any important thermal phenomena. The absence of melting and crystallization peaks may have two possible explanations<sup>70</sup>: i) low crystallinity of the polymer due to insufficient flatness preventing the proper stacking of the

polymer chains to form crystalline areas or ii) the hardness of the backbone and strong interchain interactions may induce melting points above the temperature in which the measurements were performed (140 °C).

## **CHAPTER 3: Fabrication of films and characterization**

### **3.1. Fabrication of thin solid films**

Four distinct techniques were employed for the deposition of thin films of the organic materials involved in this study: spin-coating, Langmuir-Blodgett (LB), Langmuir-Schaefer (LS) and physical vapor deposition (PVD). The LS and PVD techniques were not initially included in the project, but LS proved itself to be very efficient for the deposition of rigid Langmuir films, while PVD for the deposition of organic macromolecules<sup>80,81</sup>. For this reason, these techniques were included in this work, and further details will be discussed throughout the text. P3AT films were obtained through the spin-coating and LS techniques, for comparison.

#### **3.1.1. Spin-coating**

The spin-coating technique is used to uniformly apply thin films onto plain substrates. The procedure is to drip an excessive amount of the desired solution onto the substrate, which is then spun to high speeds, in order to spread the fluid by centrifugal force<sup>82</sup>. The equipment is called spinner, in which the substrate is attached by suction before initiating the procedure. The solvent to be employed is generally volatile and evaporates during the spinning process, leading to the formation of the film of the desired material.

For the production of thin films by the spin-coating technique, a spinner with rotation speed of 1000 rpm for 60 seconds interval was used. P3AT derivatives were dissolved in chloroform providing solutions of 15 mg/ml with the aid of an ultrasonic device for 30 minutes. As an exception, only for P3BT the concentration of the solution had to be lowered to 10 mg/ml, due to the difficulty to solubilize large quantities of this material in chloroform.

#### **3.1.2. Langmuir and Langmuir-Blodgett**

The Langmuir films are obtained by spreading a small amount of a material consisting of amphipathic (amphiphilic) molecules onto a liquid surface. This material, such as a fatty acid, a polymer or alike<sup>83</sup>, is first dissolved in a volatile solvent that evaporates after the solution is spread onto the water. The stearic acid is a standard octadecanoic fatty acid (18 carbon atoms) used as a model in the formation of Langmuir thin films, since it has a

hydrophilic head and hydrophobic tail, as shown in the detail of Figure 17. A solution of stearic acid in chloroform of concentration of 1 mg/mL was prepared, and 50  $\mu\text{L}$  were spread in an ultra pure water subphase (milli-Q). The Langmuir film was then studied using the so-called  $\pi$ -A isotherms (Figure 17), which refer to the mean molecular area occupied by molecules present at the interface for different values of surface pressure, SP. This  $\pi$ -A isotherm is an analogy to a curve of pressure *vs.* volume for a common thermodynamic system<sup>84</sup>.

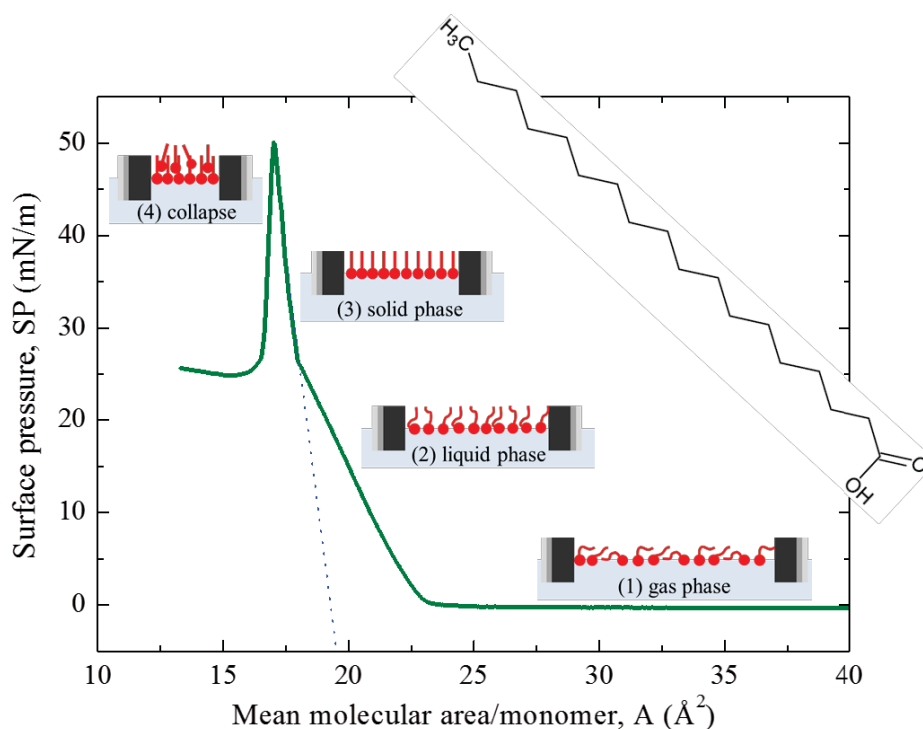


**Figure 17:**  $\pi$ -A isotherm obtained for stearic acid and its chemical structural formula shown in details.

In analogy to thermodynamics, three distinct phases characterize the compression of the Langmuir film: (1) gas phase, in which the molecules do not interact with each other; (2) liquid phase in which the molecules have some interaction, and (3) the solid phase where the molecules are relatively well oriented and packaged, forming a film of monomolecular thickness (Langmuir film). In the solid phase, it can be possible to find the area per molecule of the analyzed material, in this case, stearic acid. The  $\pi$ -A isotherm was obtained at 22°C and the value found for the area per molecule in our case was  $\sim 19 \text{ \AA}^2$  as shown in Figure 17, which is in good agreement with the literature<sup>84,85</sup>. This area is computed as a tangent line to the condensed phase. At this stage, the Langmuir film can then be transferred to a solid substrate which is immersed vertically through the layer (Figure 18), forming the so-called

Langmuir-Blodgett film (LB), whose main features are the very small thickness and high degree of structural ordering <sup>86</sup>. If the Langmuir film is compressed beyond the condensed phase, the molecules can group inordinately on top of each other causing the collapse of the film, as is the case for typically amphiphilic molecules. The collapse of stearic acid Langmuir film can also be seen in Figure 17, step 4.

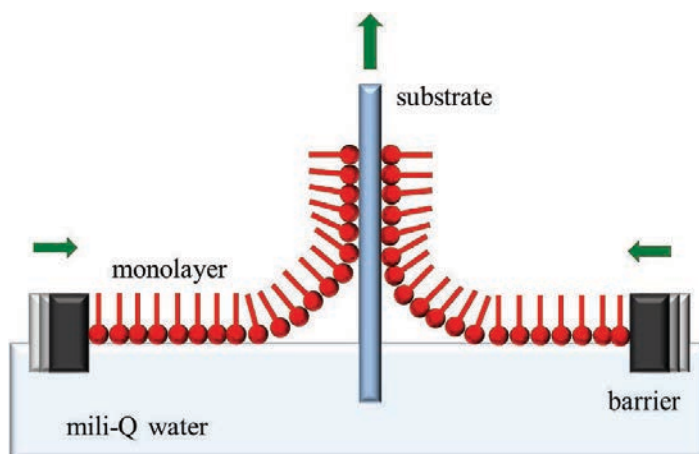


**Figure 18:** Langmuir-Blodgett deposition scheme for amphiphilic molecules.

For the study of Langmuir films, a Langmuir trough model KSV 5000 was employed. Before starting any experiment, the trough is cleaned with chloroform. The liquid subphase used for the depositions was pure milli-Q water. The organic material solution is spread on the milli-Q water sub-phase with the aid of a micro syringe (Hamilton), previously cleaned with chloroform. The spreading of the solution is done slowly to avoid any precipitation of the solution in the sub-phase, improve the spreading of the material and avoid abrupt variations in the surface pressure in the subphase/material interface. The experiments were conducted at room temperature (22 °C) using a barrier speed compression of 10 mm/min.

In order to obtain isotherms of the P3AT Langmuir films, solutions of 0,2 mg/ml concentration were used <sup>87</sup>. For each material, different amounts of solution were spread onto the trough as a test, and the volumes that gave better results were 1000, 1000, 1500 and 1250  $\mu\text{L}$  for the P3BT, P3HT, P3OT and P3DT derivatives, respectively. It was not possible to deposit films of the pure regioregular polythiophene derivatives via LB, and hence the LS technique was invoked, which will be described in the next section.

The low-bandgap polymers PCPDTBT and PDTSBT were also characterized in the Langmuir trough using a 0.2 mg/mL solution of the polymers in chloroform. The molecular

weights for the repeating units are 534.85 and 550.93 g/mol for the PCPDTBT and PDTSBT, respectively. For neat PCPDTBT and PDTSBT it was not possible to grow multilayer LB films. As the materials studied here are not ideal molecules, polymer mixtures with stearic acid (SA) in different percentages were used in order to improve the LB deposition. SA:PCPDTBT and SA:PDTSBT rates of 2:1, 4:1 and 8:1 (mmol) were prepared in chloroform solution, in order to evaluate the influence of the SA in the LB films quality.

### 3.1.3. Langmuir-Schaefer

A LS film is made of one or more layers of the Langmuir film, and the deposition is made by horizontal contact of the substrate with the monolayer<sup>88</sup>. In order to assure a better deposition, the substrate is slowly brought to the interface while the Langmuir film remains stabilized. Then, the substrate is raised slowly, and the hydrophobic end of the molecule stays in touch with the substrate (Figure 19). The surface pressure of choice used for the LS deposition of each material was the same of the ones used for the attempts to deposit via LB, since the initial experimental procedure is the same for both techniques. The P3BT derivative was deposited in  $SP = 30$  mN/m, while the derivatives P3HT, P3OT and P3DT were deposited in  $SP = 20$  mN/m.

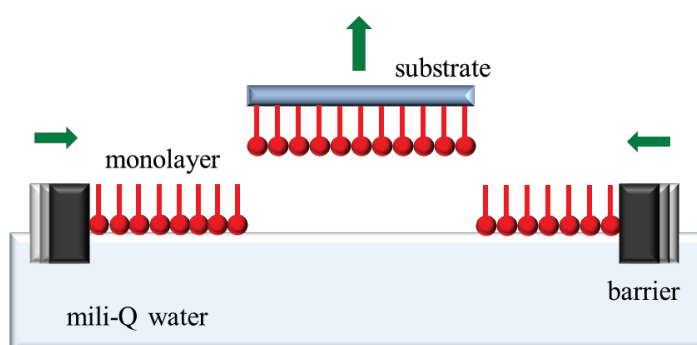


**Figure 19:** Langmuir-Schaefer deposition scheme for amphiphilic molecules.

P. G. Nicholson *et al.* have successfully deposited P3HT in glass substrates using the LS technique<sup>89</sup>, and to ease the deposition, they have previously treated the substrate's surface (microscope slide) to make it hydrophobic by submerging it into piranha solution and then in a solution of hexamethyldisilazane (HMDS) in acetone it was then rinsed with toluene and dried at 110 °C in a furnace for 20 minutes. In this work, the films were deposited onto an ITO electrode, which is naturally hydrophobic and does not require any previous treatment

<sup>90,91</sup>. Figure 20 shows the Langmuir trough during the solid phase of the P3HT film, after depositing the first LS layer.

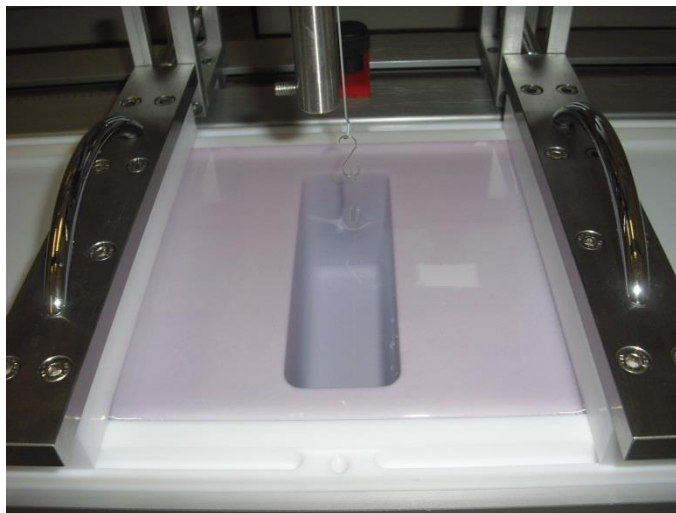


**Figure 20:** Langmuir film of P3HT derivative in the solid phase at 20 mN/m, indicating a region of lack of material due to previous deposition of LS film.

### 3.1.4. Physical vapor deposition

There are three PVD processes: evaporation, ion plating and sputtering <sup>92</sup>, and the former was used in this work. Evaporation is a common method for the deposition of thin films. The material to be evaporated is placed in a metallic crucible with a high melting point, through which an electric current is applied to raise the temperature and promote the evaporation of the material. The process takes place at a high vacuum chamber, which enhances the mean free path of the evaporated particles and allow them to move directly to the target (substrate), where they condense and return to the solid state.

The films of BuPTCD and C<sub>60</sub> were grown using this technique, using a Boc Edwards model Auto 306 Evaporation System at 10<sup>-6</sup> Torr chamber pressure. In the evaporator, the material in its powder form was placed on a tantalum crucible and the electric current was raised slowly up to ~ 1.4 A, leading to an evaporation rate of 0,2 to 0,5 nm/s, which was monitored by a quartz crystal microbalance.

### 3.2. Brewster angle microscopy

The Brewster angle microscopy (BAM) technique allows for the observation of monolayers typically in an air-water interface using a Langmuir trough, where an image of the surface is created by the detection of changes in the refractive index of the surface of the water due to the presence of surfactant molecules<sup>93</sup>. With BAM images, it is possible to obtain the size of domains, shape, packing, homogeneity and morphology of the Langmuir films. BAM images were obtained for the Langmuir films of regioregular P3BT, P3HT, P3OT and P3DT derivatives, using the MicroBAM KSV accessory, connected to a KSV 2000 Langmuir trough, which is installed on *Laboratório de Filmes Finos* (UNESP - Presidente Prudente/SP - Brazil), under the supervision of Prof. Dr. Carlos J. L. Constantino.

### 3.3. UV-visible absorption spectroscopy

The electronic transitions that occur in the visible and ultraviolet (UV) regions of the spectrum are due to absorption of radiation by specific types of bonds and functional groups within the molecules. The absorption wavelength,  $\lambda$ , is related to the amount of energy required for the transition, while the intensity is dependent on the probability of the transition to occur when the electronic system and radiation interact<sup>94</sup>.

The electrons in a molecule can be classified in four different types: i) inner layer electrons that are not involved in binding. These have very high excitation energy and do not contribute to the absorption in the UV or visible regions. ii) covalent bonding electrons ( $\sigma$  electrons). These also have very high excitation energies to contribute to the UV or visible absorption. iii) non-bonding paired electrons (n electron), such as N, O, S and halogens. These are less strongly bound to the  $\sigma$  electrons and can be excited by UV or visible radiation. iv) electrons in  $\pi$  orbitals, double or triple bonds. These can be more easily excited and are responsible for most of the electronic spectra in the UV-visible region<sup>94</sup>. The absorption spectroscopy is therefore a useful technique for identifying functional groups in a molecule and enables the qualitative determination of compounds containing absorbing groups<sup>95</sup>.

A molecule has normally unoccupied orbitals called anti-binding orbitals, corresponding to the energy level of the excited state ( $\sigma^*$  orbital or  $\pi^*$ ). Therefore, the radiation absorption results in an electronic transition to an anti-binding orbital. The most common are one from  $\pi$  or n orbitals to  $\pi^*$  orbital, and these are represented by  $\pi \rightarrow \pi^*$  and  $n \rightarrow \pi^*$ <sup>94</sup>. Both transitions require the presence of an unsaturated functional group to provide



the  $\pi$  orbitals. Molecules containing such functional groups and which are capable of absorbing UV-visible radiation are called chromophores<sup>95</sup>.

For the characterization of thin films by UV-visible absorption spectroscopy, a Varian Cary 50 spectrophotometer was employed, which is installed on *Laboratório de Filmes Finos* (UNESP - Presidente Prudente/SP - Brazil), under the supervision of Prof. Dr. Carlos J. L. Constantino. During the cyclic voltammetry measurements, absorption spectra were obtained using a Thermo Scientific model Genesys 6 spectrophotometer, under the supervision of Prof. Dr. Marystela Ferreira (UFSCar - Sorocaba/SP - Brazil).

### 3.4. Photoluminescence spectroscopy

Fluorescence and phosphorescence are examples of luminescence, which is the light emission from any excited state of a molecule. The luminescence measurements are inherently more sensitive than absorption measurements, and have lower energy (higher  $\lambda$ ) than the absorbed radiation (excitation). One can even compare the absorption and emission spectra, because they have a rough relationship of a mirror image if the spaces between the vibrational levels of the molecule and the transition probabilities are similar<sup>96</sup>.

The luminescence measurements were performed on a Shimadzu RF-5301PC fluorescence spectrophotometer in the *Grupo de Polímeros* of the *Instituto de Física de São Carlos* (USP - São Carlos/SP - Brazil), under the supervision of Dr. Debora T. Balogh. An emission spectrum is obtained by keeping the excitation wavelength ( $\lambda_{\text{ex}}$ ) fixed and sweeping the region of the emitted radiation. The wavelength of maximum absorption ( $\lambda_{\text{max}}$ ) in the UV-visible spectra was used for excitation, to obtain the emission spectra.

### 3.5. Atomic force microscopy

The atomic force microscopy (AFM) was developed by Gerd Binnig, Calvin Quate and Christoph Gerber during the 80's<sup>97</sup> and uses non-optical elements to obtain an image, but only the interaction force between a small tip and the surface of the sample<sup>98</sup>. The AFM technique provides topography data of surfaces, and for the characterization of organic thin films it's especially useful to help evaluate the formation of defects and agglomerates, to measure the thickness and roughness of the films.

The nanoscale morphology of the films deposited onto ITO was characterized by means of a Nanosurf model Easy Scan 2 AFM, with Silicon tip coupled to its cantilever and

running on contact mode. Post-processing of the topographical images was carried out with the Gwyddion 2.31 software, and the roughnesses of the films were obtained. In Figure 21, the AFM image for the ITO covered glass substrate is shown, and the RMS roughness,  $R_q$ , was in the order of 10 nm.

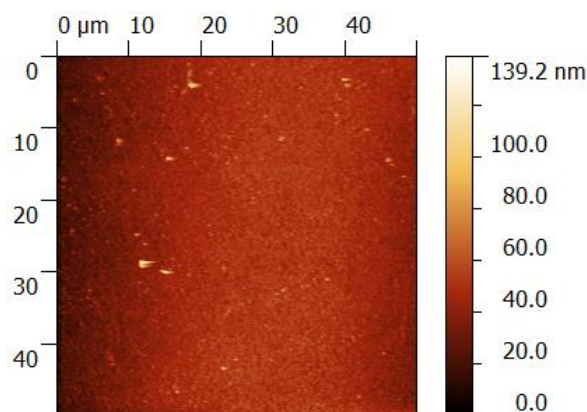


**Figure 21:** AFM image of the ITO substrate, where films were deposited for morphological analysis.

### 3.6. Perfilometry analysis

The perfilometry technique consists in sweeping a Diamond tip along the surface of a sample, with controlled parameters such as speed and force. The perfilometer then measures the relative height of the surface during the sweep of the tip, and binds this information with the position coordinates of the tip. The data is digitalized and captured by suitable software<sup>99</sup>, making it possible to further analyze curvature, roughness, thickness, stresses, intrinsic defects or even defects caused by treatments<sup>100</sup>.

The thicknesses of the pristine films, as well as the organic heterojunctions, were determined by a Veeco model Dektak 150 perfilometer, in the *Grupo de Polímeros* of the *Instituto de Física de São Carlos* (USP - São Carlos/SP - Brazil), under the supervision of Dr. Debora T. Balogh. To help determine the thickness of the films, they were previously scratched with an aluminum tip, creating a trench which bottom reaches the surface of the substrate.

### 3.7. Cyclic voltammetry

The voltammetry comprehends a group of electro analytical methods in which information about the sample are obtained by the measurement of the electric current as a

function of the applied voltage, under proper conditions that promote the polarization of a reference electrode, or a work electrode<sup>95,101</sup>. In the cyclic voltammetry (CV), the response of electric current of a small stationary electrode that is immersed in a solution under rest is obtained as a function of a triangle-shaped excitation voltage signal. A linear voltage sweep between two defined values is initially applied. It first goes to the maximum and then returns to the initial value at the same rate. This process is then repeated indefinitely while the current is registered. The two defined edge potentials are called reversion potentials<sup>95</sup>.

The CV measurements were carried out using a potentiostat/galvanostat, model PGSTAT 30, under the responsibility of Prof. Dr. Marystela Ferreira (UFSCar - Sorocaba/SP - Brazil). The supporting electrolyte was a solution of 0.1 mol.L<sup>-1</sup> tetrabutylammonium-perchlorate (TBAP) in acetonitrile (ACN). The cell was composed of an Ag/ACN with TBAP, 0.1 mol.L<sup>-1</sup> as reference electrode, a 1.0 cm<sup>2</sup> platinum counter electrode and the working electrode (spin-coating and LS films of P3AT deposited onto ITO). The experimental setup is shown in Figure 22.



**Figure 22:** Electrochemical cell and experimental setup for CV measurements.

### 3.8. Impedance spectroscopy

In the direct current circuits, the electrical resistance of a component is simply defined as the ratio between the voltage and current on it. However, in many circuits the electrical current is not stationary, and varies with time. These are called alternating current

(AC) circuits, and the ratio between voltage and current is called electrical impedance, defined as  $Z^* = V^*/I^*$ . In the same way as a combination of resistors in series or parallel may be represented by a single equivalent resistor, an arbitrary combination of resistors, capacitors and inductors may be represented by a single equivalent impedance  $Z^*$ , which is a complex number, and its modulus admits the same unit used for the DC electrical resistance, the Ohm ( $\Omega$ ).

The impedance,  $Z^* = Z' - jZ''$ , is a vectorial complex quantity that can be represented in a plane, in rectangular or polar coordinates, as shown in Figure 23. This defines the Argand-Gauss diagram, or complex plane <sup>102</sup>, in which the real ( $Z'$ ) and imaginary ( $Z''$ ) parts of  $Z^*$  are plotted in the X and Y-axis, respectively. In the polar form, the impedance related to the phase angle  $\theta$  following the expression  $Z^* = |Z^*| e^{j\theta}$  which can be converted to the rectangular form by using the Euler's formula:  $e^{j\theta} = \cos(\theta) + j\sin(\theta)$ . It's important to remark that this parametric representation allows for a point analysis of the impedance, which can then be studied as a time-invariant function <sup>102</sup>.

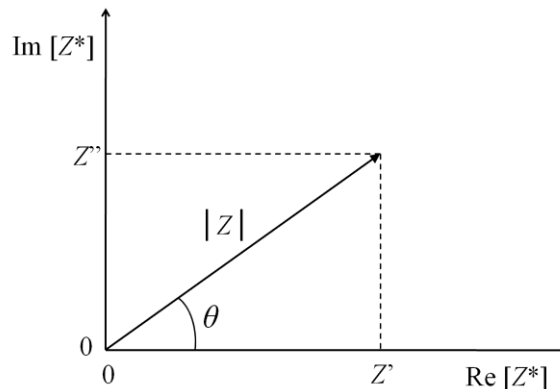


**Figure 23:** Impedance  $Z^*$  plotted as a planar vector using rectangular and polar coordinates.

The conventional impedance spectroscopy consists of measuring  $Z^*$  over a broad range of frequencies. From the resulting plot of  $Z^*$  vs.  $f$ , it is possible to obtain information about the electrical properties of the electrode-material system <sup>102</sup>. The analysis of the charge transport process that can be present in the experimental cell (assembly of sample, electrodes and connectors) may often be represented as an equivalent circuit of ideal resistors, capacitors and inductors, and can help explain the behavior of the experimental cell <sup>102</sup>. The impedance analyzer often provides a pair of physical quantities calculated from the values of voltage and current measured on the experimental cell, and especially the phase difference ( $\theta$ ) between

them. The quantities used in this work were  $Z'$  e  $Z''$ , which represent the electrical resistance and reactance of the sample as a function of the frequency.

Similarly to the DC case, it is possible to calculate the AC electrical conductivity,  $\sigma^*$ , of the sample, following the relation

$$\sigma^* = \frac{1}{Z^*} k_{cell} \quad (3)$$

and separating the real and imaginary parts in accordance with

$$\sigma^* = \frac{Z'}{Z'^2 + Z''^2} k_{cell} - j \frac{Z''}{Z'^2 + Z''^2} k_{cell} \quad (4)$$

where  $k_{cell}$  relates the geometrical parameters of the device, as it will be described in 3.12.1.

From the  $\sigma'$  vs.  $f$  plots at low frequencies, one can notice that the conductivity gets close to a constant value, and for non-Ohmic devices it is distinct for each applied DC bias. Extrapolating this plot to  $f \rightarrow 0$ , one obtains  $\sigma'(0)$ , which should be considered equivalent to the DC electrical conductivity,  $\sigma_{DC}$ . Another way to calculate  $\sigma_{DC}$  is by using the estimate value of the sample  $R$  from the impedance plots ( $Z''$  vs.  $Z'$ ) where  $Z''$  is null at low frequencies, and again calculating using the Equation 6.

### 3.8.1. The Solartron impedance analyzer

In order to be able to study the DC conductivity in ceramic and polymeric devices without introducing significant distortions and non-linear effects, it is necessary to keep the excitations at a low level. Working at this low-excitation regime requires an electrometer capable of measuring very small currents, as the resistivity,  $\rho$ , of these materials is usually high, as compared to metallic materials. In this case, the measurements would be susceptible to considerable broadband-coupled noise, inherent of this technique, and could negatively affect the results. A workaround to this problem is to use the lock-in technique, where a sinusoidal electric signal of well-known frequency and amplitude is applied to the sample, and the response signal can be separated from noise by means of harmonic analyses and common-mode rejection<sup>103</sup>.

However, some of the charge carriers commonly found in organic devices can suffer diffusion when subjected to low-frequency electrical excitations and move to neighboring chains<sup>54</sup> until reaching the cathode, which will then be polarize and increase the resistivity of the whole sample. Due to this fact, it is not suitable to make measurements in a single frequency and consider it as DC regime. It is a better practice to sweep a range of frequencies and then define the DC regime as the frequency-invariant part of the plot.

The Solartron model 1260A impedance analyzer used in this work is a versatile instrument, capable of performing measurements from 10  $\mu\text{Hz}$  up to 32 MHz<sup>103</sup>. It is made of two operational modules: the generator and the analyzer. The generator sources a programmed electrical excitation to the sample, either AC voltage or current, plus desired DC bias. The generator will also be responsible for measuring the current, since it is always connected in series to the experimental cell. The analyzer essentially samples the true voltage over the sample, and correlates the phase difference between this signal and the current measured by the generator. The final pair of quantities (in this work,  $Z'$  and  $Z''$ ) are computed internally, and given to the user.

### 3.8.2. Analysis of impedance data using equivalent circuits

One of the most attractive aspects of the impedance spectroscopy is the possibility to use it as a tool to investigate electrical properties of materials by modelling it with an equivalent circuit made of discrete passive components, in accordance with the response provided by the impedance analyzer. However, the detailed modelling of all the processes that can occur in a sample-electrode system may be too complex to justify its usage in a first approach<sup>102</sup>.

Figure 24 shows a parallel RC circuit, usually employed as a common building block during the analysis of impedance spectra, and its typical response of  $Z^*$  in the complex plane. It is common to attribute a geometrical capacitance  $C$  and a bulk resistance  $R$  to samples mounted between parallel electrodes in an experimental cell.  $R$  usually denotes the conductive path of electric charges, and can relate to the conductivity of the material or even chemical reactions at the electrode interface. Similarly,  $C$  are generally related to polarized regions, adsorption processes and crystallization at the electrode<sup>102</sup>.

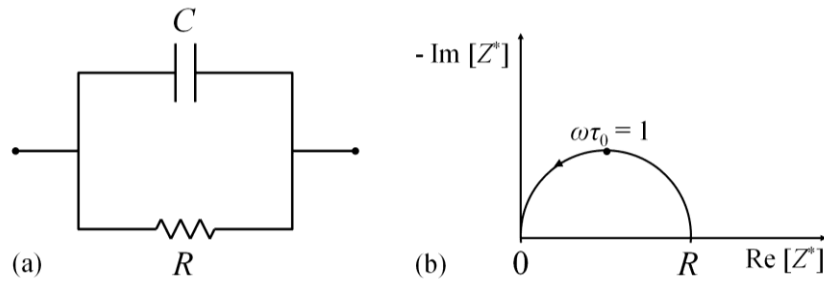


**Figure 24:** (a) Common RC parallel circuit and (b) its corresponding impedance plane.

This electrical circuit has a time constant,  $\tau_0 = RC$ , which is denoted as the dielectric relaxation of the material<sup>102</sup>. The semicircle denotes the existence of a single relaxation time, but it is very common to find several relaxation times in impedance planes of real materials<sup>104</sup>. In order to obtain a complete curve, the frequency range must be big enough around  $\omega\tau_0 = 1$ <sup>102</sup>, where  $\omega$  is the angular frequency.

In practice, however, experimental data seldom yields a complete semicircle centered in the real axis of the complex plane. There are three common perturbations<sup>102</sup>, which can still allow for the partial observation of the semicircle: i) The arc may not cross the origin because there are other arcs, or because the electrical resistance of the sample is not null at high frequencies; ii) The center of an experimental arc is frequently pushed below the real axis due to the presence of distributed elements in the material-electrode system, *i.e.* the relaxation time is not unique, but distributed around a mean value,  $\tau_m$ ; iii) The arcs may be distorted by other relaxations whose mean time constants are within two or less orders of magnitude than the arc being considered. Many experimental spectra involve such superposition of arcs.

The physical interpretation of distributed elements in an equivalent circuit is rather complex, but key for the understanding of the deepest aspects of AC electronic transport. There are two types of distributions of interest: the first directly relates with non-local processes, such as diffusion, which can even occur in completely homogeneous materials where the physical properties are the same throughout the entire sample; the second is exemplified by the constant phase element (CPE), which arises from the distribution of the microscopic properties of the materials in the sample-electrode system<sup>102</sup>.

### 3.9. Electrical measurements in direct current

Resistors are passive electrical circuit devices called linear elements because the current,  $I$ , through these devices is linearly proportional to the electric tension,  $V$ , in accordance with Ohm's Law

$$I = \frac{1}{R}V \quad (5)$$

where the resistance,  $R$ , is the constant of proportionality, and its unit is the Ohm ( $\Omega$ ).

In a direct current (DC) electrical measurement, one can obtain the value of  $R$  and the DC conductivity,  $\sigma_{DC}$ , of various materials, provided that a suitable geometric factor is known. In order to break down the analysis of the behavior of the sample, one can treat it as a combination of known circuit elements.

Electrical characterization is essential to understand the phenomena occurring in the bulk of nanomaterials. One of the challenges in the electrical characterization of these materials is the wide range of behaviors that these materials can display. As an example, polymeric materials can assume  $R$  values greater than  $G\Omega$ . However, when shaped in the form of fibers with thicknesses less than 100 nm in diameter and doped with various types of nanoparticles, a polymer can be transformed from an excellent insulator to a highly electrically conductive wire<sup>105</sup>. The result of this challenge is the need to have a wide testing range and suitable equipment to achieve accurate results.

The limits of very high and very low resistance generate small electrical signals and pose another challenge for the study of organic nanomaterials. Highly sensitive instrumentation, such as electrometers, picoammeters and nanovoltmeters, are required to detect these signals<sup>105</sup>. In this project, DC electrical measurements were carried out with a Keithley model 238 source-measure unit (SMU).

#### 3.9.1. The Keithley source-measure unit

As the name suggests, an SMU is capable of providing a constant current or a constant voltage as an excitation parameter, while simultaneously measuring the voltage or current response across its terminals, in any combination. It's a simpler and more versatile setup than



using split instruments to do the same task, and can easily acquire  $I$  vs.  $V$  curves of semiconductors and other devices <sup>106</sup>.

The SMUs have inherent characteristics of the electrometers that make them very suitable to make measurements with low excitation currents. The input resistance is generally high, in the order of 100 T $\Omega$  or more <sup>106</sup>, which minimizes overhead while probing circuits of also high impedances. Special SMUs can also achieve picoammeter sensitivities in the range of 10 fA <sup>106</sup>. In the *Laboratório de optoeletrônica e filmes finos* (UNESP - Presidente Prudente/SP - Brazil), a Keithley model 238 SMU is used to apply voltage and measure the response electrical current of devices. This instrument can operate from 100  $\mu$ V to 110 V and measure up to 1 A <sup>107</sup>.

### 3.9.2. Analysis of the $I$ vs. $V$ curves

In Materials Science, devices that present linear electrical behavior are called Ohmic, i.e. they obey the Ohm's law and thus have a similar  $I$  vs.  $V$  relationship than that of a resistor. In this case, the electrical resistance of the device can be simply obtained by the slope of this graph. If the geometric parameters of the sample are known, it's also possible to obtain its conductivity by the relation

$$\sigma = \frac{1}{R} k_{cell} \quad (6)$$

where  $k_{cell}$  is a combination of the geometric parameters of the device in question <sup>108</sup>. If the sample is simply measured in the configuration of a parallel plate capacitor (one electrode at each end), the geometric parameters are simply the thickness,  $d$ , and the effective area of the electrode,  $A$ . That being,  $k_{cell}$  is given by the ratio  $d/A$  and the unit is  $m^{-1}$ .

Another type of structure consists of depositing the material over a pre-made interdigitated set of electrodes (IDE), which will be detailed in the section 3.10.1. For this device,  $k_{cell}$  is then given by:

$$k_{cela} = \frac{2}{(N-1)L} \quad (7)$$

where  $N$  is the number of digits of the IDE, and  $L$  is the length of each digit. This relation can only be used because for the devices in this work, the spacing between the digits and their width ( $w$ ) are the same<sup>109</sup>.

### 3.10. Electrical measurements in organic thin films

The electrical characterization of organic films is fundamental for the study and evaluation of their potential application as layers in photovoltaic devices. The characterization of the P3AT films was carried out with different structures and types of electrodes. The parallel contact was obtained by the deposition of the film onto gold IDE. The perpendicular contact, diode-like structure, was obtained by the deposition of the film on top of transparent ITO electrodes and latter evaporation of aluminum on top of the film (ITO/film/Al).

DC electrical measurements were carried out with a Keithley model 238 SMU, configured to source voltage and measure the response current, in order to obtain the  $I$  vs.  $V$  curves. Photoconductivity effects were also investigated in the IDE devices, applying 5 V and collecting the time evolution of the electrical current ( $I$  vs.  $t$ ) in the dark and then under illumination from a 150 mW/cm<sup>2</sup> halogen lamp. For photoconductivity tests, the measurements were taken with samples inside a homemade dark box (Figure 25) to help mitigate the influence of external luminosity.



**Figure 25:** Experimental apparatus used to carry out electrical measurements in dark and under illumination of the halogen lamp of 150 mW/cm<sup>2</sup> power.

In order to carry out AC electrical measurements, a Solartron model 1260A impedance analyzer was employed, which is installed in the *Laboratório de Sensores e Dispositivos Orgânicos* (UNESP - Presidente Prudente/SP - Brazil), acquired with resources of the *Instituto Nacional de Eletrônica Orgânica* (INEO/CNPq - Brazil). With such equipment, impedance measurements were carried out with 100 mV AC excitation, from 1 Hz to 1 MHz. Studies of the influence of a 0 to 2.5 V DC bias superimposed to the AC signal were also carried out. The interfacing software between the instrument and the computer was the SMaRT software. The impedance spectra were analyzed by equivalent electrical circuits for the student Lucas Vinicius de Lima Citolino (UNESP - Presidente Prudente/SP - Brazil).

The organic heterojunction devices were evaluated for their possible application as photovoltaic cells and a similar procedure of the DC characterization was adopted. The procedure consists in obtaining the  $I$  vs.  $V$  curves for the devices with a Keysight B2901A Precision Source/Measure Unit in the dark and under illumination of the Oriel VERASOL solar simulator (100 mW/cm<sup>2</sup> – AM 1.5), shown in Figure 26. The devices were made of organic materials deposited in planar heterojunctions between ITO and Al electrodes, similar to a diode-like configuration, as described before for the electrical characterization of P3AT films.



**Figure 26:** Experimental apparatus used to carry out photovoltaic measurements in dark and under illumination of the Oriel VERASOL solar simulator (100 mW/cm<sup>2</sup> – AM 1.5).

### 3.10.1. Parallel contact: interdigitated electrodes

Electrical measurements on IDE are commonly used due to the low conductivity of the materials to be studied, because the total current is amplified by the number of pairs of digits

in each electrode. Use of this type of electrode in this work is very interesting, not only for assisting the electrical characterization of organic materials that are candidates to active layers, but also to be possible to be made previously, thus avoiding the difficulties found in the fabrication of the diode-like devices, which will be further discussed.

The gold IDE were fabricated (Project LMF n° 16557) in the *Laboratório de Microfabricação* (LNNano/CNPEM - Campinas/SP - Brazil). Their parameters are  $N = 50$  digits with 110 nm height ( $h$ ), 8 mm length ( $L$ ) and 100  $\mu\text{m}$  width ( $w$ ), as depicted in Figure 23 (however with  $N = 10$  for the sake of clarity). According to this geometry,  $k_{\text{cell}}$  is  $\sim 5.1 \text{ m}^{-1}$

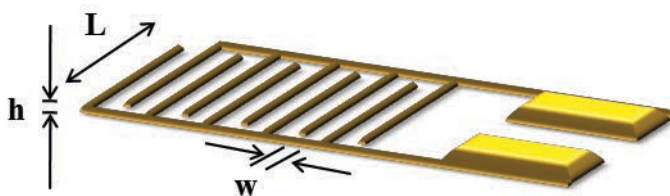


**Figure 27:** Schematic representation of an interdigitated electrode being  $N = 10$  digits, height  $h$ , length  $L$  and  $w$  the width of digits.

The photolithography was the method of choice to record the IDE-Au onto glass substrates. It is based on the selective etching of a thin film in a substrate. UV radiation is used to transfer a pre-determined geometric pattern of a mask to a photosensitive chemical compound (photoresist), which has been previously deposited onto the substrate<sup>52,110</sup>. This pattern allows a subsequent deposition of another material in the pattern of choice, as it won't attach to the substrate in the areas where the photoresist is present. The steps for the photolithography process are listed below:

- a) Cleaning of the glass substrates using an ultrasonic bath at 50 °C with deionized water and Extran soap for 5 minutes;
- b) Submersion of the substrates in a piranha solution, followed by bath with deionized water and subsequent heating at 120 °C for some minutes to allow it to dry;
- c) Application of HMDS using a spinner at 3000 rpm for some seconds;
- d) Application of Clariant AZ 4210 photoresist using a spinner at 3000 rpm for 30 seconds;
- e) Heating of the substrate with photoresist in a warm plate at 95 °C for 5 minutes to speed up solvent evaporation;

- f) Application of the acetate photomask and substrate assembly under 300 W UV radiation for 20 to 30 seconds. During this step, the photoresist will be exposed to light and the pattern of the photomask will be transferred to it. A Karl Süss MJB3 photoaligner was used to align the mask to the substrate, and can be seen in Figure 28(a);

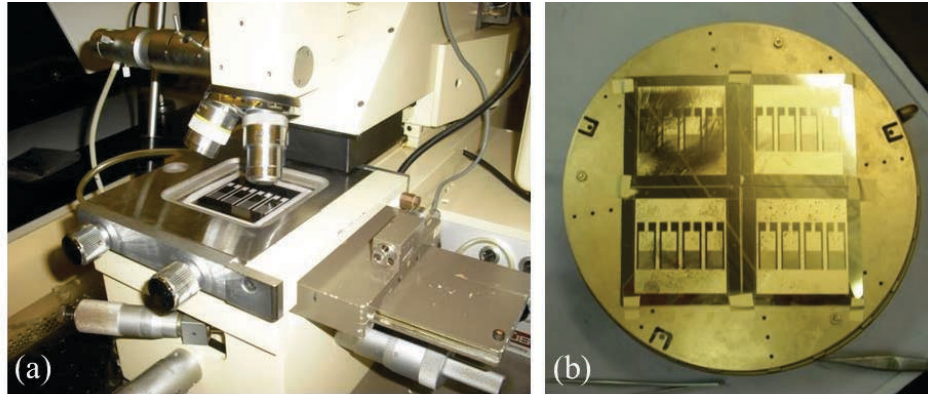


**Figure 28:** (a) Photoaligner used to expose the photoresist to UV light. (b) Metal film deposited onto the glass substrates, with patterns previously formed by the presence of the photoresist.

- g) The development of the photoresist is made by dipping the substrate in Clariant K400 developer during 30 seconds;
- h) After the development, the substrates were exposed to Oxygen plasma from a Barrel Asher Plasma Technology SE80 to remove possible residues and assure good adhesion of the metal to be deposited later. The exposure to plasma takes 3 minutes, and is carried on in a 100 mTorr chamber and 100 W power;
- i) The metallic layers were deposited by sputtering using a Balzers BA510 sputtering equipment. The metallic film is composed of a 30 nm Chromium (Cr) layer to facilitate the adhesion of other metals, and a second 80 nm layer of Gold (Au). Some of the metallized substrates can be seen in Figure 28(b);
- j) The last step is called lift-off, when the glass substrates are submerged in acetone for one hour to remove the photoresist that served as the mold for the metallic electrodes. The metal film that was attached onto the photoresist is also removed in this step, and only the metal film that has been in direct contact to the glass remains.

Each glass slide will yield 4 IDEs which will be later separated by cutting the glass with a diamond tip. This detail and the lift-off process can be seen in Figure 29. Before usage, the electrodes were cleaned by boiling them in acetone and isopropyl alcohol.



**Figure 29:** Lift-off step under acetone, to remove the photoresist and metal film, the last process of the fabrication of the IDE.

### 3.10.2. Perpendicular contact: diode-like structure

The perpendicular contact (diode-like structure) was obtained by deposition of the film onto a transparent electrode (ITO) and later evaporation of aluminum onto the film, giving rise to an ITO/film/Al structure. It was used for both the electrical characterization of the materials and for the assembly of the photovoltaic devices. The glass substrates covered with ITO were manufactured by Delta Technology.

A big challenge of producing such diode-like devices is the possibility of a short circuit between the electrodes due to the thin thickness of the organic material film. In order to mitigate this problem, the ITO layer was submitted to a process of partial removal, which consists of depositing zinc powder and hydrochloric acid (HCl 1 M) in a certain region of the ITO. A reaction then takes place, and leads to the formation of zinc chloride ( $\text{ZnCl}_2$ ). In this region,  $\text{ZnCl}_2$  reacts with ITO, forming salts of indium and tin that are soluble in water.

After partially removing the ITO, the substrates were cleaned with boiling acetone and dried with boiling isopropyl alcohol. At this point, the substrates are ready to receive the film of organic material by the deposition techniques presented in section 3.1. After the deposition of the organic film, the top metallic (Al) electrodes were then evaporated using a patterned mask and a Boc Edwards model Auto 306 Evaporation System, installed at *Departamento de Física, Química e Biologia* (UNESP - Presidente Prudente/SP - Brazil) under the responsibility of Prof. Dr. Carlos J. L. Constantino. The thickness and effective area of the aluminum layer were  $\sim 60$  nm and  $0.12$  cm<sup>2</sup>, respectively.

Figure 30 shows the final structure of the device, making it clear the importance of the partial removal of the ITO. As the thickness of the film is in the order of magnitude of

nanometers, the negative pole that runs through the organic film would short with the ITO if it was not removed from a certain region. Although this effect was mitigated, it can still happen during the evaporation of the Al electrode.

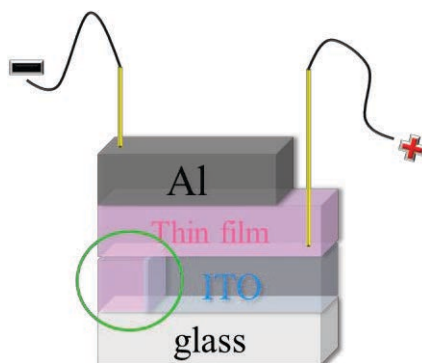


**Figure 30:** Schematic view of an ITO/film/Al, showing how the electrical contacts are made. The circled region emphasizes the area where the ITO was partially removed.

### 3.10.3. Photovoltaic devices in planar heterojunction

Several steps have to be accomplished in order to build OPV devices. Onto ITO surfaces it is common to use an anode buffer layer such as poly(3,4-ethylenedioxythiophene) polystyrene sulfonate (PEDOT:PSS),  $V_2O_5$ ,  $MoO_3$ ,  $WO_3$  or NiO, in order to provide effective charge collection and also improve smoothness the ITO surface to remove potential pinholes<sup>111</sup>. After the anode buffer layer deposition, the donor and acceptor layers are deposited, respectively, in order to form a planar heterojunction. Onto the organic layer is often deposited a cathode window layer that acts to block excitons from quenching at the cathode, protect the active layers from damage during the cathode deposition, reduce Schottky barriers for improved charge collections and extend the lifetime of the device<sup>6</sup>. Lastly the top electrode should be deposited.

In this research, the first step was the partial removal of the ITO, as mentioned for the diode-like structure. Then, the PEDOT:PSS (Sigma-Aldrich) was deposited by spin-coating (3000 rpm - 60 seconds)<sup>112</sup> onto ITO substrates. The PEDOT:PSS solution was annealed at 100 °C for 10 minutes<sup>113</sup>. The donor layer (P3BT, P3HT, P3OT or P3DT) was deposited by spin-coating or LS technique followed by the PVD deposition of the acceptor layer (BuPTCD), providing a planar heterojunction also known as bilayer<sup>60</sup>. The P3AT derivatives were grown to provide ~100 nm while the BuPTCD ~50 nm thickness. The LiF was deposited by PVD as cathode window layer (1.5 nm)<sup>114,115</sup> on top of some heterojunctions, in order to



evaluate the differences obtained for the OPV devices with and without LiF. The Al layer was deposited onto the complete structure, as mentioned for the diode-like structure. The Figure 31 shows the schematic representation of the OPV devices in planar heterojunctions (ITO/PEDOT:PSS/P3AT/BuPTCD/Al). Preliminary tests were conducted in similar structures using fullerene- $C_{60}$  deposited by PVD instead of BuPTCD and without any anode buffer layer (ITO/P3AT/ $C_{60}$ /Al).

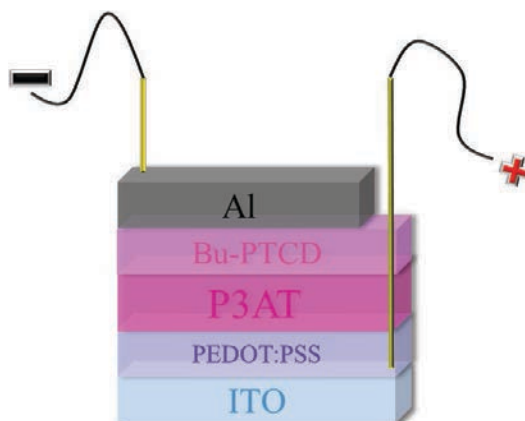


**Figure 31:** Schematic representation of the OPV devices forming planar heterojunctions between thin films of P3AT derivatives (spin-coating or Langmuir-Schaefer deposition providing ~100 nm thick) and BuPTCD (PVD deposition providing ~50 nm thick).



## CHAPTER 4: Thin films of alkyl-substituted polythiophene derivatives

### 4.1. P3AT Langmuir films

The  $\pi$ -A isotherms for regioregular P3AT studied are shown in Figure 32. In addition, the inset in Figure 32 shows pictures of two important phases for the P3OT: the condensed phase and the Langmuir film collapse. It was possible to estimate the collapse pressure of the Langmuir films in descending order according to the increase of carbon number in the side chain, around 75, 70, 66 and 65 mN/m for P3BT, P3HT, P3OT and P3DT, respectively. Around 25 mN/m it is possible to observe a change in the slope of the  $\pi$ -A isotherm of P3HT, P3OT and P3DT monolayers. P. Yli-Lahti *et al.* observed the same effect in isotherm slope above 30 mN/m to Langmuir films of P3OT with arachidic acid<sup>116</sup> and it could be explained as a molecular reorganization of the film.

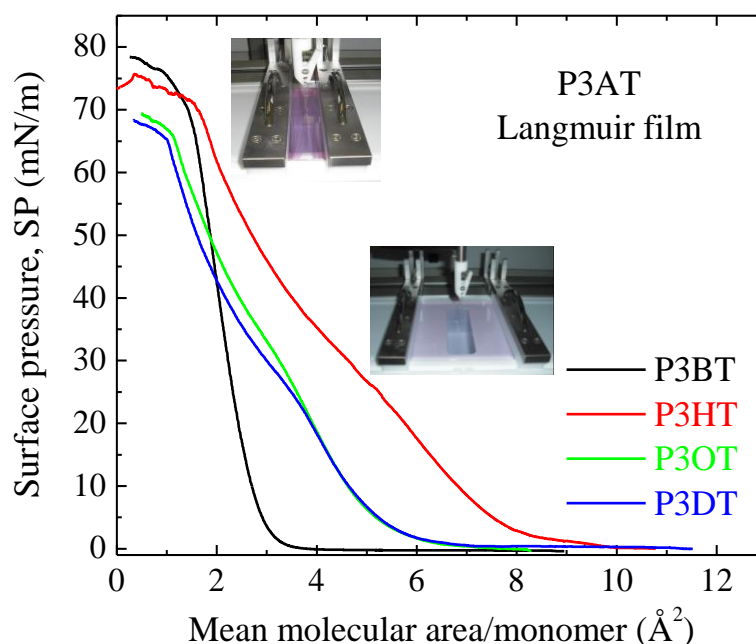


**Figure 32:**  $\pi$ -A isotherms for regioregular P3AT: P3BT, P3HT, P3OT and P3DT. In the inset, pictures of P3OT Langmuir film showing the condensed phase and the collapse of the film.

The mean molecular areas per monomer calculated from the condensed phase were 2.7, 8.0, 5.2 and 5.3  $\text{\AA}^2$  for regioregular P3BT, P3HT, P3OT and P3DT, respectively. Some studies report a variance on the mean molecular area per monomer in polythiophene derivatives from 14.7 to 28  $\text{\AA}^2$ . It shows dependence on the angle between the thiophenic ring and the aqueous subphase, where the area would be the largest for the case in which the ring

is parallel ( $0^\circ$ ) to the subphase and the lowest for the perpendicular case ( $90^\circ$ )<sup>30,117</sup>. Small molecular areas per monomer obtained for P3BT, P3HT, P3OT and P3DT show that these polythiophene derivatives do not form true monolayers at air-water interface, probably because just a small portion of the polymeric chain is in contact with the water surface<sup>32</sup>. Changes in the molecular arrangement of the polymer during the barrier compression may bend the side or main chain part, thus enabling the formation of multilayers<sup>118</sup> alternating different composition and characteristics.

Although the inset in Figure 32 shows an homogeneous aspect of the film in the condensed phase on a macroscopic scale, the images captured using BAM technique during the condensed phase from each regioregular P3AT (Figure 33) show the formation of aggregates at the air-water interface for the Langmuir films. D. R. Greve *et al.* obtained BAM images of the Langmuir film of poly(4-dodecyl-2,2'-bithiophene) in different stages of the film compression<sup>31</sup>. They showed that large domains (aggregates) are formed immediately after spreading the solution on the water surface and these domains do not disintegrate with time, however, upon film compression, these domains come together to form a continuous film. Nevertheless, as demonstrated in this study, even in compressed condensed phase the film consists of a large number of defects and imperfections. The condensed phase is also the one in which the Langmuir film is deposited onto a solid substrate. It was not possible to deposit Langmuir-Blodgett films due to the high rigidity of the regioregular P3AT Langmuir film formed on the water subphase<sup>31</sup>. For this reason, the Langmuir films were transferred to hydrophobic substrates by horizontal deposition (Langmuir-Schaefer technique).

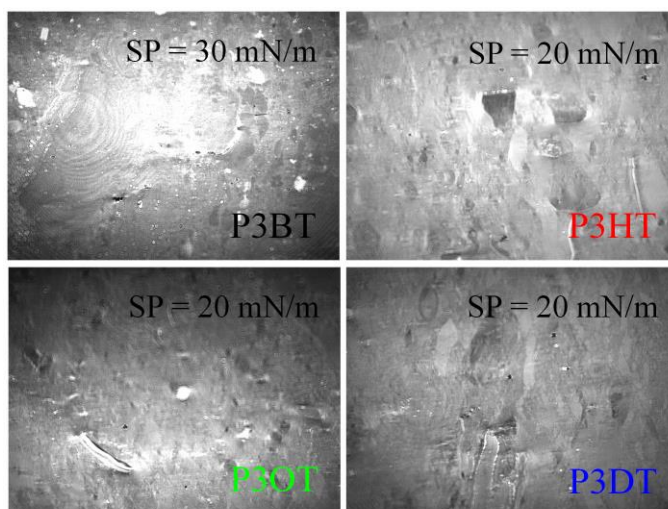


**Figure 33:** BAM images of Langmuir films for regioregular P3AT at deposition pressures: SP = 30 mN/m for P3BT and SP = 20 mN/m for P3HT, P3OT and P3DT.

## 4.2. Spin-coated and Langmuir-Schaefer films of P3AT

### 4.2.1. UV-visible absorption

The UV-visible absorption spectra for spin-coated and LS films of regioregular P3AT are shown in Figure 34 (a) and (b), respectively. The  $\lambda_{\max}$  were 490, 517, 518 and 513 nm, for spin-coated films of P3BT, P3HT, P3OT and P3DT, respectively. The P3BT also shows a blue shift in comparison to the other ones, which could mean a less ordered film<sup>119</sup> in relation to the other regioregular derivatives deposited by spin-coating. These values of  $\lambda_{\max}$  are similar to the ones found in literature for thin films of the regioregular P3ATs<sup>120–122</sup>.

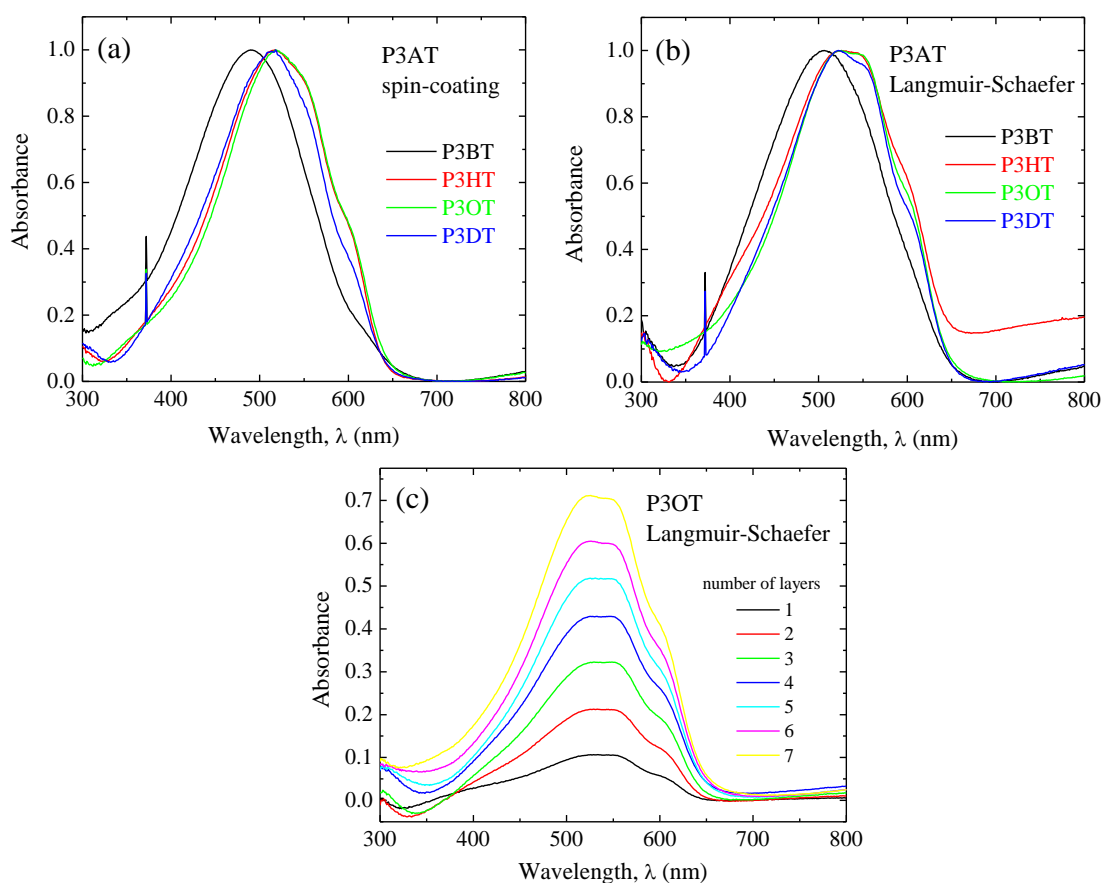


**Figure 34:** Absorption spectra in the UV-visible range for P3AT thin films deposited by (a) spin-coating and (b) LS onto an ITO substrate. (c) UV-visible spectra performed during the growth of seven layers for P3OT LS film.

In conjugated polymers, likewise polythiophene derivatives, the conjugation directly affects the observed energy for the  $\pi$ - $\pi^*$  transition, that shows itself as an absorption maximum in these materials<sup>121</sup>. The band position and intensity data can only be used as an approximation for identification purposes, since both are influenced by effects of the solvent

<sup>123</sup> and also by other structural features of the molecule. Nevertheless, the conjugation between two or more chromophores tends to cause shifts in the absorption peak at higher wavelengths <sup>95</sup>. Finally, vibrational effects broaden the absorption bands in the ultraviolet and visible ranges, which usually make it difficult to precisely determine the absorption peak <sup>95</sup>.

Besides the maximum absorption wavelength, it is also possible to observe not so well defined shoulders in the spectra of regioregular P3HT, P3OT and P3DT, as it was also observed by other authors <sup>39,121,122</sup>. R. C. Hiorns *et al.* have also observed the presence of such shoulders in the absorption band for the P3HT (544 and 602 nm) whereas for the P3BT only one absorption peak was observed (480 nm) <sup>39</sup>. Rughooputh *et al.* have suggested that these shoulders appear due to vibrational stretching transitions involving carbons double bonds in the thiophene ring <sup>124</sup>, and this hypothesis is well accepted by the scientific community <sup>125,126</sup>. According to R. D. McCullough, these shoulders can be related to a long range ordered structure, which gives rise to longer conjugation lengths <sup>121</sup>.

The spectra for P3AT LS films (Figure 34 (b)) show  $\lambda_{\text{max}}$  at approximately 506, 526, 526 and 522 nm for P3BT, P3HT, P3OT and P3DT, respectively, and these results differ only by a few nanometers of red shift in relation to those spin-coated films, but remain in accordance to the values obtained for the ones found in the literature for the thin films of the regioregular polythiophene derivatives.

According to G. Dicker *et al.*, highly ordered films exhibit red shifts of the  $\pi$ - $\pi^*$  band <sup>119</sup>, which itself indicates higher ordering of the LS films as compared to the ones obtained by spin-coating. In opposition to the spin-coated films, for the LS films of P3HT, P3OT and P3DT it was observed a broadened absorption maximum, which possibly happens due to the presence of not only one, but two slightly overlapped absorption bands. Nevertheless, the regioregular P3AT deposited by the LS technique showed not very well defined shoulders at higher wavelengths, as already discussed for the films obtained by spin-coating of these same polymers.

K. Kanai *et al.* also observed the development of additional bands in the absorption spectra in the UV-visible range and higher definition of the already existing ones after thermal treatment of regioregular P3HT films <sup>127</sup>. The explanation to the fact is that the main polymer chain becomes a well-ordered structure after annealing, due to the formation of a more lamellar structure, which ensures a long  $\pi$  conjugation along the polymer chain. It is possible to relate the appearance of a new absorption band in the UV-visible range of the spectrum to a more ordered structure provided by the LS technique, as compared to the spin-coating. Higher

$\sigma_{DC}$  should be expected from highly ordered films<sup>22</sup>, and this is to be comparatively shown throughout this paper.

The accurate control of the deposition process of thin films deposited by techniques that involve more than one layer deposition step, such as layer-by-layer, Langmuir-Blodgett and LS is necessary to ensure the growth of a linear and uniform film onto the substrate. Figure 34 (c) shows the absorption spectra in the UV-visible range for the LS film of regioregular P3OT grown with seven layers onto an ITO substrate. The linear growth of the absorption indicates that similar amount of material was deposited onto the substrate in each deposition step, and this result has also been observed for the other P3AT derivatives.

With the aim to observe a possible molecular organization induced by the compression of the film in the Langmuir trough, transmitted to the substrate by the LS technique, polarized optical absorption measurements were carried out. M. Rikukawa *et al.* showed the optical anisotropy for the LB film of P3HT and stearic acid (2:1), evidencing its molecular organization<sup>128</sup>. The optical anisotropy could explain the raise of the electrical conductivity for most of the regioregular P3AT derivatives deposited by the LS technique, when compared to the ones obtained by spin-coating. Two different polarizations of the incident light were used: with the electric field parallel and perpendicular to the direction of deposition. For reference, the deposition was carried out with the substrate placed perpendicularly to the barriers of the Langmuir through. Figure 35 shows the results for the absorption spectra with polarized light for films of the P3BT, P3HT, P3OT and P3DT derivatives, which did not present any meaning difference between the results.

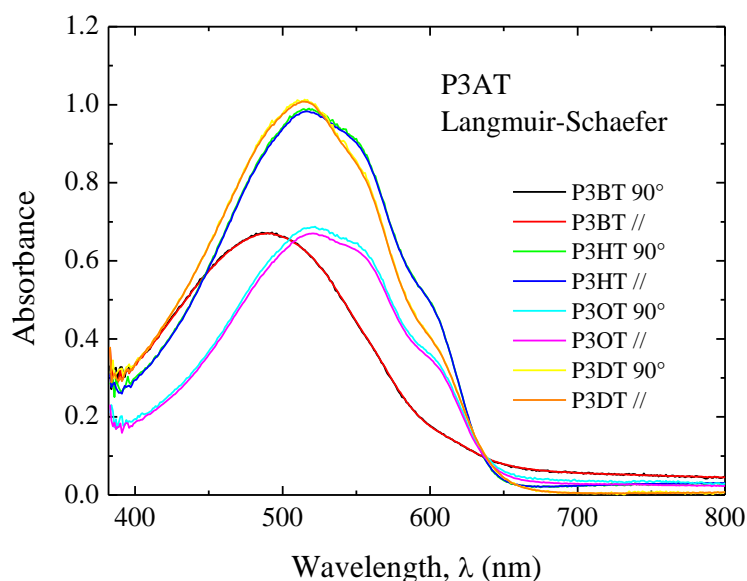


**Figure 35:** Optical absorption spectra with polarized light for the LS devices of P3AT.

#### 4.2.2. Photoluminescence spectroscopy

Luminescence measurements were carried out by exciting each material with its corresponding  $\lambda_{\text{max}}$  as obtained by the optical absorption measurements, therefore obtaining its respective emission spectrum. The luminescence spectra for the regioregular P3BT, P3HT, P3OT and P3DT, deposited by (a) spin-coating and (b) LS are shown in Figure 36. The wavelength related to the photoluminescence peak, as in the absorption in the UV-visible range, also called  $\lambda_{\text{max}}$ , were 614, 652, 662 and 661 nm for the spin-coated films and 634, 655, 661 and 662 nm for the LS films of P3BT, P3HT, P3OT and P3DT, respectively. The obtained data was similar regardless of the film deposition technique, presenting only a few nanometers deviation, except for the P3BT which presented a 30 nm shift to higher wavelengths for the LS film when compared to the spin-coated one. Besides the maximum wavelength peak, it is also possible to notice shoulder peaks at higher wavelengths for the P3AT derivatives.

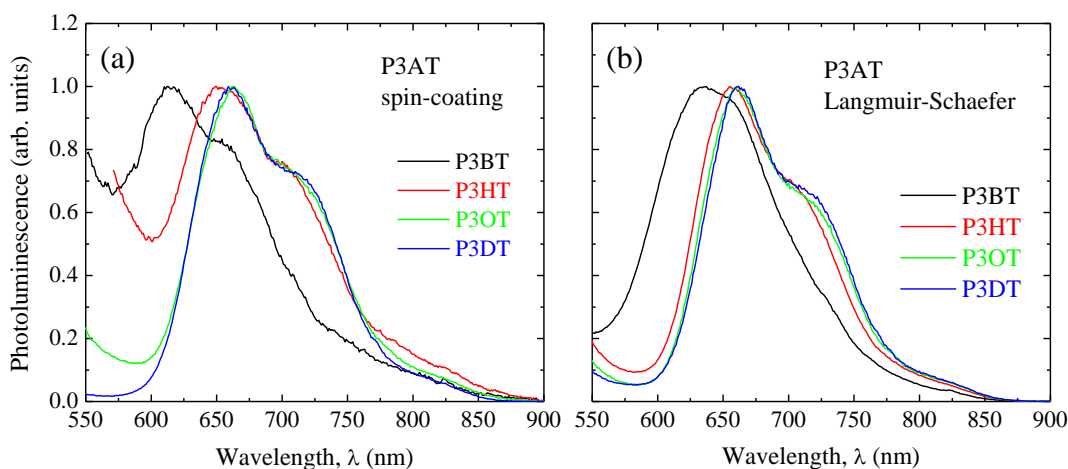


**Figure 36:** Photoluminescence spectra for regioregular P3AT films deposited by (a) spin-coating and (b) LS technique.

The shapes of the photoluminescence spectra were similar to the ones found in literature for the P3AT<sup>129–131</sup>, and they both agree on the peak position and the presence of a shoulder at higher wavelength. J. Clark *et al.* have shown the emission in regioregular P3HT results from the weak coupling of H aggregates, without any significant contributions of the excitons inside the chains<sup>132</sup>. The H aggregates are coherent with the structural organization of the P3HT film<sup>133</sup> which has semi-crystalline structure with layers of thiophenic rings

stacked chain by chain ( $\pi$ -stack) alternated with alkyl side chains, inferred by T. J. Prosa *et al.* from X-ray diffraction<sup>134</sup>, as shown in Figure 37.

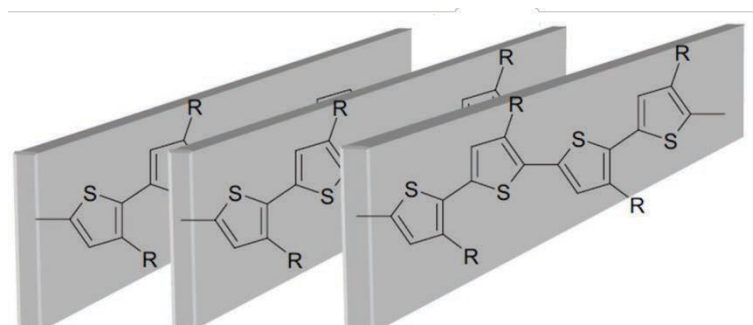


**Figure 37:**  $\pi$ -stacks of the regioregular P3AT, where R represents an alkyl group. Adapted from<sup>133</sup>.

#### 4.2.3. AFM morphology

The nanoscale morphology of the films was determined by AFM in the contact mode. Figure 38 contains AFM topographic images for the regioregular P3AT (a) spin-coated films for an area of  $25\ \mu\text{m} \times 25\ \mu\text{m}$  and (b) LS films for an area of  $20\ \mu\text{m} \times 20\ \mu\text{m}$ . Figure 38 (a) also presents the roughness values,  $R_q$ , for the spin-coated films, these being 10.8, 2.84, 2.45 and 2.10 nm and of 11, 2.2, 2.5 and 1.6 % in relation to the thickness for the P3BT, P3HT, P3OT and P3DT, respectively. The images reveal homogeneous surfaces, and the highest roughness was obtained for the P3BT film, in which the presence of aggregates is easily visible (clearer spots), possibly due to the solution used to prepare the thin film, which solubilizes less effectively in chloroform.

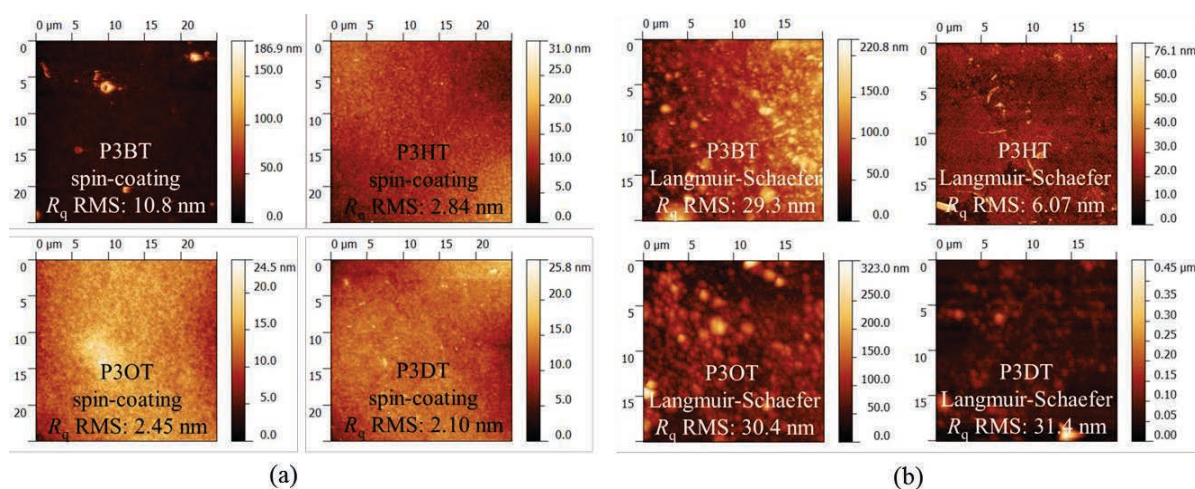


**Figure 38:** AFM topographic images of the films of P3BT, P3HT, P3OT and P3DT deposited by (a) spin-coating and (b) LS techniques onto ITO substrate. The roughness values  $R_q$  are contained inside of each image.



P. Gangopadhyay *et al.* have obtained roughness less than 6 nm for the spin-coated film of poly(3-dodecylthiophene) (P3DDT) regioregular with 1  $\mu\text{m}$  thick<sup>135</sup>, characterizing a highly homogeneous film. J. Clark *et al.* have obtained 0.95 and 5.7 nm roughness for spin-coated films with 10 and 50 nm thick obtained from the P3HT solution in chloroform and isodurene, respectively, demonstrating that the roughness of the film is also influenced by the boiling point of the organic solvent used in the solution<sup>136</sup>.

In Figure 38 (b) one can see not only the AFM topographic images for the regioregular P3AT films deposited by LS, but also the values of  $R_q$  of 29.3, 6.07, 30.4 and 31.4 nm and of 41, 3, 22 and 14 % relative to the thickness of the films deposited on ITO of P3BT, P3HT, P3OT and P3DT, respectively. The images reveal non-homogeneous surfaces with large amount of aggregates and these results agree with the BAM images in the Langmuir trough.

M. Ferreira *et al.* have obtained similar results when comparing LB and cast films of a PPV derivative (polyphenylenevinylene)<sup>137</sup>. In this latter case, although the cast film thickness was three times greater, its roughness was around two times lower as compared to the LB film. The authors explain this result by the presence of side chains in the polymer, which can align perpendicularly to the substrate during the LB deposition, resulting in a higher roughness of the film. C. P. L. Rubinger *et al.* have also evaluated AFM images for the films of poly(5-amino-1-naphthol) deposited by LB and LS and the images show that the LS ones had higher homogeneity and planarity than the ones deposited by LB<sup>138</sup>. Both Langmuir techniques could not be compared in this work, since it was not possible to deposit LB films of the neat regioregular P3AT.



## CHAPTER 5: Electrical properties of thin films

### 5.1. Electrical measurements in IDE devices

The results of DC electrical measurements on regioregular P3AT films deposited by spin-coating and LS onto IDE show that the current increases as a function of the applied voltage ( $I$  vs.  $V$ ) in a linear way, as seen in Figure 39. This result characterizes the ohmic behavior<sup>139</sup>, possibly related to the Au/P3AT/Au contact interface. Therefore, from  $I$  vs.  $V$  curves it is possible to estimate the electrical resistance  $R$  of the deposited film in this specific type of structure and a model from W. Olthuis *et al.*<sup>108</sup> allows to obtain the related  $\sigma_{DC}$ . The cell constant accounts for the digit height, spacing, number and length<sup>108</sup> and for the IDE utilized in this paper the calculated value was  $5.1 \text{ m}^{-1}$ <sup>80</sup>.

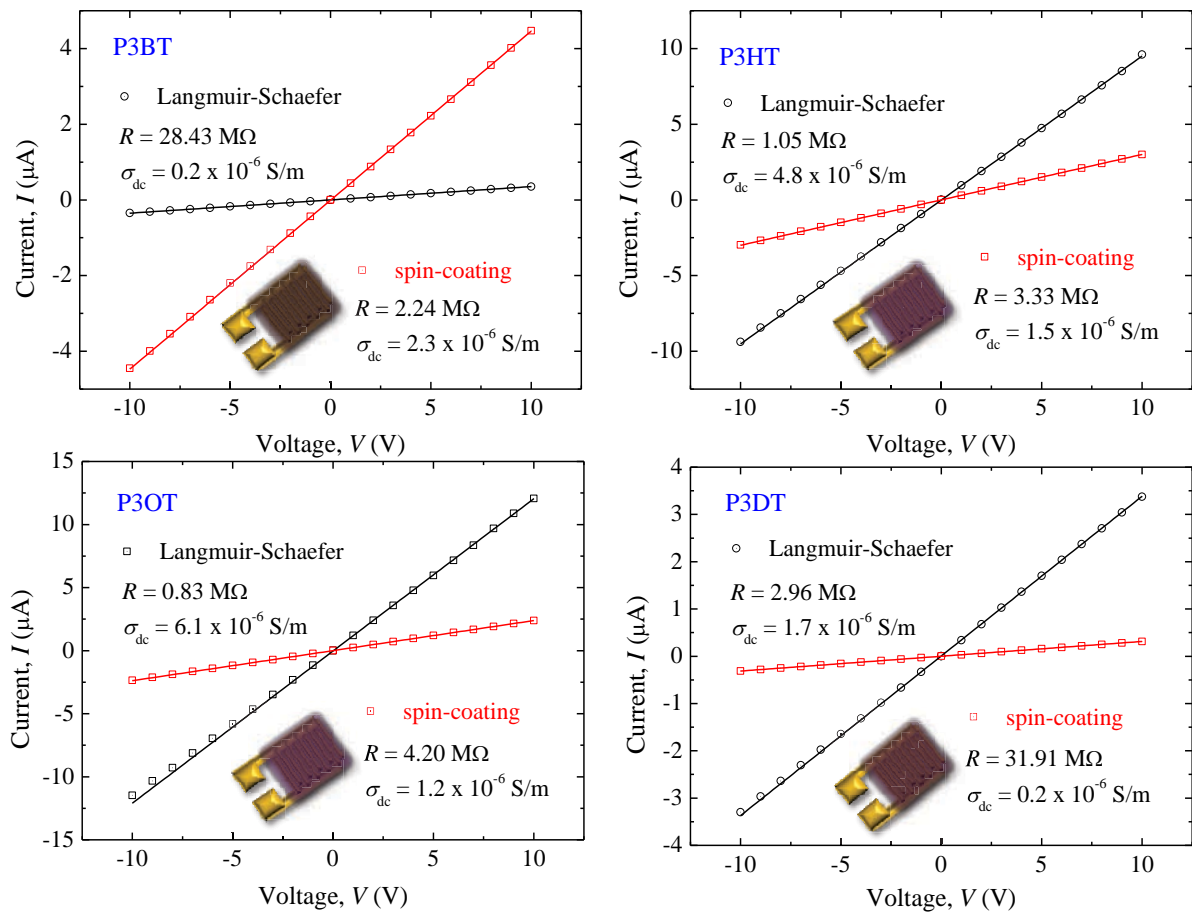


**Figure 39:**  $I$  vs.  $V$  electrical measurements of the regioregular P3AT comparing LS and spin-coating techniques.

The values of  $\sigma_{DC}$  were obtained from  $I$  vs.  $V$  plots for P3BT, P3HT, P3OT and P3DT spin-coated films resulting in  $2.3 \times 10^{-6}$ ,  $1.5 \times 10^{-6}$ ,  $1.2 \times 10^{-6}$ ,  $0.2 \times 10^{-6}$  S/m, respectively.

Although these values are quite close to each other, there is a trend in the data showing the  $\sigma_{DC}$  decrease for longer alkyl side chains of P3AT derivatives in spin-coated films, as already observed by J. Roncali *et al.*<sup>140</sup> for electrochemically deposited films. Conductivity decreases progressively with the size of the interchain spacer (alkyl side chain) probably due to a less efficient three-dimensional packing of the polymer main chains<sup>141</sup>, thus hindering hopping<sup>142</sup>.

R. K. Singh *et al.* and J. Kumar *et al.* have measured the conductivity of polythiophene deposited by casting onto gold substrate in a diode-type structure (Au/P3AT/Au) and have found  $2.33 \times 10^{-6}$  S/m<sup>143</sup> and  $1.1 \times 10^{-6}$  S/m<sup>144</sup> for the P3HT and P3OT, respectively, which are at the same order of magnitude of the measurement for P3BT, P3HT and P3OT presented in this paper. However, these values are slightly lower than the ones reported by T.-A. Chen *et al.* for thin films of the P3AT in electrical measurements taken using two tips in pressure contacts ( $10^{-5}$  to  $10^{-4}$  S/m)<sup>145,146</sup>.

The values of  $\sigma_{DC}$  were calculated for the LS films of P3BT, P3HT, P3OT and P3DT resulting in  $0.2 \times 10^{-6}$ ,  $4.8 \times 10^{-6}$ ,  $6.1 \times 10^{-6}$  and  $1.7 \times 10^{-6}$  S/m, and these are higher than the ones obtained for spin-coated films onto IDE, except for the P3BT which presented a lower electrical conductivity for the LS film. This fact can be explained by the difficulty to deposit regioregular P3BT onto glass substrates coated by gold IDE.

Therefore, the *I vs. V* characterization for the IDE devices have shown that the LS films of the regioregular P3AT yield lower electrical resistance and hence higher conductivity than the same materials when deposited by spin-coating. The higher conductivity of the materials that were deposited by LS compared to the spin-coated ones is possible related to i) the organization of the LS films down to molecular level, as observed by UV-visible absorption spectroscopy and ii) the higher LS film roughness as observed by AFM. The calculated values of  $\sigma_{DC}$  are shown in Table 1.

**Table 1:** Electrical properties of P3AT films deposited by spin-coating and LS techniques.

	spin-coating		Langmuir-Schaefer	
	<i>R</i> (M $\Omega$ )	$\sigma_{DC}$ (S/m)	<i>R</i> (M $\Omega$ )	$\sigma_{DC}$ (S/m)
P3BT	2.24	$2.3 \times 10^{-6}$	28.43	$0.2 \times 10^{-6}$
P3HT	3.33	$1.5 \times 10^{-6}$	1.05	$4.8 \times 10^{-6}$
P3OT	4.20	$1.2 \times 10^{-6}$	0.83	$6.1 \times 10^{-6}$
P3DT	31.91	$0.2 \times 10^{-6}$	2.96	$1.7 \times 10^{-6}$

After the DC electrical characterization of the LS films deposited on IDE, a systematic study of the photoconductivity was carried out, aiming to evaluate the applicability of such materials as an electron donor in photovoltaic devices of organic heterojunctions. The electric current enhancing due to the light exposure (photoconductivity effect), is basically related to the photogenerated excitons diffusing through the organic layer<sup>147</sup>. However, the photocurrent measured depends not only on the photogeneration of charge carriers into the bulk, but as well on the charge carrier mobility and on the photoinjection from the illuminated electrodes<sup>148</sup>.

Figure 40 shows the  $I$  vs.  $t$ , in dark and illuminated conditions when 5 V are applied to the LS films of regioregular P3AT on IDE. The four derivatives presented an increase of the current ( $\Delta I = I_{\text{light}} - I_{\text{dark}}$ ) when illuminated, and the values of  $\Delta I$  are 0.33, 5.10, 8.87 and 1.70  $\mu\text{A}$ , for the P3BT, P3HT, P3OT and P3DT, respectively. The lowest increase of the current for the P3BT as compared to the others is possibly related to the inefficient deposition of this compound on the IDE, as well as observed for the  $I$  vs.  $V$  results for this same device.

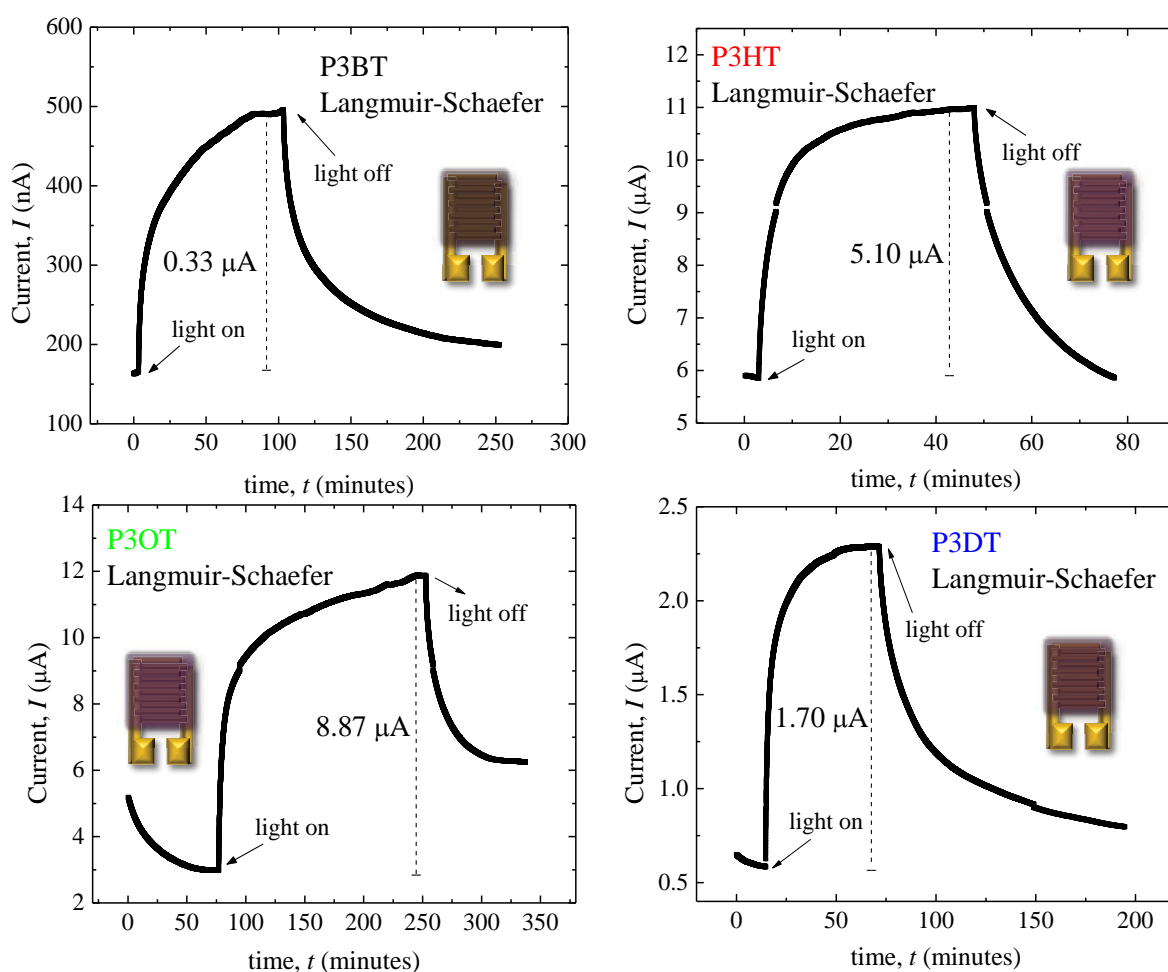


**Figure 40:**  $I$  vs.  $t$  plots in dark and illuminated conditions of P3BT, P3HT, P3OT and P3DT LS films on IDE.

According to the Su-Schrieffer-Heeger (SSH) model, photoexcitations through the  $\pi$ - $\pi^*$  band gap would create free carriers (both electrons and holes) which self-organize to build up nonlinear excitations in conducting polymers: solitons, polarons and bipolarons, depending on the ground state degeneracy<sup>49</sup>. Z. Vardeny *et al.* employed steady-state photoinduced absorption spectroscopy and light-induced electron-spin resonance to show that the photoconductivity effect in polythiophenes is due to the photogeneration of bipolarons in neutral polythiophenes<sup>149</sup>. The existence of bipolarons during the photoexcitation or after a doping process implies that an attractive indirect interaction exists between two equal charges, due to the generation of a local structural distortion<sup>149</sup>.

When the light is turned off, the photogenerated excitons diffuse through the organic layer until they dissociate at a defect site or at a metal/organic-layer interface<sup>147</sup>, causing a decay of the photocurrent in the  $I$  vs.  $t$  plots. After the fast initial decrease, the current reading slowly decays and approaches the value obtained under dark condition for most of the polymers, except for the P3OT which may have degraded and changed its properties under illumination. The slow decay of the current features the persistent photoconductivity, a phenomenon where the conductivity remains high for a while even after light exposure, which has already been observed in organic semiconductors by several groups<sup>150–152</sup>. According to C. H. Lee *et al.* the persistent photoconductivity is caused by the slow diffusion of the photogenerated bipolarons to an interface, where they are dissociated into polarons<sup>150</sup>.

## 5.2. Electrical measurements in ITO/P3AT/Al devices

Figure 41 shows the results of the DC electrical characterization for the ITO/P3AT/Al devices of P3BT, P3HT, P3OT and P3DT deposited by spin-coating and LS techniques. In order to compare the results for films with different thicknesses,  $d$ , the electric field moduli  $F = V/d$  were calculated<sup>153</sup>. The  $I$  vs.  $F$  plots shown in Figure 41 reveal a diode-like behavior, possibly due to the formation of a Schottky barrier<sup>154</sup>, which is the result of the formation of defects in a metal-semiconductor interface<sup>155,156</sup>. For the ITO/P3AT/Al devices of spin-coated films, the current onset in direct polarization for P3BT and P3HT are at low  $F$  and close to each other, whereas the P3OT shows the less significant current increase. For the devices of LS films, the ITO/P3HT/Al stands before the others, once the current onset is at the lowest  $F$ .

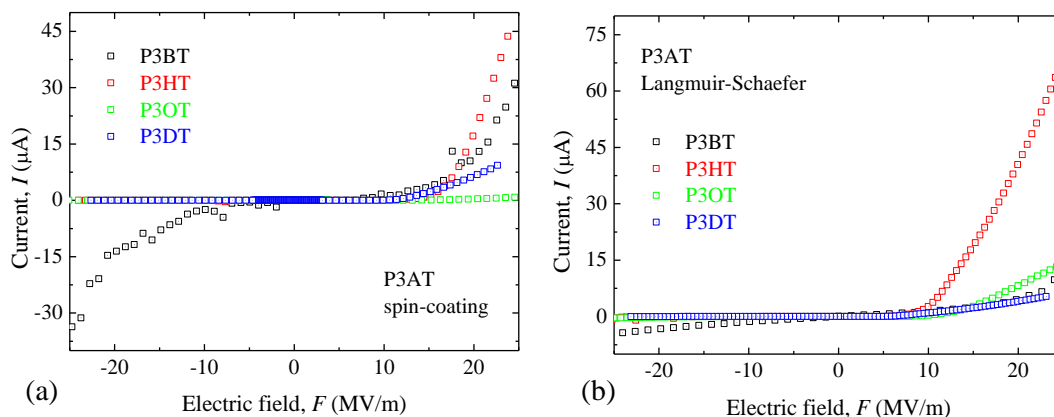


**Figure 41:**  $I$  vs.  $F$  plots for the ITO/P3AT/Al devices, where P3BT, P3HT, P3OT and P3DT were deposited by (a) spin-coating and (b) LS techniques. Image from <sup>157</sup>.

The results for different polymers and deposition technique were also compared by means of the rectification factor of  $I$  vs.  $F$  plots, which is the ratio between the electrical current in direct and reverse polarization. The rectification factors calculated at  $\sim 20$  MV/m resulted in 1, 5500, 2100 and 17000 for the ITO/P3AT(spun-coating)/Al devices and in 1, 790, 43 and 310 for the ITO/P3AT(LS)/Al devices of P3BT, P3HT, P3OT and P3DT, respectively. The ITO/P3AT/Al devices of spin-coated films showed higher rectification factors when compared to the LS ones, except for the P3BT in which both cases showed no rectifying signature.

### 5.3. Electrochemical measurements and energy diagrams

Besides the Schottky barrier, the energy diagram also plays an important role on the charge transport in direct and reverse polarization, due to the work functions of the ITO electrodes ( $4.8$  eV)<sup>158</sup> and Al ( $4.1$  eV)<sup>20</sup>, which promote different barriers for charge injection in the material<sup>159</sup>. Figure 42 shows the energy diagram for a hypothetical ITO/polymer/Al device, highlighting the work functions of ITO and Al, the HOMO and LUMO levels, and  $E_{\text{gap}}$ . By means of CV measurements, it was possible to determine the energy diagrams of the organic devices, since HOMO and LUMO are directly related to their ionization potential and electronic affinity, and thus allow an estimate of the interfacial barrier energy<sup>160</sup>.

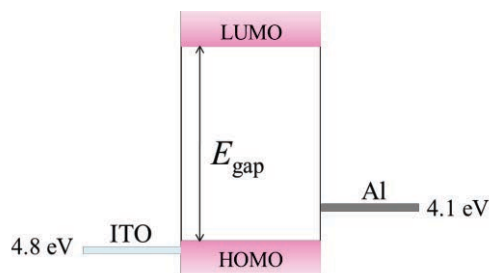


**Figure 42:** Energy diagram for a hypothetical ITO/polymer/Al device.

Figure 43 (a) and (b) shows the CV results obtained for the P3AT films deposited by spin-coating and LS technique, respectively, where two oxidation and reduction peaks were observed for all P3AT derivatives. The shape of the voltammogram of P3AT derivatives depends on several features, including the polymer molecular weight<sup>123</sup> and the monomer side chain length<sup>140</sup>. Before the first oxidation peak it was possible to estimate the oxidation potential onset,  $E'_{\text{ox}}$ ,<sup>161,162</sup> as observed in the Figure 43 (c) for the P3DT spin-coated film.

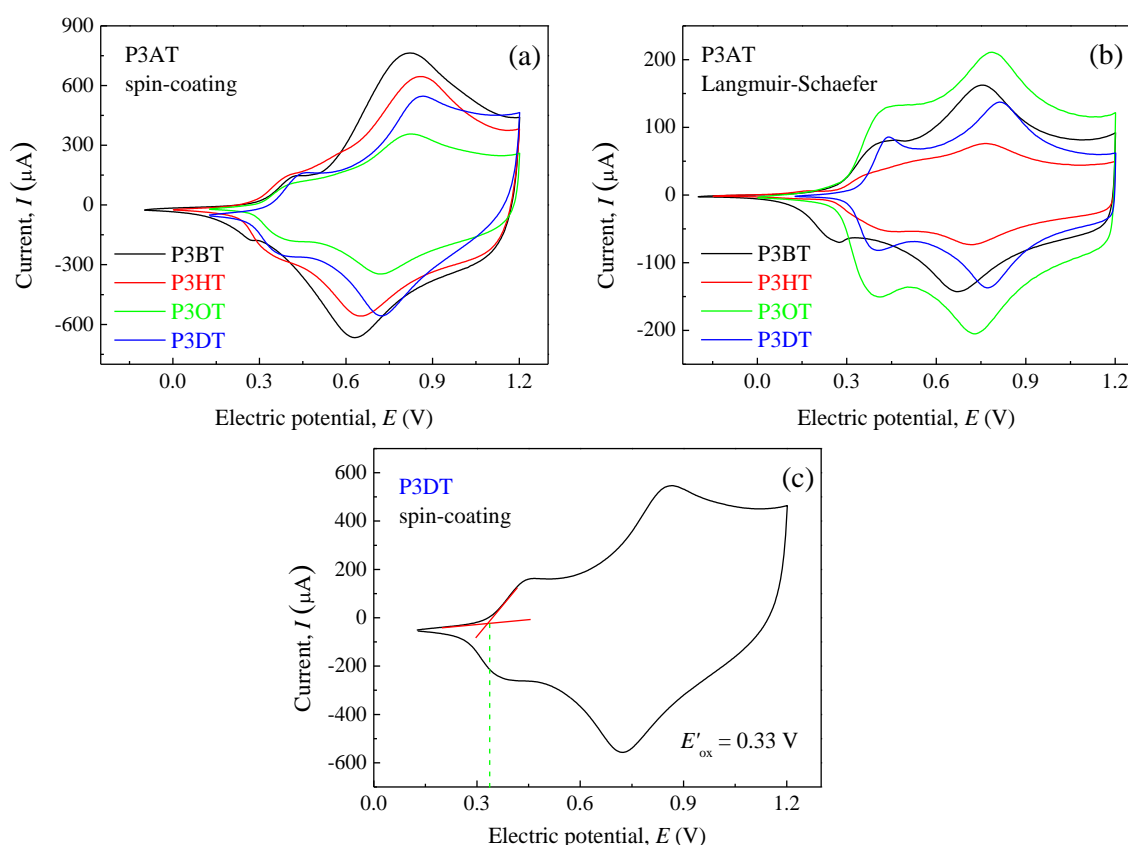


**Figure 43:** CV data for the P3AT films deposited by (a) spin-coating and (b) LS technique. (c) CV results for the P3OT spin-coated film showing the oxidation potentials onset ( $E'_{\text{ox}}$ ) estimated from the intersection of the two tangents drawn at the rising oxidation current and background current in the cyclic voltammograms. Image from<sup>157</sup>.

Since the measurements were carried out in solution and not under vacuum, the values must be corrected for each type of reference electrode and solution that was employed. The energy for the HOMO level can be calculated by the relation  $E_{\text{HOMO}} = e E'_{\text{ox}} + 4.43$ , where  $e$  is the electron charge and 4.43 eV is the correction for the Ag/ACN with TBAP 0.1 mol.L<sup>-1</sup> electrode<sup>163,164</sup>. The HOMO values were calculated to be around 4.73, 4.71, 4.73 and 4.76 eV for the spin-coated films and around 4.68, 4.70, 4.73 and 4.77 eV for the ones obtained by the LS technique for P3BT, P3HT, P3OT and P3DT respectively. These HOMO values are similar to the ones found in literature for thin films of regioregular P3HT<sup>165</sup>.

It was not possible to estimate the electronic affinity in the region of the anodic potential of the voltammograms (related to the LUMO of the considered material) due to the difficulty to accurately determine the potentials' onset for the second reduction peak. Instead, UV-visible optical absorption measurements were employed to determine the optical gap, which is usually close to the electronic gap, as shown by H. Eckhardt *et al.* for the poly(phenylene vinylene)<sup>166</sup>. The wavelength related to the optical gap is estimated by the intersection between the red lines in Figure 44, allowing for the calculation of the gap energy  $E_{\text{gap}}$ <sup>163</sup>:

$$E_{\text{gap}} = \frac{hc}{\lambda} = \frac{4.135 \times 10^{-15} \cdot 3 \times 10^8}{\lambda} = \frac{1240}{\lambda} \text{ eV} \quad (8)$$

where  $h$  represents the Planck's constant in eV.s and  $c$  the speed of light in vacuum, in m/s.

The calculated  $E_{\text{gap}}$  were 1.95, 1.93, 1.92 and 1.92 eV for the spin-coated films, and 1.89, 1.92, 1.91 and 1.90 eV for the LS films of P3BT, P3HT, P3OT and P3DT respectively. These values are similar to the ones obtained by S. Alkan *et al.* for thin films of polythiophene derivatives grown by electrochemical polymerization<sup>167</sup>. Despite the small differences, the  $E_{\text{gap}}$  are smaller for the LS than for the spin-coated films. Low band gaps can be related to higher conjugation length<sup>168</sup> induced by the possible organization at the molecular level of the films provided by Langmuir deposition techniques<sup>169</sup>.

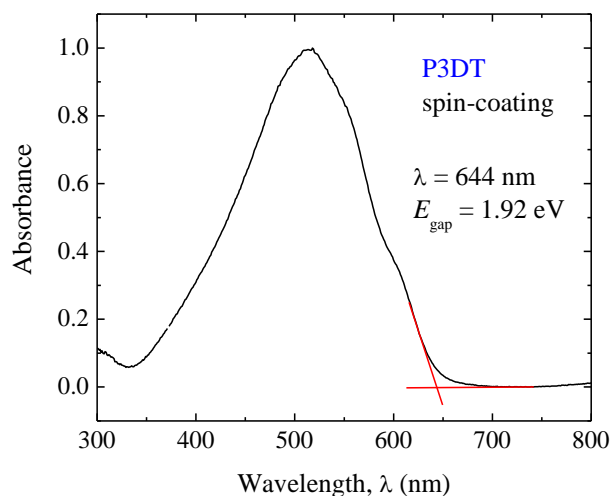


**Figure 44:** UV-visible absorption spectra for the P3DT spin-coated film where the red lines intersection show the wavelength used to calculate the  $E_{\text{gap}}$  for the thin film.

From the values of  $E_{\text{HOMO}}$  and  $E_{\text{gap}}$  it is possible to calculate the energy level for the LUMO,  $E_{\text{LUMO}}$ , through the relation  $E_{\text{LUMO}} = E_{\text{HOMO}} - E_{\text{gap}}$ . The procedure followed to estimate the energy diagram was the same as the adopted by F.N. Crespilho *et al.*<sup>170</sup>. The application of this method to obtain energy diagrams is possible once the charge transfer process is assumed to be reversible, *i.e.* the position of voltammetric signals is determined by thermodynamics of the process (not kinetic phenomena). The results that allowed estimating the energy diagram for the spin-coated and LS films of the polythiophene derivatives are shown in Table 2.

**Table 2:** Results obtained by CV and UV-visible optical absorption measurements for the P3AT films deposited by spin-coating and LS technique.

	<b>Deposition technique</b>	$E'_{\text{ox}}$ (V)	$E_{\text{HOMO}}$ (eV)	$E_{\text{gap}}$ (eV)	$E_{\text{LUMO}}$ (eV)
P3BT	spin-coating	0.30	4.73	1.95	2.78
P3BT	LS	0.25	4.68	1.89	2.79
P3HT	spin-coating	0.28	4.71	1.93	2.73
P3HT	LS	0.27	4.70	1.92	2.78
P3OT	spin-coating	0.30	4.73	1.92	2.81
P3OT	LS	0.30	4.73	1.91	2.82
P3DT	spin-coating	0.33	4.76	1.92	2.84
P3DT	LS	0.34	4.77	1.90	2.87



From the Figure 41, the most pronounced electric current is for the ITO/P3HT/Al device that showed 17 and 40  $\mu\text{A}$  at 20 MV/m for spin-coated and LS films, respectively. The increase of current for the LS film when compared to the spin-coated one can be related with the increase of  $E_{\text{LUMO}}$ , justifying the increase of current due to a small barrier for the charge injection in the LS film device. On the other hand, for the P3DT there is also an increase of  $E_{\text{LUMO}}$  for the LS film, and conversely, a decrease of current from 7 to 4  $\mu\text{A}$  when compared to the spin-coated film at 20 MV/m for the ITO/P3DT/Al devices in the  $I$  vs.  $F$  plots. Therefore, the  $I$  vs.  $F$  plots cannot be evaluated only by the interface between polymeric material and electrodes (energy diagram), but also by the transport properties in the bulk, which must be taken into account<sup>171,172</sup>.

During the CV measurements, a color change has been noticed for all the P3AT spin-coated and LS films. For the P3BT film, the color changed from orange-red to blue when oxidized, as seen in Figure 45 for the spin-coated film. The thin films of P3HT, P3OT and P3DT have a dark pink to purple color when in neutral state, and a bluish color during the oxidation process, which was similar for all the compounds. A similar result was obtained by P.R. Somani and S. Radhakrishnan for different polythiophene derivatives, observing colors between red, orange and brown in the neutral form and dark blue or greenish when oxidized depending on the monomer of the polymer structure<sup>173</sup>.

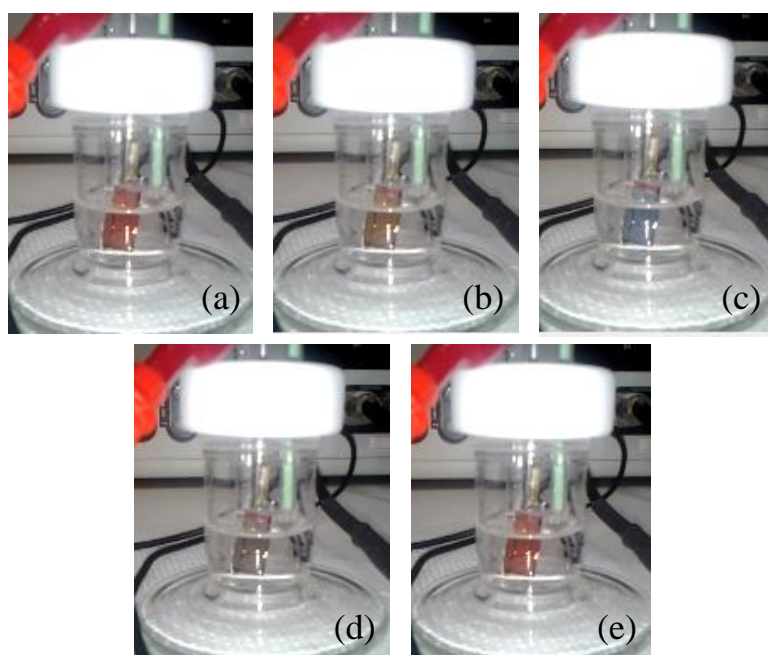


**Figure 45:** Images from the color changing of P3BT spin-coated film during the CV measurements around (a) 0.4 V, (b) 0.6 V and (c) 0.8 V for the oxidation process and (d) 0.6 V and (e) 0.4 V for the reduction one. Image from<sup>157</sup>.

Electrochromism has been reported since 1981 for conducting polymers, when A.F. Diaz *et al.* have noticed a color change in films of polypyrrole derivatives from yellow to black when oxidized<sup>174</sup>. Since 1983, several papers have been published about the occurrence of this phenomenon in films of polythiophene derivatives, and also the observation of a single oxidation peak<sup>175</sup>. According to R.J. Mortimer, the conducting polymers in their oxidized form are “doped” with anions, introducing polarons which are the majority charge carriers in this kind of material. The reduction, however, removes the electronic conjugation, in such a way the polymer returns to its neutral form (undoped)<sup>176</sup>. The electrochromism mechanism is similar for the conducting polymers, but a particular feature observed for the polythiophene derivatives is the formation of bipolarons instead of polarons during the doping process<sup>177</sup>, as confirmed by J. Chen *et al.* in 1986<sup>178</sup>.

The electrochromism observed during the CV measurements on the spin-coated and LS films of P3BT, P3HT, P3OT and P3DT was analyzed by means of UV-visible optical absorption spectroscopy in steps of 0.2 V from 0 to 1.2 V. These results for the LS films are shown in Figure 46, and for the spin-coated films similar results were observed (data not shown). It is possible to observe a decrease of the intensity of the band around 500 nm as the oxidation is driven by the applied voltage, and its subsequent increase during the reduction process (inset). It was also noticed the appearance of a possible wide absorption band at higher wavelengths during the oxidation process, probably related to the color change to blue. The technique of obtaining absorption spectra during the CV is very common and the results found are in good agreement with the ones found in the literature for the polythiophene derivatives<sup>167,177</sup>. K. Hyodo carried out similar investigation with polyaniline and poly-N-methylpyrrole films and has also noticed a reduction of the bandwidth of the absorption band and appearance of a new one at higher wavelengths as the oxidation carries out<sup>179</sup>.

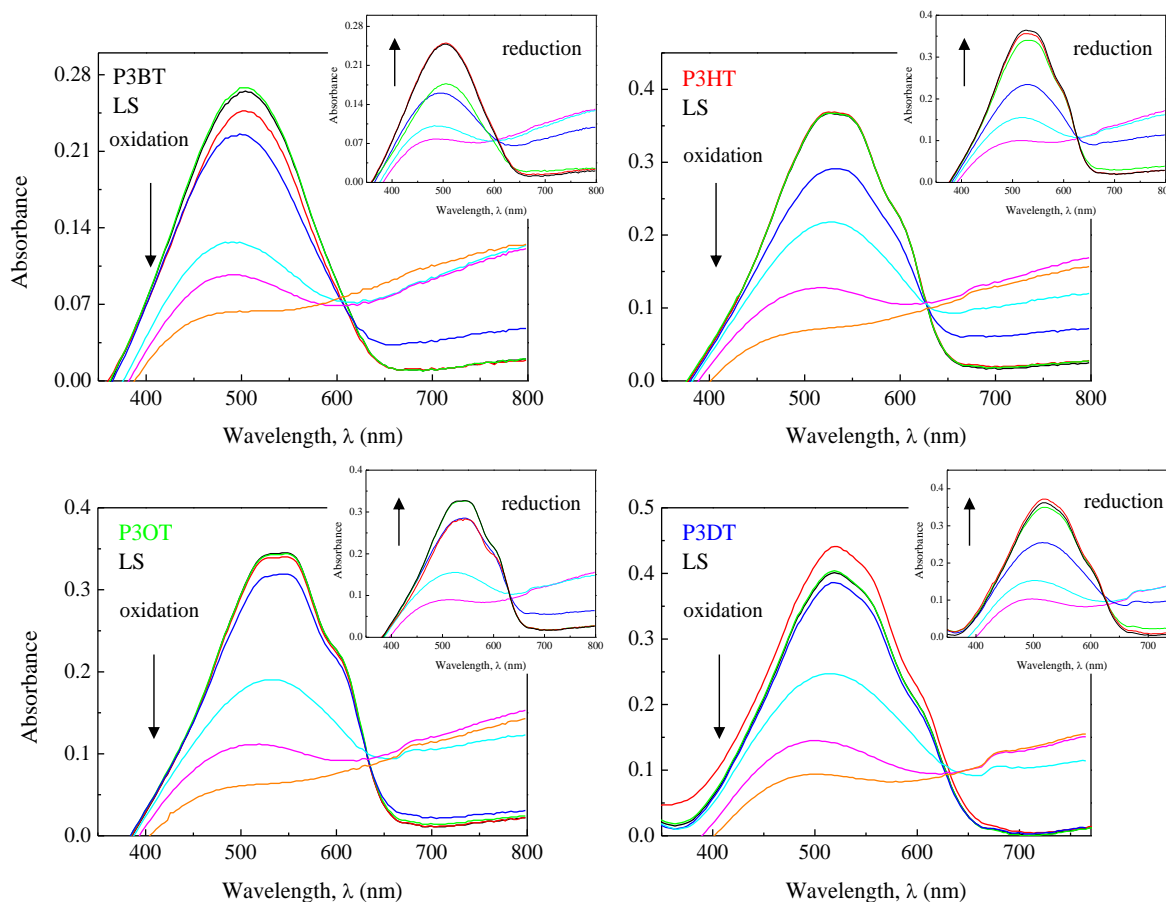


**Figure 46:** Absorption spectra in the UV-visible range for the LS films of P3BT, P3HT, P3OT and P3DT obtained in different voltages during the oxidation and reduction (inset) processes. In the graphs, the black, red, green, dark blue, blue, pink and orange lines are related with the electric potential 0, 0.2, 0.4, 0.6, 0.8, 1.0 and 1.2 V, respectively. Image from <sup>157</sup>.

#### 5.4. Impedance analysis in ITO/P3AT/Al devices

The  $Z'$  vs.  $f$  plots obtained for the ITO/P3AT/Al devices in which the P3AT films were deposited by spin-coating (ITO/P3AT(spine-coating)/Al) and LS (ITO/P3AT(LS)/Al) techniques are shown in Figure 47. The experimental results are represented by the open circles while the solid lines are the theoretical fitting, discussed later in this section. Through these results one can see some similarities between the spectra of the devices. For the  $Z'$  vs.  $f$  data there is a behavior where  $Z'$  tends to reach constant values (plateaus) at low and high frequencies. This is a clear result for some plots as for the P3HT spin-coated film at low frequencies, but it is not evident for others, and this reason that justifies the use of theoretical fitting. The plateaus shift at low frequencies according to the DC bias applied. This result is possible related to the reduction of the potential barrier in the Al/P3AT interface while the DC bias applied increases <sup>23</sup>.

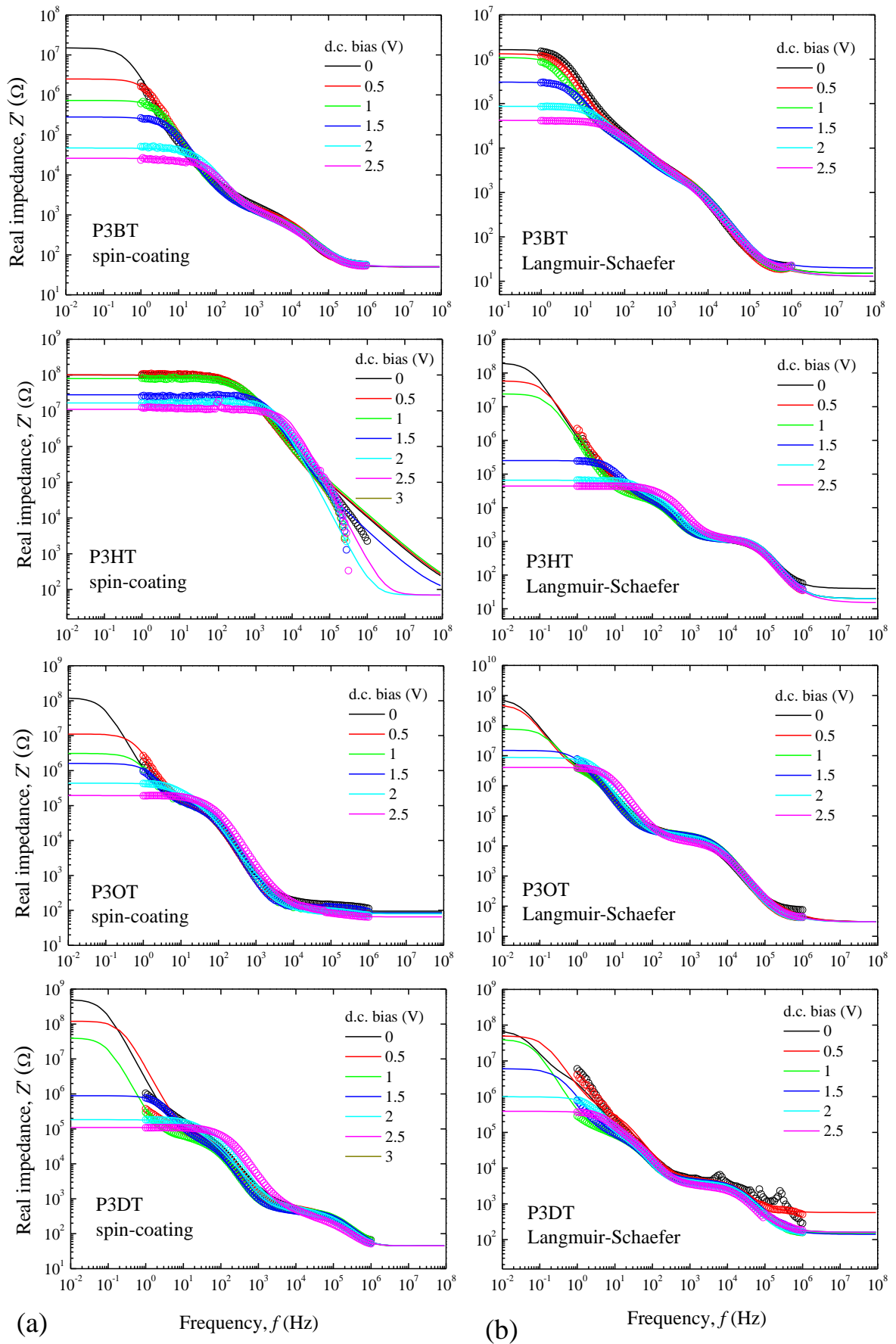


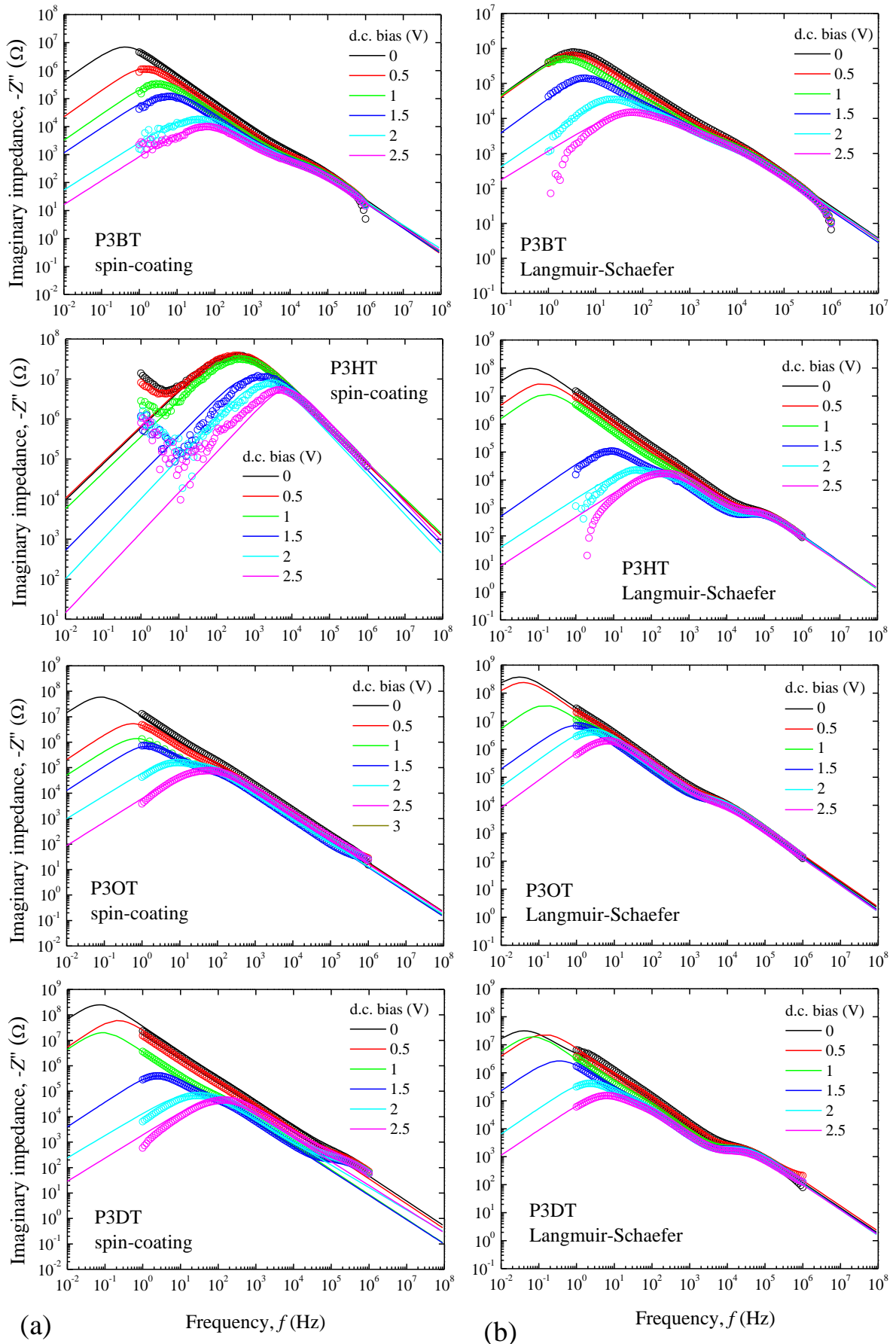
**Figure 47:**  $Z'$  vs.  $f$  plots for the ITO/P3AT/Al devices for (a) spin-coated and (b) LS films.

The theoretical models were proposed using equivalent electrical circuits of associated resistors and capacitors. The resistors are used to represent the possible resistance of the materials or the interface resistance between two different materials. The capacitors, on the other hand, are used to represent the charge accumulation at the interfaces, thus defining the characteristic relaxation times of the studied structures. The theoretical model applied was the equivalent circuit (Equation 9) <sup>23</sup>, in which the  $\alpha$  parameter analytically simulates the distribution of dielectric relaxation time  $\tau$ , where  $0 \leq \alpha \leq 1$ .

$$Z^* = R + \frac{R_1}{1 + (\omega R_1 C_1)^{1 - \alpha_1}} + \frac{R_2}{1 + (\omega R_2 C_2)^{1 - \alpha_2}} + \left( \frac{R_1}{1 + (\omega R_1 C_1)^{1 - \alpha_1}} + \frac{R_2}{1 + (\omega R_2 C_2)^{1 - \alpha_2}} \right) j \quad (9)$$

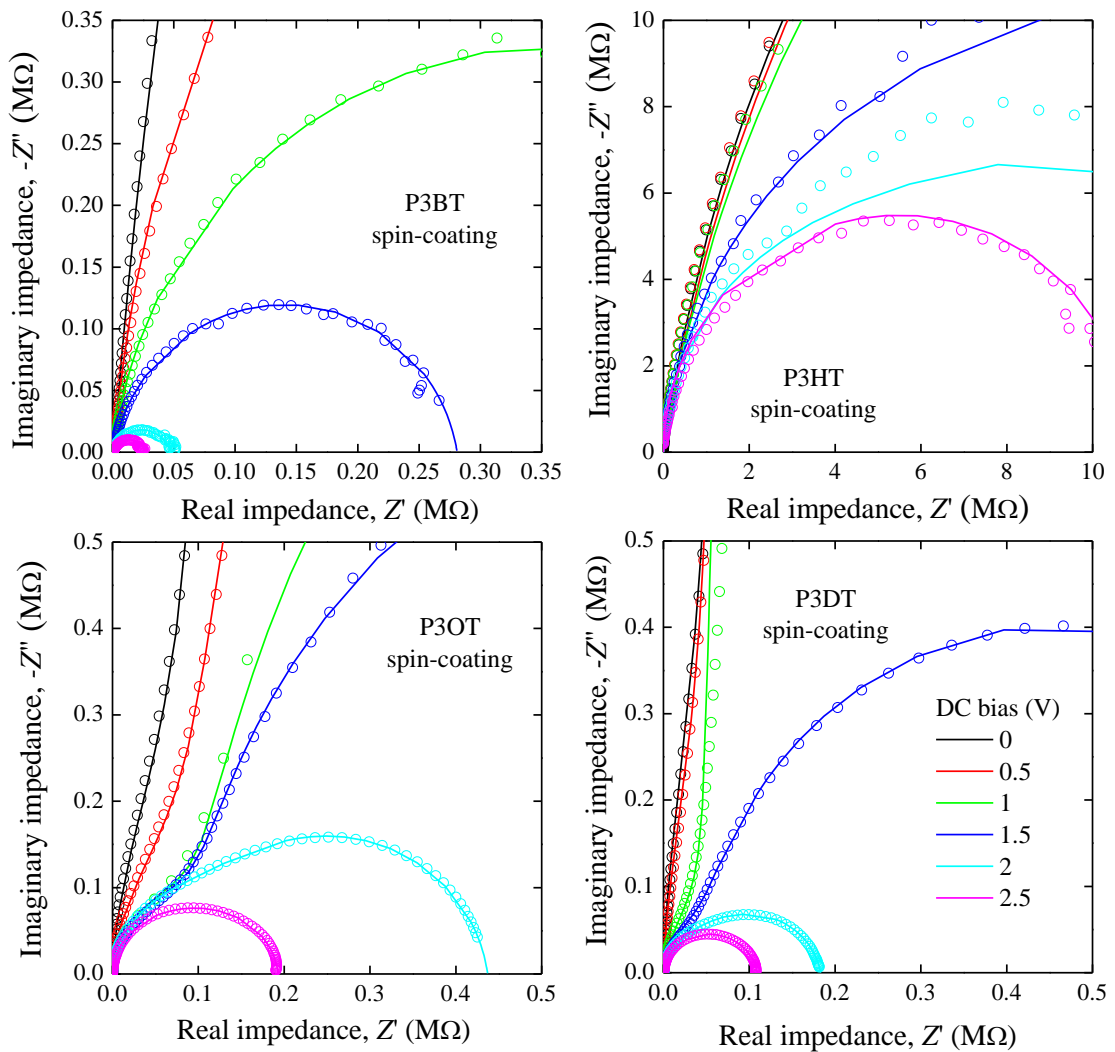
The model provides a symmetric distribution of relaxation times and enables the development of more complex models. Applying the Mathcad software (version 14.0), the analysis of the experimental data and theoretical modeling of the electrical measurements were performed.

Figure 48 shows the  $Z'$  vs.  $f$  plots obtained for the ITO/P3AT/Al devices in which the P3AT films were deposited by spin-coating (ITO/P3AT(spin-coating)/Al) and LS (ITO/P3AT(LS)/Al) techniques. As for the  $Z'$  vs.  $f$  plots, in Figure 48 the experimental results are represented by the open circles while the solid lines are the theoretical fitting. In the  $-Z''$  vs.  $f$  spectra, for the spin-coated and LS films of P3BT is observed one well-defined relaxation peak which, in both films, the peak shifts to lower frequencies with the increase of the DC bias applied. For the P3HT spin-coated film is observed only one relaxation peak which shifts in middle frequencies, while the P3HT LS film presents two relaxation peaks, wherein one peak shifts from low to medium frequencies (around 10 to  $10^2$  Hz) and the other less defined remains constant at high frequencies. For the spin-coated and LS films of P3OT is observed only one well-defined relaxation peak formed, similar to the P3BT case. However, it is possible to notice the formation of one shoulder peak around  $10^4$  Hz for the P3OT LS film. For the spin-coated and LS films of P3DT is observed one well-defined relaxation peak at low frequencies and one shoulder peak at higher frequencies. The shoulder peaks improve their definition according to the applied DC bias.



**Figure 48:**  $-Z''$  vs.  $f$  plots for the ITO/P3AT/Al devices for (a) spin-coated and (b) LS films.

Some plateaus and relaxation peaks only can be observed due to the extrapolation of the frequency used in the theoretical fittings. The Argand diagrams for the devices in which the derivatives of P3AT have been deposited by spin-coating and Langmuir-Schaefer are shown in Figure 49 and Figure 50, respectively. In the Argand diagram for the ITO/P3AT/Al devices it is possible to observe only one semicircle possibly due to the overlapping of two or more semicircles. In all diagrams,  $Z^*$  tends to smaller semicircles with increasing DC bias voltage, wherein the diameter of the semicircle is related to the total resistance of the device. In theoretical fittings, each circle shall be related to an RC circuit in parallel.



**Figure 49:** Argand diagrams for the ITO/P3AT(spine-coating)/Al devices.

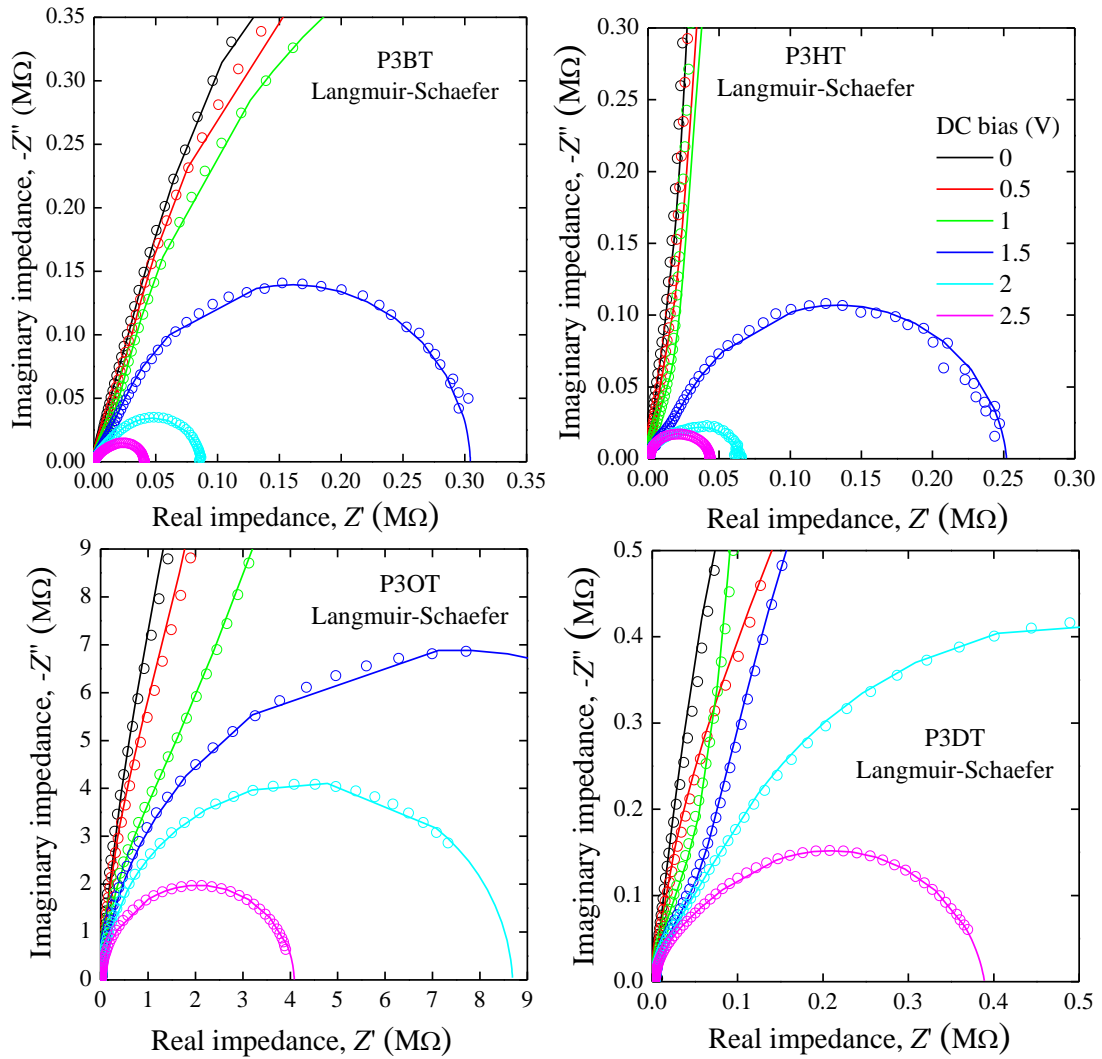


**Figure 50:** Argand diagrams for the ITO/P3AT(Langmuir-Schaefer)/Al devices.

The experimental data were analyzed using the electrical circuits shown in Figure 51. For the devices of P3AT spin-coated films were used the equivalent circuit with two parallel RC (Figure 51 (a)), except for the P3DT, and for the P3AT LS films were used the one with three parallel RC (Figure 51 (b)). Due to the higher roughness, the P3AT films deposited by LS have more contact surface with the aluminum electrode, which probably cause more interfacial effects. This is a possible explanation for the additional parallel RC circuit in theoretical fitting for the ITO/P3AT(LS)/Al devices.



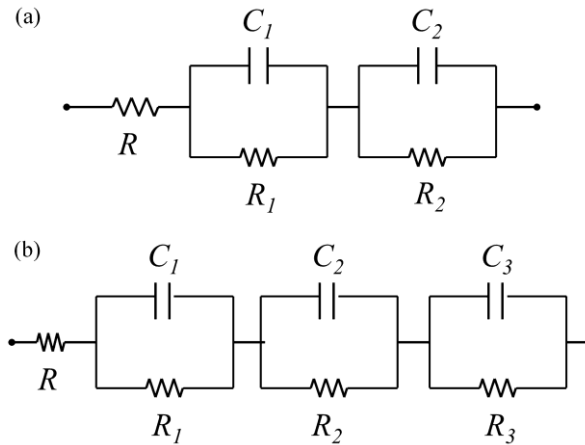


**Figure 51:** Equivalent electrical circuits used in the theoretical fitting for the ITO/P3AT/Al devices.

Through theoretical fittings of Argand diagrams, for most devices in which the P3AT derivatives were deposited by spin-coating technique it is possible to evaluate the superposition of two semicircles. Only for the ITO/P3DT(spun-coating)/Al device the theoretical fittings showed the superposition of three semicircles. As for the ITO/P3AT(spun-coating)/Al devices, the ITO/P3AT(Langmuir-Schaefer)/Al devices also exhibited only one semicircle, but in this case due to the superposition of three semicircles. The Table 3 shows the parameters obtained by the fittings performed in the experimental curves shown in impedance spectra at DC bias 0 V.

**Table 3:** Parameters obtained through the theoretical fittings of components  $Z'$  and  $Z''$  by Equation 9 for the ITO/P3AT(spun-coating)/Al and ITO/P3AT(LS)/Al devices.

Deposition technique	$R_1$ ( $\Omega$ )	$C_1$ (F)	$R_2$ ( $\Omega$ )	$C_2$ (F)	$R_3$ ( $\Omega$ )	$C_3$ (F)	$R$ ( $\Omega$ )
P3BT spin-coating	$1 \times 10^3$	$1.2 \times 10^{-7}$	$1.5 \times 10^7$	$1.6 \times 10^{-7}$	-	-	50
P3BT LS	$2.6 \times 10^4$	$3.6 \times 10^{-7}$	$2.1 \times 10^3$	$1.1 \times 10^{-7}$	$1.6 \times 10^6$	$1.6 \times 10^{-7}$	15
P3HT spin-coating	$4 \times 10^7$	$3.6 \times 10^{-11}$	$6.1 \times 10^7$	$8.6 \times 10^{-11}$	-	-	70
P3HT LS	$1.05 \times 10^3$	$1.3 \times 10^{-8}$	$1.9 \times 10^4$	$3.6 \times 10^{-7}$	$2 \times 10^8$	$8.2 \times 10^{-8}$	40
P3OT spin-coating	$1 \times 10^5$	$2.2 \times 10^{-7}$	$1.2 \times 10^8$	$1 \times 10^{-7}$	-	-	95
P3OT LS	$1.6 \times 10^4$	$1.6 \times 10^{-8}$	$2.5 \times 10^6$	$1.8 \times 10^{-7}$	$8 \times 10^8$	$4.1 \times 10^{-8}$	30
P3DT spin-coating	$7 \times 10^4$	$1.4 \times 10^{-7}$	$4 \times 10^2$	$1.6 \times 10^{-8}$	$5 \times 10^8$	$2.8 \times 10^{-8}$	45
P3DT LS	$3 \times 10^3$	$1.4 \times 10^{-8}$	$3 \times 10^6$	$2.8 \times 10^{-7}$	$7 \times 10^7$	$3.5 \times 10^{-7}$	160

Through the equivalent circuit obtained, from the analysis of experimental and theoretical spectra and the results of Table 3, for the ITO/P3AT(spun-coating)/Al devices it can be identified: i) one parallel circuit  $R_1C_1$  ( $\sim 10^4$  Hz), wherein  $R_1$  and  $C_1$  are the resistance and capacitance of the bulk of the polymer (P3AT), ii) one parallel circuit  $R_2C_2$  (in low frequency), wherein  $R_2$  and  $C_2$  represent the P3AT(spun-coating)/Al interface and iii) one resistance  $R$  represents the resistance of the P3AT(spun-coating)/ITO interface (ohmic contact). The ITO/P3DT(spun-coating)/Al device showed one additional RC circuit, circuit  $R_3C_3$ , respectively. For the ITO/P3AT(LS)/Al devices can be identified: i) one parallel circuit  $R_1C_1$  ( $\sim 10^4$  Hz), wherein  $R_1$  and  $C_1$  are the resistance and capacitance of the bulk of the polymer (P3AT), ii) two parallel circuits (both in low frequency),  $R_2C_2$  and  $R_3C_3$ , wherein  $R_2$ ,  $R_3$ ,  $C_2$  and  $C_3$  represent the P3AT(LS)/Al interface and iii) one resistance  $R$  represents the resistance of P3AT(LS)/ITO interface (ohmic contact).

Studies using the impedance technique performed by Olivati *et al.* in polymer light emitting devices (PLEDs) fabricated from poly(2-methoxy-5-hexyloxy)-p-phenylenevinylene (OC<sub>1</sub>OC<sub>6</sub>-PPV) thin films by LB technique and the type structure ITO/OC<sub>1</sub>OC<sub>6</sub>-PPV(LB)/Al, reported that the spectrum of  $Z'$  vs.  $f$  presented two plateaus<sup>23</sup>. The measurements were fitted by an equivalent circuit composed of two parallel RC circuits with a series resistance, and through the values obtained by the theoretical fittings, it was identified that an RC circuit represents the resistance and capacitance of the layer OC<sub>1</sub>OC<sub>6</sub>-PPV(LB) and the other circuit represents the OC<sub>1</sub>OC<sub>6</sub>-PPV(LB)/Al interface, the series resistance represents ITO/OC<sub>1</sub>OC<sub>6</sub>-PPV(LB) interface.

To realize the theoretical fittings from the equivalent electrical circuits in impedance measurements for a device like ITO/doped organic layer/Ag, Chen *et al.* used an equivalent electrical circuit consisting of two RC circuits in parallel and one series resistance<sup>180</sup>. The Argand diagrams showed two semicircles and the spectra of  $Z'$  vs.  $f$  showed a tendency to form two plateaus. The semicircles and plateaus were related to RC circuits, where one circuit represents the resistance and capacitance of the doped organic layer/Ag interface and the other represents the resistance and capacitance of the doped organic layer, the series resistance was correlated with ITO/organic layer doped interface.

Mirsky *et al.* through impedance spectroscopy, reported information regarding the resistance of the polymer and metal/polymer interface in measurements performed in a thin film of polypyrrole deposited gold electrodes<sup>181</sup>. The spectrum of  $-Z''$  vs.  $Z'$  was fitted by an equivalent circuit having a series resistance connected to three RC circuits in parallel. One RC circuit represents the resistance and the capacitance of the electrode/polymer interface and the

other two RC circuits represent the capacitance and the resistance of the bulk of conductive polymer.

In Table 4 the electrical conductivities obtained from the Equation 6 to the devices of P3AT spin-coated and LS films are shown. In general, the LS films showed higher electrical conductivity compared to the spin-coated films. The LS film of P3HT showed higher electrical conductivity (order of  $10^{-5}$  S/m) compared to all the other derivatives. A factor related to the highest conductivity is the mobility of charge carriers, since the P3HT has higher regioregularity than other ones. Due to the longer connected chains, charge carriers and excitons can move along these chains also enable more jumps to the neighboring chains

182,183

**Table 4:** Electrical conductivity values for thins films of P3AT derivatives deposited by spin-coating and LS.

Deposition	Polymer	Conductivity (S/m)
spin-coating	P3BT	$8.4 \times 10^{-6}$
LS	P3BT	$2.3 \times 10^{-7}$
spin-coating	P3HT	$2.7 \times 10^{-10}$
LS	P3HT	$2.5 \times 10^{-5}$
spin-coating	P3OT	$8 \times 10^{-8}$
LS	P3OT	$1.2 \times 10^{-6}$
spin-coating	P3DT	$1.6 \times 10^{-7}$
LS	P3DT	$6.1 \times 10^{-6}$

Unlike other P3AT derivatives, the P3BT thin film deposited by spin-coating showed higher electrical conductivity compared to the film deposited by LS. The films deposited by the LS technique showed higher electrical conductivity, probably due to the organization at the molecular level that can be provided by Langmuir techniques. However, the P3BT present a less efficient adhesion onto ITO substrate when compared to the other P3AT derivatives. Thus it is possible that the deposition issues had influenced in the layers packaging, thus hampering the mobility of charge carriers and decreasing the electrical conductivity of the LS film for the P3BT derivative.

## CHAPTER 6: Low-bandgap polymers

### 6.1. Langmuir and Langmuir-Blodgett films of low-bandgap polymers

Figure 52 shows the  $\pi$ -A isotherms of neat and SA mixed Langmuir films of PCPDTBT and PDTSBT. For the neat polymers PCPDTBT and PDTSBT, the mean molecular areas per monomer calculated from the condensed phase (around 30 mN/m) were 21.1 and 15.7  $\text{\AA}^2$ , respectively. From the  $\pi$ -A isotherm for the SA (data not shown), the mean molecular area is 19  $\text{\AA}^2$ , which is in good agreement with the literature<sup>84</sup>. The  $\pi$ -A isotherms for the SA:PCPDTBT showed mean molecular areas per monomer of 27.2, 33.5, 28.9  $\text{\AA}^2$  for 2:1, 4:1 and 8:1, respectively. For the SA:PDTSBT Langmuir films a change was observed in the slope of the  $\pi$ -A isotherms around 27 mN/m for the 2:1 and 4:1 and around 24 mN/m for the 8:1 mixture. Less significant slope changes also occurred around 25 mN/m in the  $\pi$ -A isotherms for the SA:PCPDTBT mixtures. Below the slope changes, the mean molecular areas per monomer are 21.7, 28.2, 26.6 for 2:1, 4:1 and 8:1 SA:PDTSBT mixtures, respectively. Still for the SA:PDTSBT, above 30 mN/m the mean molecular areas per monomer are 21.3, 23.8 and 22.9  $\text{\AA}^2$  for 2:1, 4:1 and 8:1, respectively. Although the differences in the mean molecular areas due to the slope changes in the  $\pi$ -A isotherms for the SA:PDTSBT mixtures, there is a trend in the data for both low-bandgap polymers in SA mixtures. The mean molecular area increases with stearic acid from the 2:1 to 4:1 SA:polymer mixtures, while the area decreases from the 4:1 to 8:1 mixtures.

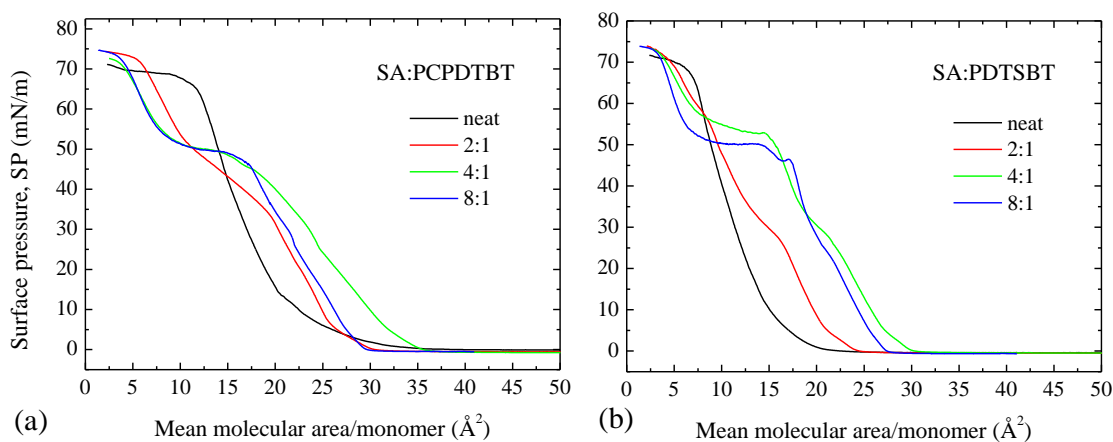


**Figure 52:**  $\pi$ -A isotherms for (a) PCPDTBT and (b) PDTSBT of neat and SA:polymer mixtures of 2:1, 4:1 and 8:1 (mmol).

For mixed films of two ideal compounds named A and B, the  $\pi$ -A isotherm should exhibit i) one collapse surface pressure, if A and B are completely miscible or ii) two collapses in different surface pressures related to the A and B collapses in neat films, if they do not feature miscibility<sup>184</sup>. For the  $\pi$ -A isotherms of 4:1 and 8:1 mixtures two collapses are evident for the two low-bandgap polymers. From this result, one can suppose a mixture of two immiscible materials; however the theory fits perfectly ideal compounds. The lower pressure collapses (around 50 mN/m) feature the SA collapse, as previously shown by M. Rikukawa *et al.*<sup>128</sup>. Nevertheless, the collapse surface pressure for the mixed Langmuir films (around 72 mN/m) is at higher values than the neat polymers (around 66 and 68 mN/m for the PCPDTBT and PDTSTBT, respectively). Therefore, the two low-bandgap polymers and SA are not completely immiscible, but they exhibit a lower miscibility feature. The two collapses in Figure 52 are more evident for the mixtures with higher SA concentrations (4:1 and 8:1 mixtures) while for the 2:1 mixture it is less expressive, which could be interpreted just as a slope change in the  $\pi$ -A isotherms.

After evaluating the  $\pi$ -A isotherms, attempts to LB deposition of the Langmuir films were performed. For neat PCPDTBT and PDTSTBT, it was not possible to grow multilayer LB films. Polythiophene derivatives often do not form true monolayers in the Langmuir trough<sup>30,31</sup> which makes it extremely difficult to transfer the polymer into multilayer structures by LB technique<sup>32</sup>. However, the polymer mixture with stearic acid improved the LB deposition of the two low-bandgap polymers. The deposition surface pressure (SP), the number of deposited multilayers and the transfer ratio (TR) for the LB technique are presented in Table 5. In spite of the LB deposition succeeded for all the polymer:SA rates, the 2:1 concentration for the PDTSTBT built a non-homogeneous film, therefore it was not possible to perform its electrical characterization.

**Table 5:** Deposition parameters for the LB films of PCPDTBT and PDTSTBT.

	PCPDTBT			PDTSTBT		
SA:polymer (mmol)	2:1	4:1	8:1	2:1	4:1	8:1
SP (mN/m)	30	30	30	40	40	30
multilayers	35	61	61	35	71	71
initial TR	1	1	1	1	1	1
final TR	0.8	0.7	0.9	0.8	1	1

## 6.2. Electrical characterization of low-bandgap polymers

The  $I$  vs.  $V$  plots for the LB mixed films of the low-bandgap polymers (SA:PCPDTBT and SA:PDTSBT) deposited onto IDE are shown in Figure 53. In addition, the inset in Figure 53 shows pictures of these devices. The linear behavior of  $I$  vs.  $V$  plots allows to obtain the electrical resistance  $R$  of the polymer mixtures in this electrode configuration. The electrical conductivity  $\sigma_{DC}$  is calculated using the cell constant, which takes into account the digit height, spacing, number and length<sup>108</sup>. For the IDE described in this paper, the cell constant is  $5.1 \text{ m}^{-1}$ <sup>80</sup>. The obtained  $R$  and the calculated  $\sigma_{DC}$  for the LB films of the two low-bandgap polymers in IDE devices are presented in Table 6.

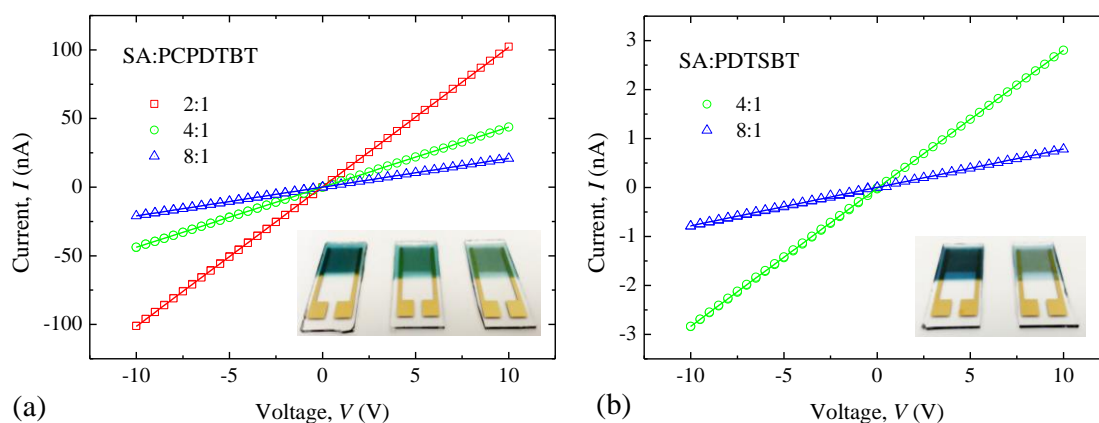


**Figure 53:**  $I$  vs.  $V$  electrical measurements for the LB mixed films of the low-bandgap polymers (a) PCPDTBT and (b) PDTSBT.

**Table 6:** Electrical properties for the LB films of low-bandgap polymers in IDE devices.

	PCPDTBT			PDTSBT	
SA:polymer (mmol)	2:1	4:1	8:1	4:1	8:1
$R$ ( $G\Omega$ )	0.1	0.2	0.5	3.5	12.8
$\sigma_{DC}$ (S/m)	$5.2 \times 10^{-8}$	$2.2 \times 10^{-8}$	$1.1 \times 10^{-8}$	$1.4 \times 10^{-9}$	$4.0 \times 10^{-10}$

For both low-bandgap polymers, there is a trend in the data showing the  $\sigma_{dc}$  decrease for higher concentration of SA in the mixture. Despite the SA improved the LB deposition, it is also well defined as an insulator molecule, which can harm the electrical properties of the resulting films<sup>185</sup>. Apart from the SA, the PCPDTBT in IDE devices showed higher  $\sigma_{DC}$  than PDTSBT. This result is possible associated to the  $\pi$ -A isotherms obtained, where the mean

molecular area per monomer in the condensed phase is smaller for the PDTSBT than for the PCPDTBT.

## CHAPTER 7: Electrical measurements in organic heterojunction devices

In this section the main results obtained for the OPV devices will be presented. The results for the P3AT used as donor layers deposited by spin-coating and Langmuir-Schaefer are discussed herein. Some preliminary results as well as the challenges that were faced are shown in the first subsection. The final results are shown in the second subsection and despite the simplicity of the devices, the planar heterojunction OPV devices showed the photovoltaic effect.

### 7.1. Preliminary results in the homemade dark box

The first devices fabricated in this research were built in planar heterojunctions of P3AT and  $C_{60}$ . The P3AT derivatives were deposited by spin-coating and Langmuir-Schaefer and the  $C_{60}$  was deposited by PVD. The final structure of the devices was ITO/P3AT/ $C_{60}$ /Al. The photovoltaic tests were conducted in the homemade dark box using a halogen lamp, as described for the photoconductivity tests for the P3AT films in IDE devices (section 5.1.). The  $J$  vs.  $V$  curves for these OPV devices are shown in Figure 54(a) for the devices in which the P3OT layers were deposited by spin-coating and in Figure 54(b) the P3OT were deposited by Langmuir-Schaefer technique. Since the results for the other P3AT derivatives were similar, they were not presented.

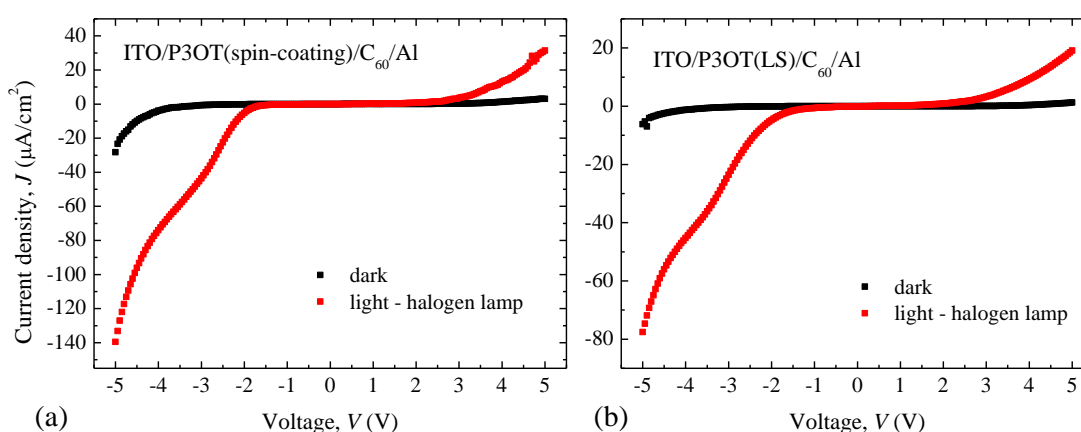


**Figure 54:**  $J$  vs.  $V$  curves for the planar heterojunction devices (ITO/P3AT/ $C_{60}$ /Al) under illumination of a halogen lamp ( $150 \text{ mW/cm}^2$ ). In the devices, the donor layers were deposited by (a) spin-coating and (b) Langmuir-Schaefer techniques.



The results show distinct curves in the dark and under illumination, thus highlighting the photovoltaic potential of these devices. However, the main features of a photovoltaic device ( $J_{SC}$  and  $V_{OC}$ ) were not observed. In other words, carriers are being created in the bulk of the active layer, but not being separated probably due to the lack of a barrier or depletion region<sup>186</sup>. This result can be related to some issues, as the intensity of the light. Some tests using a voltage controller showed the photovoltaic effect, justifying an acquisition of a solar simulator from a project of Prof. Olivati (FAPESP grant). Such equipment is shown in Figure 26.

Most usually, OPV devices are fabricated with an anode buffer layer between the ITO electrode and the donor layer. Several materials can be used as anode buffer layers, including PEDOT:PSS,  $V_2O_5$ ,  $MoO_3$ ,  $WO_3$  and NiO<sup>111</sup>. For the first devices this layer was not used, and it can be one of the explanations of some features observed in the results. In section 7.2. results for OPV devices in which PEDOT:PSS was used as anode buffer layer are presented.

## 7.2. P3AT derivatives and perylene in planar heterojunctions

During the PhD progress some partnerships were established, among them is the one with Prof. Carlos J. L. Constantino. Interesting results for the BuPTCD film from a master student (José D. Fernandes) were highlighted when its electrical conductivity was increased by 2 orders of magnitude ( $10^{-10}$  to  $10^{-8}$  S/m) when illuminated by the halogen lamp (150  $mW/cm^2$ ) in the homemade apparatus shown in Figure 25. These results prompted the construction of new OPV devices using such perylene derivative as electron acceptor layer.

Figure 55 shows the  $J$  vs.  $V$  curves for the P3AT and BuPTCD in planar heterojunction (ITO/PEDOT:PSS/P3AT/BuPTCD/Al) OPV devices in the dark and under illumination of a solar simulator. In Figure 55(a) the results obtained for the devices in which the donor layers were deposited by spin-coating are shown, while in Figure 55(b) the donor materials were deposited by Langmuir-Schaefer technique. In both cases, the BuPTCD was deposited by PVD, as described in Chapter 3. All the devices in this configuration showed the photovoltaic effect. It was not possible to grow the P3BT LS film onto PEDOT:PSS layer, therefore the black curve usually correlated to the P3BT is shown in Figure 55(a), but not in Figure 55(b).

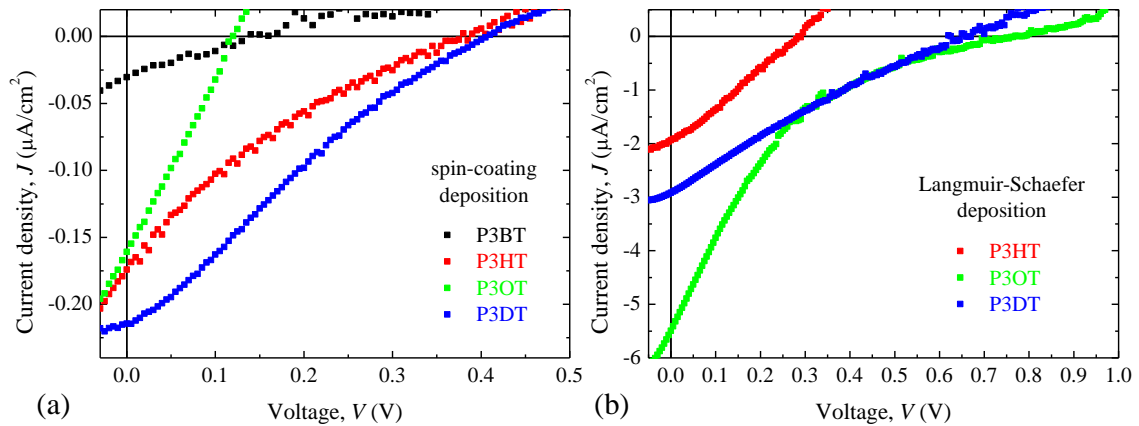


**Figure 55:**  $J$  vs.  $V$  curves for the planar heterojunction devices (ITO/PEDOT:PSS/P3AT/BuPTCD/Al) under illumination of a solar simulator ( $100 \text{ mW/cm}^2$  - AM 1.5). In the devices, the donor layers were deposited by (a) spin-coating and (b) Langmuir-Schaefer techniques.

Table 7 shows the photovoltaic parameters for the OPV devices in planar heterojunctions for the spin-coated and LS donor layers. The OPV devices built with LS films for the donor layers showed higher values of  $J_{SC}$  when compared to the related devices built using spin-coating technique. For the P3OT and P3DT donor layers, an increase in the  $V_{OC}$  when deposited by LS technique is shown, while for the P3HT there is a decrease of this parameter. Additionally, despite the low efficiency, it is possible to notice an increase in the efficiency of at least one order of magnitude for the devices in which the donor layer was deposited by LS. Therefore, the possibly higher degree of nanostructuration of the donor layer indeed positively affects the OPV performance.

**Table 7:** Photovoltaic parameters obtained for the OPV devices of P3AT (spin-coating or Langmuir-Schaefer) and BuPTCD in planar heterojunctions.

	$J_{max}$ ( $\mu\text{A/cm}^2$ )	$V_{max}$ (V)	$J_{SC}$ ( $\mu\text{A/cm}^2$ )	$V_{OC}$ (V)	$FF$	$\eta$ (%)
<b>spin-coating</b>						
P3BT	0.01	0.07	0.03	0.16	0.15	$7.2 \times 10^{-7}$
P3HT	0.07	0.16	0.17	0.39	0.17	$1.1 \times 10^{-5}$
P3OT	0.09	0.06	0.16	0.29	0.12	$5.6 \times 10^{-6}$
P3DT	0.11	0.18	0.21	0.41	0.23	$2.0 \times 10^{-5}$
<b>Langmuir-Schaefer</b>						
P3HT	1.06	0.14	1.94	0.29	0.26	$1.5 \times 10^{-4}$
P3OT	2.25	0.21	5.49	0.78	0.11	$4.7 \times 10^{-4}$
P3DT	1.38	0.30	2.92	0.67	0.21	$4.1 \times 10^{-4}$

It is important to stress that the measurements were conducted in open atmosphere. According to K. Kawano *et al.*, the exposure of organic solar cells to air results in rapid, illumination independent, degradation of the device efficiency<sup>187</sup>. Studies as a function of atmospheric conditions determined that this degradation results from the exposure of the device to natural humidity<sup>187</sup>. Therefore for OPV devices, the measurements are usually conducted under N<sub>2</sub> atmosphere using a glovebox or encapsulating the cells<sup>188,189</sup>. It is important to mention that although the OPV measurements were carried out in non-ideal conditions, the main conclusion of this work was not directly affected.

Since the nanostructuring of the donor layers provided by LS technique did improve the OPV performance of the devices, it would be interesting to apply other common methodologies used to achieve more efficient solar cells as a matter of comparison. A relatively simple, yet effective approach is the addition of a cathode window layer between the acceptor layer and the Al electrode. For this reason, the OPV devices formed by donor layers deposited by spin-coating technique were rebuilt exactly as presented before and also using LiF as cathode window layer.

Figure 56 shows the  $J$  vs.  $V$  curves for the OPV device with P3DT deposited by spin-coating as donor layer (dark blue curve) and also using LiF (light blue curve). This specific device is shown since the P3DT was the derivative which presented the most remarkable improvement upon deposition of LiF. It was observed that some of the performance parameters increased significantly ( $J_{\max} = 0.41 \mu\text{A}$ ,  $V_{\max} = 0.18 \text{ V}$ ,  $J_{\text{SC}} = 0.80 \mu\text{A}$ ,  $V_{\text{OC}} = 0.40 \text{ V}$ ,  $\text{FF} = 0.23$ ,  $\eta = 7.4 \times 10^{-5} \%$ ) for the device with LiF, as compared to the ones without such compound. However, this improvement is not as high as the one obtained for the devices built with LS films for the donor layer (Figure 55(b)). Still in Figure 56, in order to facilitate this comparison discussed above, the orange curve represents the result obtained for the device where the P3DT was deposited by LS technique.

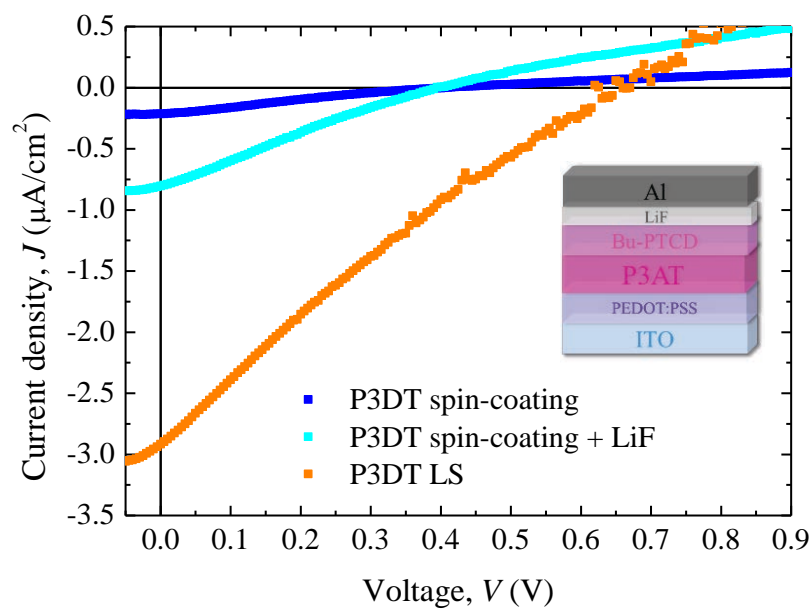


**Figure 56:**  $J$  vs.  $V$  curves measured under illumination of a solar simulator for the OPV devices using P3DT spin-coated film as donor layer with (light blue curve) and without (dark blue curve) LiF used as cathode window layer.  $J$  vs.  $V$  result for the OPV device simply using P3DT LS film (orange curve) as donor layer.

## CHAPTER 8: Conclusions

The distinct molecular organizations on optical, morphological, electrical and electrochemical properties of regioregular P3AT derivatives forming thin films was demonstrated. From the UV-visible absorption data it was observed that polymers deposited by LS show higher order in the thin film form than those deposited by spin-coating technique. The results obtained for the fluorescence measurements justify the  $\pi$ -stack organization of P3AT derivatives, according to the literature. Through AFM measurements it was observed that LS P3AT films show higher roughness compared to films deposited by spin-coating of the same polymer. At first, it was assumed that the roughness could be acquired at the time of LS deposition, but after analyzing results obtained for BAM measurements, it was concluded that the Langmuir films of P3AT derivatives form aggregates in the trough, which are transferred to the solid substrate giving rise to the rough characteristic of the LS films.

Among the P3AT films, those grown by the LS technique onto IDE devices showed higher conductivity (except for P3BT), probably due to the higher roughness of the films and organization at the molecular level provided by Langmuir techniques. The ITO/P3AT/Al devices showed rectifying diode behavior, except for the P3BT derivative. Through cyclic voltammetry and UV-visible absorption measurements it was possible to estimate the energy diagrams for the four P3AT derivatives in the thin films form. Therefore, the electrical features of polymeric devices in diode-like structure cannot be evaluated only by the charge carrier injection, but also the transport properties in the bulk must be taken into account.

For the impedance analysis, the theoretical model used satisfactorily simulates the data obtained for the devices ITO/P3AT/Al. With the analysis of the experimental/theoretical spectra and the values of the parameters used in the equivalent electric circuit, information were obtained and related with electronic transport properties and interfacial effects. For the polymers P3BT, P3HT and P3OT in ITO/P3AT/Al structure, the theoretical fit shows that the ones deposited by spin-coating could be fitted by two parallel RC and the ones deposited by LS should be fitted by three parallel RC. The only exception is the P3DT, which was fitted by three parallel RC regardless the deposition technique used to build the thin film. Among the P3AT films, those grown by the LS technique showed higher electrical conductivity, and the only exception was the P3BT, in accordance with the results obtained for the P3AT films onto IDE devices.

Despite their simplicity, the ITO/PEDOT:PSS/P3AT/BuPTCD/Al devices showed photovoltaic effect. Among these, the devices in which the donor layer (P3AT derivative) was

deposited by LS technique presented higher performance when compared to the ones in which the donor layer was deposited by spin-coating. Therefore, the possibly higher degree of nanostructuration provided by the deposition technique of the donor layer indeed positively affects the OPV performance. A usual approach was applied to the OPV devices with spin-coated donor layers and the increase in the performance was not as high as the one obtained for the devices with LS films, justifying the use of the Langmuir techniques in the OPV area.

The synthesized polymer, PCPDTBT, showed high molecular weight and good thermal stability. The amount synthesized was appropriate to perform deposition tests of the material as thin film as well as their subsequent characterization. During the synthesis routes the student had the opportunity to tackle different equipment and techniques that are out of the knowledge domain of the physics background. This has allowed further improvement of the personal skills of the student as a researcher in a more general overview.

The behavior of PCPDTBT and PDTSBT, in the Langmuir trough as well as their electrical properties in LB films was investigated. Good transfer ratios were obtained for LB deposition from the mixed films with higher percentage of stearic acid, resulting in high quality and uniform films. The results show that it is possible to fabricate low-bandgap polymers by LB technique providing nanostructured films. The LB films of PCPDTBT showed higher electrical conductivities than the PDTSBT ones in the Au-IDE structure. The molecular architecture control of the films is relevant since it can affect some characteristics of organic electronic devices, such as electronic properties, as it was herein confirmed for the PCPDTBT and PDTSBT.

## COMPLEMENTARY INFORMATION

### Published and accepted papers

- a) M. L. Braunger, C. A. Escanhoela Jr., I. Fier, L. Walmsley, E. C. Ziemath, *Electrical conductivity of silicate glasses with tetravalent cations substituting Si*. **Journal of Non-Crystalline Solids**, 358, 2855-2861, 2012.
- b) P. Alessio, R. F. de Oliveira, P. H. B. Aoki, J. D. A. S. Pereira, M. L. Braunger, L. N. Furini, M. Vieira, S. R. Teixeira, A. E. Job, C. A. T. Saenz, N. Alves, C. A. Olivati, C. J. L. Constantino, *Molecular architecture and electrical properties in evaporated films of cobalt phthalocyanine*. **Journal of Nanoscience and Nanotechnology**, 12 (9), 7010-7020, 2012.
- c) M. L. Braunger, C. A. Escanhoela Jr., E. C. Ziemath, *Electrical conductivity of Ag-Na ion exchanged soda-lime glass*. **Solid State Ionics**, 265, 55-60, 2014.
- d) E. A. Silva, V. J. R. Oliveira, M. L. Braunger, C. J. L. Constantino, C. A. Olivati, *Poly(3-octylthiophene)/stearic acid Langmuir and Langmuir-Blodgett films: Preparation and characterization*. **Materials Research**, 17(6), 1442-1448, 2014.
- e) M. L. Braunger, A. Barros, M. Ferreira, C. A. Olivati, *Electrical and electrochemical measurements in nanostructured films of polythiophene derivatives*. **Electrochimica Acta**, 165, 1-6, 2015.
- f) P. Alessio, M. L. Braunger, R. F. Aroca, C. A. Olivati, C. J. L. Constantino, *Supramolecular organization-electrical properties relation in nanometric organic films*. **Journal of Physical Chemistry C**, 119, 12055-12064, 2015.
- g) J. D. Fernandes, P. H. B. Aoki, R. F. Aroca, W. D. Macedo Jr., S. R. Teixeira, M. L. Braunger, C. A. Olivati, C. J. L. Constantino, *Supramolecular architecture and electrical properties of a perylene derivative in physical vapor deposited films*. **Materials Research**, 2015.

### Submitted papers

- a) M. L. Braunger, P. Alessio, L. N. Furini, D. T. Balogh, C. J. L. Constantino, C. A. Olivati, *Influence of the supramolecular arrangement in the electrical conductivity of polythiophene thin films*. **Thin Solid Films**, 2015.

- b) E. C. Ziemath, C. A. Escanhoela Jr., M. L. Braunger, *Activation energies for the electrical conductivity of silicate glasses obtained by ac and dc techniques*. **Solid State Ionics**, 2015.
- c) M. L. Braunger, E. A. Silva, H. Awada, H. S. Silva, D. Bégué, R. C. Hiorns, C. Dagrón-Lartigau, C. A. Olivati, *Langmuir and Langmuir-Blodgett films of low-bandgap polymers*. **Surface and Coatings Technology**, 2015.
- d) L. V. L. Citolino, M. L. Braunger, V. J. R. Oliveira, C. A. Olivati. *Study of nanostructure effect on polyalkylthiophene derivatives films using impedance spectroscopy*. **Organic Electronics**, 2015.



## REFERENCES

1. Chauhan, A. & Saini, R. P. A review on integrated renewable energy system based power generation for stand-alone applications: Configurations, storage options, sizing methodologies and control. *Renew. Sustain. Energy Rev.* **38**, 99–120 (2014).
2. Etxebarria, I., Ajuria, J. & Pacios, R. Solution-processable polymeric solar cells: A review on materials, strategies and cell architectures to overcome 10%. *Org. Electron.* **19**, 34–60 (2015).
3. Green, M. A., Emery, K., Hishikawa, Y., Warta, W. & Dunlop, E. D. Solar cell efficiency tables (Version 45). *Prog. Photovoltaics Res. Appl.* **23**, 1–9 (2015).
4. Service, R. F. Outlook brightens for plastic solar cells. *Science* **332**, 293–293 (2011).
5. Gevorgyan, S. A., Jørgensen, M., Krebs, F. C. & Sylvester-Hvid, K. O. A compact multi-chamber setup for degradation and lifetime studies of organic solar cells. *Sol. Energy Mater. Sol. Cells* **95**, 1389–1397 (2011).
6. Traverse, C. J. *et al.* Efficient zinc sulfide cathode layers for organic photovoltaic applications via n-type doping. *J. Appl. Phys.* **115**, 1–5 (2014).
7. Kawata, S. *et al.* A morphology control layer of a pyrene dimer enhances the efficiency in small molecule organic photovoltaic cells. *J. Mater. Chem. C* **2**, 501–509 (2014).
8. Chen, H. *et al.* The role of fullerene mixing behavior in the performance of organic photovoltaics: PCBM in low-bandgap polymers. *Adv. Funct. Mater.* **24**, 140–150 (2014).
9. Clulow, A. J. *et al.* Determination of fullerene scattering length density: A critical parameter for understanding the fullerene distribution in bulk heterojunction organic photovoltaic devices. *Langmuir* (2014).
10. Bernardo, B. *et al.* Delocalization and dielectric screening of charge transfer states in organic photovoltaic cells. *Nat. Commun.* **5**, 1–7 (2014).
11. Wang, N., Tong, X., Burlingame, Q., Yu, J. & Forrest, S. R. Photodegradation of small-molecule organic photovoltaics. *Sol. Energy Mater. Sol. Cells* **125**, 170–175 (2014).
12. Kim, J.-H. *et al.* Fluorinated benzoselenadiazole-based low-band-gap polymers for high efficiency inverted single and tandem organic photovoltaic cells. *Macromolecules* (2014).
13. Awartani, O., Kudenov, M. W. & O'Connor, B. T. Organic photovoltaic cells with controlled polarization sensitivity. *Appl. Phys. Lett.* **104**, 1–5 (2014).
14. Griffith, O. L. & Forrest, S. R. Exciton management in organic photovoltaic multidonor energy cascades. *Nano Lett.* **14**, 2353–2358 (2014).

15. Kim, H., Lee, S., Han, D. & Yoo, S. High-density organic photovoltaic modules: Mask-free fabrication using nozzle jet printing and oblique deposition. *Sol. Energy Mater. Sol. Cells* **120**, 561–565 (2014).
16. Neophytou, M., Georgiou, E., Fyrrillas, M. M. & Choulis, S. A. Two step sintering process and metal grid design optimization for highly efficient ITO free organic photovoltaics. *Sol. Energy Mater. Sol. Cells* **122**, 1–7 (2014).
17. Truong, M. A. *et al.* Synthesis, characterization, and application to polymer solar cells of polythiophene derivatives with ester- or ketone-substituted phenyl side groups. *J. Polym. Sci. Part A Polym. Chem.* **53**, 875–887 (2015).
18. Wang, R. *et al.* Luminescent polythiophene-based main-chain polyoxometalate-containing conjugated polymers with improved solar-cell performance. *Eur. J. Inorg. Chem.* 656–663 (2015).
19. Yoon, C. O. *et al.* Hopping transport in doped conducting polymers in the insulating regime near the metal-insulator boundary: polypyrrole, polyaniline and polyalkylthiophenes. *Synth. Met.* **75**, 229–239 (1995).
20. Hummel, R. E. *Electronic properties of materials*. (Springer, 2011).
21. Brédas, J. L. & Street, G. B. Polarons, bipolarons, and solitons in conducting polymers. *Acc. Chem. Res.* **18**, 309–315 (1985).
22. Roncali, J. Conjugated poly(thiophenes): synthesis, functionalization, and applications. *Chem. Rev.* **92**, 711–738 (1992).
23. Olivati, C. A. *et al.* Polymer light emitting devices with Langmuir-Blodgett (LB) films: Enhanced performance due to an electron-injecting layer of ionomers. *Chem. Phys. Lett.* **408**, 31–36 (2005).
24. Kobayashi, T., Shinke, W., Nagase, T., Murakami, S. & Naito, H. Third-order optical susceptibility in polythiophene thin films prepared by spin-coating from high-boiling-point solvents. *Thin Solid Films* **554**, 106–109 (2014).
25. Lee, C., Hsu, C., Chen, I., Wu, W. & Lin, C. Percolation of carbon nanoparticles in poly(3-hexylthiophene) enhancing carrier mobility in organic thin film transistors. **2014**, 1–10 (2014).
26. Jayaraman, S., Yu, L. T. & Srinivasan, M. P. Polythiophene-gold nanoparticle hybrid systems: Langmuir-Blodgett assembly of nanostructured films. *Nanoscale* **5**, 2974–2982 (2013).
27. Takeoka, Y., Saito, F. & Rikukawa, M. Synthesis of optically active regioregular polythiophenes and their self-organization at the air-water interface. *Langmuir* **29**, 8718–8727 (2013).
28. Cimrová, V., Remmers, M., Neher, D. & Wegner, G. Polarized light emission from LEDs prepared by the Langmuir-Blodgett technique. *Adv. Mater.* **8**, 146–149 (1996).

29. Zasadzinski, J. A., Viswanathan, R., Madsen, L., Garnæs, J. & Schwartz, D. K. Langmuir-Blodgett films. *Science* **263**, 1726–1733 (1994).
30. Arslanov, V. V. Polymer monolayers and Langmuir-Blodgett films. Polythiophenes. *Russ. Chem. Rev.* **69**, 883–898 (2000).
31. Greve, D. R., Dynarowicz-Łatka, P., Dhanabalan, A. & Janssen, R. A. J. Langmuir film of regioregular poly(4-dodecyl-2,2'-bithiophene). *Colloids Surfaces A Physicochem. Eng. Asp.* **198-200**, 323–330 (2002).
32. Watanabe, I., Hong, K. & Rubner, M. Langmuir-Blodgett manipulation of poly(3-alkylthiophenes). *Langmuir* **6**, 1164–1172 (1990).
33. Bjørnholm, T., Hassenkam, T. & Reitzel, N. Supramolecular organization of highly conducting organic thin films by the Langmuir-Blodgett technique. *J. Mater. Chem.* **9**, 1975–1990 (1999).
34. Sanfelice, R. C., Gonçalves, V. C. & Balogh, D. T. Langmuir and Langmuir-Schaefer films of poly(3-hexylthiophene) with gold nanoparticles and gold nanoparticles capped with 1-octadecanethiol. *J. Phys. Chem. C* **118**, 12944–12951 (2014).
35. Reitzel, N. *et al.* Self-assembly of conjugated polymers at the air/water interface. Structure and properties of Langmuir and Langmuir-Blodgett films of amphiphilic regioregular polythiophenes. *J. Am. Chem. Soc.* **122**, 5788–5800 (2000).
36. Holmes, N. P. *et al.* The effect of polymer molecular weight on P3HT:PCBM nanoparticulate organic photovoltaic device performance. *Sol. Energy Mater. Sol. Cells* **128**, 369–377 (2014).
37. Chen, H., Peet, J., Hsiao, Y. C., Hu, B. & Dadmun, M. The impact of fullerene structure on its miscibility with P3HT and its correlation of performance in organic photovoltaics. *Chem. Mater.* (2014).
38. Yang, Q. *et al.* Improved performance of P3HT:PCBM photovoltaic devices with ITO treated by hydrogen peroxide. *J. Nanosci. Nanotechnol.* **14**, 3407–3411 (2014).
39. Hiorns, R. C. *et al.* High molecular weights, polydispersities, and annealing temperatures in the optimization of bulk-heterojunction photovoltaic cells based on poly(3-hexylthiophene) or poly(3-butylthiophene). *Adv. Funct. Mater.* **16**, 2263–2273 (2006).
40. Dennler, G., Scharber, M. C. & Brabec, C. J. Polymer-fullerene bulk-heterojunction solar cells. *Adv. Mater.* **21**, 1323–1338 (2009).
41. Scharber, M. C. *et al.* Influence of the bridging atom on the performance of a low-bandgap bulk heterojunction solar cell. *Adv. Mater.* **22**, 367–370 (2010).
42. Coffin, R. C., Peet, J., Rogers, J. & Bazan, G. C. Streamlined microwave-assisted preparation of narrow-bandgap conjugated polymers for high-performance bulk heterojunction solar cells. *Nat. Chem.* **1**, 657–661 (2009).

43. Huo, L., Chen, H.-Y., Hou, J., Chen, T. L. & Yang, Y. Low band gap dithieno[3,2-b:2',3'-d]silole-containing polymers, synthesis, characterization and photovoltaic application. *Chem. Commun.* 5570–5572 (2009).
44. Kaiser, A. B. Systematic conductivity behavior in conducting polymers: Effects of heterogeneous disorder. **13**, 927–941 (2001).
45. Pope, M. & Swenberg, C. E. *Electronic process in organic crystals and polymers*. (Oxford University Press, 1999).
46. Chiang, C. K. *et al.* Electrical conductivity in doped polyacetylene. *Phys. Rev. Lett.* **39**, 1098–1101 (1977).
47. Nicolini, C. & Narizzano, R. New materials by organic nanotechnology and their applications. *Recent Res. Dev. Mater. Sci.* **6**, 1–24 (2005).
48. Wan, M. *Conducting polymers with micro or nanometer structure*. (Tsinghua University Press and Springer, 2008).
49. Heeger, A. J., Kivelson, S., Schrieffer, J. R. & Su, W.-P. Solitons in conducting polymers. *Rev. Mod. Phys.* **60**, 781–850 (1988).
50. Heeger, A. J. & Pethig, R. Charge storage and charge transport in conducting polymers: solitons, polarons and bipolarons [and discussion]. *Philos. Trans. R. Soc. A Math. Phys. Eng. Sci.* **314**, 17–35 (1985).
51. Nabok, A. *Organic and inorganic nanostructures*. (Artech House, 2005).
52. *Introduction to nanoscale science and technology*. Ventra, M. D., Evoy, S., Heflin Jr., J. R., **7**, (Kluwer Academic Publishers, 2004).
53. Manasreh, O. *Semiconductor heterojunctions and nanostructures*. (McGraw-Hill, 2005).
54. *Handbook of conducting polymers - Conjugated polymers: theory, synthesis, properties, and characterization*. Skotheim, T. A., Reynolds, J. R. (CRC press, 2007).
55. Wang, H. & Nann, T. *Springer Series on Fluorescence. Upconverting Nanoparticles 7*, (Springer-Verlag, 2008).
56. *Practical handbook of photovoltaics: fundamentals and applications*. Markvart, T., Castañer, L. (Elsevier, 2003).
57. Tang, C. W. Two-layer organic photovoltaic cell. *Appl. Phys. Lett.* **48**, 183–185 (1986).
58. *Organic Photovoltaics - Concepts and Realization*. Brabec, C. J., Dyakonov, V., Parisi, J., Sariciftci, N. S. (Springer, 2003).
59. Yang, F., Shtein, M. & Forrest, S. R. Controlled growth of a molecular bulk heterojunction photovoltaic cell. *Nat. Mater.* **4**, 37–41 (2005).

60. Kaur, N., Singh, M., Pathak, D., Wagner, T. & Nunzi, J. M. Organic materials for photovoltaic applications: Review and mechanism. *Synth. Met.* **190**, 20–26 (2014).
61. Luque, A. & Hegedus, S. *Handbook of photovoltaic science and engineering*. (John Wiley & Sons, 2003).
62. *Electrical characterization of photovoltaic materials and solar cells with the model 4200-SCS semiconductor characterization system*. Application note (Keithley Instruments, Inc., 2011).
63. Peumans, P. & Forrest, S. R. Very-high-efficiency double-heterostructure copper phthalocyanine/C60 photovoltaic cells. *Appl. Phys. Lett.* **79**, 126–128 (2001).
64. Elumalai, N. K. *et al.* Effect of C60 as an electron buffer layer in polythiophene-methanofullerene based bulk heterojunction solar cells. *Phys. Status Solidi A* **209**, 1592–1597 (2012).
65. Zhao, G., He, Y. & Li, Y. 6.5% efficiency of polymer solar cells based on poly(3-hexylthiophene) and indene-C60 bisadduct by device optimization. *Adv. Mater.* **22**, 4355–4358 (2010).
66. Oklobia, O. & Shafai, T. S. A study of donor/acceptor interfaces in a blend of P3HT/PCBM solar cell: Effects of annealing and PCBM loading on optical and electrical properties. *Solid. State. Electron.* **87**, 64–68 (2013).
67. Sigma-Aldrich. at <<http://www.sigmaaldrich.com/>>
68. You, J. *et al.* A polymer tandem solar cell with 10.6% power conversion efficiency. *Nat. Commun.* **4**, 1–10 (2013).
69. Mühlbacher, D. *et al.* High photovoltaic performance of a low-bandgap polymer. *Adv. Mater.* **18**, 2884–2889 (2006).
70. Medlej, H. *et al.* Effect of spacer insertion in a commonly used dithienosilole/benzothiadiazole-based low band gap copolymer for polymer solar cells. *Eur. Polym. J.* **49**, 4176–4188 (2013).
71. Chen, C.-H., Hsieh, C.-H., Dubosc, M., Cheng, Y.-J. & Hsu, C.-S. Synthesis and characterization of bridged bithiophene-based conjugated polymers for photovoltaic applications: Acceptor strength and ternary blends. *Macromolecules* **43**, 697–708 (2010).
72. Pal, B. *et al.* Substituent effect on the optoelectronic properties of alternating fluorene-cyclopentadithiophene copolymers. *Macromolecules* **41**, 6664–6671 (2008).
73. Brzezinski, J. Z. & Reynolds, J. R. A new, improved and convenient synthesis of 4H-cyclopenta[2,1-b:3,4-b']-dithiophen-4-one. *Synthesis (Stuttg)*. 1053–1056 (2002).

74. Lambert, J. B. & Mazzola, E. P. *Nuclear magnetic resonance spectroscopy: an introduction to principles, applications, and experimental methods*. (Pearson Education Inc., 2004).
75. Hiorns, R. C. *et al.* A brief guide to polymer nomenclature (IUPAC Technical Report). *Pure Appl. Chem.* **84**, 2167–2169 (2012).
76. *Prominence gel permeation chromatography system*. Application note (Shimadzu Corporation).
77. *An introduction to gel permeation chromatography and size exclusion chromatography*. Application note (Agilent Technologies, Inc., 2014).
78. *Thermogravimetric analysis (TGA)*. A beginner's guide (PerkinElmer, Inc., 2010). at <www.perkinelmer.com>
79. Elmer, P. *Differential Scanning Calorimetry (DSC)*. A beginner's guide (PerkinElmer, Inc., 2013). at <www.perkinelmer.com>
80. Volpati, D. *et al.* Physical vapor deposited thin films of lignins extracted from sugar cane bagasse: morphology, electrical properties, and sensing applications. *Biomacromolecules* **12**, 3223–3231 (2011).
81. Alessio, P. *et al.* Molecular Architecture and Electrical Properties in Evaporated Films of Cobalt Phthalocyanine. *J. Nanosci. Nanotechnol.* **12**, 7010–7020 (2012).
82. *Functional thin films and nanostructures for sensors: synthesis, physics, and applications*. (Springer, 2009).
83. Pethrick, R. A. *Polymer structure characterization - from nano to macro organization*. (The Royal Society of Chemistry, 2007).
84. Mattoso, L. H. C., Ferreira, M. & Oliveira Jr., O. N. Filmes Langmuir-Blodgett de polímeros condutores. *Polímeros Ciência e Tecnol.* 23–34 (1994).
85. *Basic experiments for KSV Langmuir and Langmuir-Blodgett instruments*. KSV Monolayer Kit (KSV Instruments).
86. *KSV 5000 Instruction Manual*. 130 (KSV Instruments LTD, 2001).
87. Nunes, B. M. Fabricação e caracterização de filmes Langmuir e Langmuir-Blodgett de derivados do politiofeno. (2012).
88. *Langmuir and Langmuir-Blodgett films - What and How?* Application Note **107**, (KSV Instruments LTD, 2011).
89. Nicholson, P. G., Ruiz, V., Macpherson, J. V & Unwin, P. R. Effect of composition on the conductivity and morphology of poly(3-hexylthiophene)/gold nanoparticle composite Langmuir-Schaeffer films. *Phys. Chem. Chem. Phys.* **8**, 5096–5105 (2006).

90. Koh, S. E. *et al.* Phenylphosphonic acid functionalization of indium tin oxide: Surface chemistry and work functions. *Langmuir* **22**, 6249–6255 (2006).
91. Sharma, A. *et al.* Effects of surface modification of indium tin oxide electrodes on the performance of molecular multilayer organic photovoltaic devices. *J. Mater. Chem.* **19**, 5298–5302 (2009).
92. *Handbook of deposition technologies for films and coatings - Science, technology and applications*. Bunshah, R. F. (1994).
93. *KSV NIMA Brewster Angle Microscopes*. Brochure (KSV NIMA).
94. Gary D. Christian. *Analytical Chemistry*. (John Wiley & Sons, Inc., 2004).
95. F. J. Holler, D. A. Skoog, S. R. C. *Princípios de Análise Instrumental*. (Bookman, 2009).
96. Harris, D. C. *Análise Química Quantitativa*. (Livros Técnicos e Científicos, 2011).
97. Binnig, G., Quate, C. F. & Gerber, C. Atomic force microscope. *Phys. Rev. Lett.* **56**, 930–933 (1986).
98. *Nanosurf easyScan 2 AFM: operating instructions for SPM control software version 3.0*. (Nanosurf AG, 2011).
99. *Dektak 8 advanced development profiler manual*. (Veeco Instruments, Inc., 2004).
100. *Dektak 150+ Surface Profiler: high-performance, versatility and value*. Brochure (Veeco Instruments, Inc., 2008).
101. Skoog, D. A., West, D. M., Holler, F. J. & Crouch, S. R. *Fundamentos de Química Analítica*. (Cengage Learning, 2006).
102. Barsoukov, E. & Macdonald, J. R. *Impedance Spectroscopy - theory, experiment, and applications*. (John Wiley & Sons, Inc., 2005).
103. *1260 Impedance/Gain-Phase Analyzer*. Operating manual (Solartron Analytical, 1996).
104. *Gamry Instruments Software - Tutorials and Primers*. (Gamry Instruments, Inc., 2005).
105. *Nanotechnology measurement handbook: A guide to electrical measurements for nanoscience applications*. (Keithley Instruments, Inc., 2007). at <[http://www.keithley.com.cn/knowledgecenter/knowledgecenter\\_pdf/NanotchMsHandbk\\_1.pdf](http://www.keithley.com.cn/knowledgecenter/knowledgecenter_pdf/NanotchMsHandbk_1.pdf)>
106. *Low level measurements handbook - Precision DC current, voltage, and resistance measurements*. (Keithley Instruments, Inc., 2004).
107. *Keithley Model 236/237/238 Source Measure Units: Operator's manual*. (Keithley Instruments, Inc., 2001).

108. Olthuis, W., Streekstra, W. & Bergveld, P. Theoretical and experimental determination of cell constants of planar-interdigitated electrolyte conductivity sensors. *Sensors Actuators B* **24-25**, 252–256 (1995).
109. Dantas, C. A. R. Fabricação de microcanais para integração de uma ‘língua eletrônica’ em um sistema lab-on-a-chip. (2009).
110. *Microfabrication and Nanomanufacturing*. (CRC Press - Taylor & Francis Group, 2006).
111. Li, G., Zhu, R. & Yang, Y. Polymer solar cells. *Nat. Photonics* **6**, 153–161 (2012).
112. Garcia-Basabe, Y. *et al.* Electronic structure, molecular orientation, charge transfer dynamics and solar cells performance in donor/acceptor copolymers and fullerene: experimental and theoretical approaches. *J. Appl. Phys.* **115**, 1–7 (2014).
113. Tumay, A. & Tore, N. Efficiency improvement of PCDTBT solar cells with silver nanoparticles. *Sol. Energy Mater. Sol. Cells* **110**, 58–62 (2013).
114. Brabec, C. J., Shaheen, S. E., Winder, C., Sariciftci, N. S. & Denk, P. Effect of LiF/metal electrodes on the performance of plastic solar cells. *Appl. Phys. Lett.* **80**, 1288–1290 (2002).
115. Yanagitate, T. *et al.* Flexible PTB7:PC71BM bulk heterojunction solar cells with a LiF buffer layer. *Jpn. J. Appl. Phys.* **53**, 1–5 (2014).
116. Yli-Lahti, P., Punkka, E., Stubb, H., Kuivalainen, P. & Laakso, J. Conductive Langmuir-Blodgett multilayer films of poly(3-octylthiophene). *Thin Solid Films* **179**, 221–224 (1989).
117. Callender, C. L., Carere, C. A., Daoust, G. & Leclerc, M. Langmuir-Blodgett processing of poly(3,4-dibutoxythiophene). *Thin Solid Films* **204**, 451–457 (1991).
118. Olivati, C. A., Gonçalves, V. C. & Balogh, D. T. Optically anisotropic and photoconducting Langmuir-Blodgett films of neat poly(3-hexylthiophene). *Thin Solid Films* **520**, 2208–2210 (2012).
119. Dicker, G. *et al.* Photoconductivity enhancement of poly(3-hexylthiophene) by increasing inter- and intra-chain order. *Synth. Met.* **137**, 863–864 (2003).
120. Gonçalves, V. C. & Balogh, D. T. Optical chemical sensors using polythiophene derivatives as active layer for detection of volatile organic compounds. *Sensors Actuators B Chem.* **162**, 307–312 (2012).
121. McCullough, R. D., Lowe, R. D., Jayaraman, M. & Anderson, D. L. Design, synthesis, and control of conducting polymer architectures: structurally homogeneous poly(3-alkylthiophenes). *J. Org. Chem.* **58**, 904–912 (1993).
122. Brown, P. *et al.* Effect of interchain interactions on the absorption and emission of poly(3-hexylthiophene). *Phys. Rev. B* **67**, 1–16 (2003).



123. Trznadel, M., Pron, A., Zagorska, M., Chrzaszcz, R. & Pielichowski, J. Effect of molecular weight on spectroscopic and spectroelectrochemical properties of regioregular poly(3-hexylthiophene). *Macromolecules* **31**, 5051–5058 (1998).
124. Rughooputh, S. D. D. V., Hotta, S., Heeger, A. J. & Wudl, F. Chromism of soluble polythienylenes. *J. Polym. Sci. Part B Polym. Phys.* **25**, 1071–1078 (1987).
125. Inganäs, O., Gustafsson, G., Salaneck, W. R., Österholm, J. E. & Laakso, J. Thermochromism in thin films of poly(3-alkylthiophenes). *Synth. Met.* **28**, 377–384 (1989).
126. Sundberg, M., Inganäs, O., Stafström, S., Gustafsson, G. & Sjögren, B. Optical absorption of poly(3-alkylthiophenes) at low temperatures. *Solid State Commun.* **71**, 435–439 (1989).
127. Kanai, K. *et al.* Effect of annealing on the electronic structure of poly (3-hexylthiophene) thin film. *Phys. Chem. Chem. Phys.* **12**, 273–282 (2010).
128. Rikukawa, M. *et al.* Electrical properties of conductive Langmuir-Blodgett films comprised of head-to-tail poly(3-hexylthiophene). *Thin Solid Films* **284-285**, 636–639 (1996).
129. Xu, B. & Holdcroft, S. Molecular control of luminescence from poly(3-hexylthiophenes). *Macromolecules* **26**, 4457–4460 (1993).
130. Abdou, M. S. A., Orfino, F. P., Son, Y. & Holdcroft, S. Interaction of oxygen with conjugated polymers: charge transfer complex formation with poly (3-alkylthiophenes). *J. Am. Chem. Soc.* **119**, 4518–4524 (1997).
131. Ahn, H., Oblas, D. & Whitten, J. Electron irradiation of poly (3-hexylthiophene) films. *Macromolecules* **37**, 3381–3387 (2004).
132. Clark, J., Silva, C., Friend, R. & Spano, F. Role of intermolecular coupling in the photophysics of disordered organic semiconductors: aggregate emission in regioregular polythiophene. *Phys. Rev. Lett.* **98**, 1–4 (2007).
133. Spano, F. C., Clark, J., Silva, C. & Friend, R. H. Determining exciton coherence from the photoluminescence spectral line shape in poly(3-hexylthiophene) thin films. *J. Chem. Phys.* **130**, 1–16 (2009).
134. Prosa, T. J., Winokur, M. J., Moulton, J., Smith, P. & Heeger, A. J. X-ray structural studies of poly(3-alkylthiophenes): an example of an inverse comb. *Macromolecules* **25**, 4364–4372 (1992).
135. Gangopadhyay, P. *et al.* Faraday rotation measurements on thin films of regioregular alkyl-substituted polythiophene derivatives. *J. Phys. Chem. C* **112**, 8032–8037 (2008).
136. Clark, J., Chang, J.-F., Spano, F. C., Friend, R. H. & Silva, C. Determining exciton bandwidth and film microstructure in polythiophene films using linear absorption spectroscopy. *Appl. Phys. Lett.* **94**, 1–4 (2009).

137. Ferreira, M. *et al.* Langmuir and Langmuir-Blodgett films of poly[2-methoxy-5-(n-hexyloxy)-p-phenylenevinylene]. *Langmuir* **19**, 8835–8842 (2003).
138. Rubinger, C. P. L. *et al.* Langmuir-Blodgett and Langmuir-Schaefer films of poly(5-amino-1-naphthol) conjugated polymer. *Appl. Surf. Sci.* **253**, 543–548 (2006).
139. Sze, S. M. & Ng, K. K. *Physics of semiconductor devices*. (John Wiley & Sons, 2007).
140. Roncali, J. *et al.* Effects of steric factors on the electrosynthesis and properties of conducting poly(3-alkylthiophenes). *J. Phys. Chem.* **91**, 6706–6714 (1987).
141. Leclerc, M. & Faid, K. Electrical and optical properties of processable polythiophene derivatives: structure-property relationships. *Adv. Mater.* **9**, 1087–1094 (1997).
142. Benincori, T. *et al.* Steric control of conductivity in highly conjugated polythiophenes. *Chem. Mater.* **13**, 1665–1673 (2001).
143. Singh, R. K. *et al.* Micromorphology, photophysical and electrical properties of pristine and ferric chloride doped poly(3-hexylthiophene) films. *Mater. Chem. Phys.* **104**, 390–396 (2007).
144. Kumar, J. *et al.* Dc electrical conduction and morphology of poly(3-octylthiophene) films. *J. Phys. D: Appl. Phys.* **39**, 196–202 (2006).
145. Chen, T.-A. & Rieke, R. D. Short communication polyalkylthiophenes with the smallest bandgap and the highest intrinsic conductivity. *Synth. Met.* **60**, 175–177 (1993).
146. Chen, T.-A., Wu, X. & Rieke, R. D. Regiocontrolled synthesis of poly(3-alkylthiophenes) mediated by Rieke zinc: their characterization and solid-state properties. *J. Am. Chem. Soc.* **117**, 233–244 (1995).
147. Hudej, R., Zavrtanik, M., Brownell, J. N. & Bratina, G. Electrical conductivity in 3,4,9,10-perylenetetracarboxylic dianhydride (PTCDA). *Mater. Tehnol.* **35**, 151–155 (2001).
148. Rybak, A., Pisula, W., Jung, J. & Ulanski, J. Influence of molecular order on charge carrier photogeneration in perylene derivative layer. *Thin Solid Films* **516**, 4201–4207 (2008).
149. Vardeny, Z. *et al.* Photogeneration of confined soliton pairs (bipolarons) in polythiophene. *Phys. Rev. Lett.* **56**, 671–674 (1986).
150. Lee, C. H., Yu, G. & Heeger, A. J. Persistent photoconductivity in poly(p-phenylenevinylene): Spectral response and slow relaxation. *Phys. Rev. B* **47**, 15543–15553 (1993).
151. Ujimoto, M., Takashima, W. & Kaneto, K. Photo induced memory devices using conducting polymer, poly(3-hexylthiophene) thin films. *Thin Solid Films* **499**, 313–317 (2006).

152. Karan, S., Basak, D. & Mallik, B. Persistence in photoconductivity and optical property of nanostructured copper (II) phthalocyanine thin films. *Curr. Appl. Phys.* **10**, 1117–1122 (2010).
153. Reitz, J. R., Milford, F. J. & Christy, R. W. *Fundamentos da Teoria Eletromagnética*. (Campus, 1982).
154. Tomozawa, H. *et al.* Metal-polymer schottky barriers on processible polymers. *Synth. Met.* **28**, 687–690 (1989).
155. Spicer, W. E., Lindau, I., Skeath, P., Su, C. Y. & Chye, P. Unified mechanism for Schottky-barrier formation and III-V oxide interface states. *Phys. Rev. Lett.* **44**, 420–423 (1980).
156. Zoppi, R. A. & De Paoli, M.-A. Aplicações tecnológicas de polímeros intrinsecamente condutores: perspectivas atuais. *Quim. Nova* **16**, 560–569 (1993).
157. Braunger, M. L., Barros, A., Ferreira, M. & Olivati, C. A. Electrical and electrochemical measurements in nanostructured films of polythiophene derivatives. *Electrochim. Acta* **165**, 1–6 (2015).
158. Park, J., Kim, H. M., Kim, D. W. & Choi, J. S. Effects of gate electrode work function on electrical characteristics of pentacene-based field-effect devices. *Appl. Phys. Lett.* **97**, 1–3 (2010).
159. Horowitz, G. *et al.* Evidence for n-type conduction in a perylene tetracarboxylic diimide derivative. *Adv. Mater.* **8**, 242–245 (1996).
160. Zhan, C.-G., Nichols, J. A. & Dixon, D. A. Ionization potential, electron affinity, electronegativity, hardness, and electron excitation energy: molecular properties from density functional theory orbital energies. *J. Phys. Chem. A* **107**, 4184–4195 (2003).
161. Micaroni, L., Nart, F. C. & Hümmelgen, I. A. Considerations about the electrochemical estimation of the ionization potential of conducting polymers. *J. Solid State Electrochem.* **7**, 55–59 (2002).
162. Dissanayake, D. M. N. M., Lutz, T., Curry, R. J. & Silva, S. R. P. Measurement and validation of PbS nanocrystal energy levels. *Appl. Phys. Lett.* **93**, 1–3 (2008).
163. Ji, Y. *et al.* Synthesis and electrochromic properties of polybismaleimides containing triphenylamine units. *J. Solid State Electrochem.* **18**, 1537–1544 (2014).
164. Duan, C. *et al.* Novel silafluorene-based conjugated polymers with pendant acceptor groups for high performance solar cells. *Macromolecules* **43**, 5262–5268 (2010).
165. Fung, D. D. S. & Choy, W. C. H. *Organic solar cells: materials and device physics*. *Org. Sol. Cells* (Springer-Verlag, 2013).
166. Eckhardt, H., Shacklette, L. W., Jen, K. Y. & Elsenbaumer, R. L. The electronic and electrochemical properties of poly(phenylene vinylenes) and poly(thienylene

- vinylenes): An experimental and theoretical study. *J. Chem. Phys.* **91**, 1303–1315 (1989).
167. Alkan, S., Cutler, C. A. & Reynolds, J. R. High quality electrochromic polythiophenes via BF<sub>3</sub>.Et<sub>2</sub>O electropolymerization. *Adv. Funct. Mater.* **13**, 331–336 (2003).
  168. Son, S., Dodabalapur, A., Lovinger, A. J. & Galvin, M. E. Luminescence enhancement by the introduction of disorder into poly(p-phenylene vinylene). *Science (80-. )*. **269**, 376–378 (1995).
  169. Olivati, C. A. *et al.* Anisotropy in the optical properties of oriented Langmuir-Blodgett films of OC1OC6-PPV. *Chem. Phys. Lett.* **381**, 404–409 (2003).
  170. Crespilho, F. N. *et al.* Using electrochemical data to obtain energy diagrams for layer-by-layer films from metallic phthalocyanines. *Int. J. Electrochem. Sci.* **1**, 151–159 (2006).
  171. Khan, M. A. *et al.* Electron injection and transport mechanism in organic devices based on electron transport materials. *J. Phys. D: Appl. Phys.* **41**, 225105(1–6) (2008).
  172. Steyrlleuthner, R. *et al.* Bulk electron transport and charge injection in a high mobility n-type semiconducting polymer. *Adv. Mater.* **22**, 2799–2803 (2010).
  173. Somani, P. R. & Radhakrishnan, S. Electrochromic materials and devices: present and future. *Mater. Chem. Phys.* **77**, 117–133 (2002).
  174. Diaz, A. F., Castillo, J. I., Logan, J. A. & Lee, W.-Y. Electrochemistry of conducting polypyrrole films. *J. Electroanal. Chem. Interfacial Electrochem.* **129**, 115–132 (1981).
  175. Waltman, R. J., Bargon, J. & Diaz, A. F. Electrochemical studies of some conducting polythiophene films. *J. Phys. Chem.* **87**, 1459–1463 (1983).
  176. Mortimer, R. J. Electrochromic materials. *Chem. Soc. Rev.* **26**, 147–156 (1997).
  177. Zotti, G. & Schiavon, G. The polythiophene puzzle. Electrochemical and spectroelectrochemical evidence for two oxidation levels. *Synth. Met.* **31**, 347–357 (1989).
  178. Chen, J., Heeger, A. J. & Wudl, F. Confined soliton pairs (bipolarons) in polythiophene: in-situ magnetic resonance measurements. *Solid State Commun.* **58**, 251–257 (1986).
  179. Hyodo, K. Electrochromism of conducting polymers. *Electrochim. Acta* **39**, 265–272 (1994).
  180. Chen, C.-C. *et al.* Impedance spectroscopy and equivalent circuits of conductively doped organic hole-transport materials. *Org. Electron.* **11**, 1901–1908 (2010).

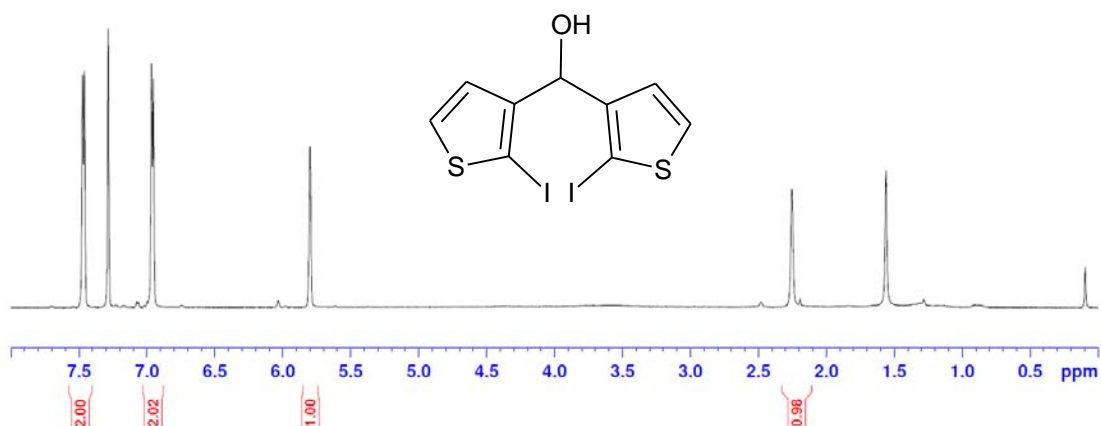
181. Lange, U. & Mirsky, V. M. Separated analysis of bulk and contact resistance of conducting polymers: Comparison of simultaneous two- and four-point measurements with impedance measurements. *J. Electroanal. Chem.* **622**, 246–251 (2008).
182. Salleo, A. Charge transport in polymeric transistors. *Mater. Today* **10**, 38–45 (2007).
183. Kline, R. J., McGehee, M. D., Kadnikova, E. N., Liu, J. & Fréchet, J. M. J. Controlling the field-effect mobility of regioregular polythiophene by changing the molecular weight. *Adv. Mater.* **15**, 1519–1522 (2003).
184. Petty, M. C. *Langmuir-Blodgett films - An introduction*. (Cambridge University Press, 1996).
185. Paloheimo, J., Kuivalainen, P., Stubb, H., Vuorimaa, E. & Yli-Lahti, P. Molecular field-effect transistors using conducting polymer Langmuir-Blodgett films. *Appl. Phys. Lett.* **56**, 1157–1159 (1990).
186. Hoppe, H. & Sariciftci, N. S. Organic solar cells: An overview. *J. Mater. Res.* **19**, 1924–1945 (2004).
187. Kawano, K. *et al.* Degradation of organic solar cells due to air exposure. *Sol. Energy Mater. Sol. Cells* **90**, 3520–3530 (2006).
188. Celik, D. *et al.* Performance enhancement of CdSe nanorod-polymer based hybrid solar cells utilizing a novel combination of post-synthetic nanoparticle surface treatments. *Sol. Energy Mater. Sol. Cells* **98**, 433–440 (2012).
189. Waters, H. *et al.* Effect of processing additive 1,8-octanedithiol on the lifetime of PCPDTBT based organic photovoltaics. *Org. Electron.* **15**, 2433–2438 (2014).

## APPENDIX

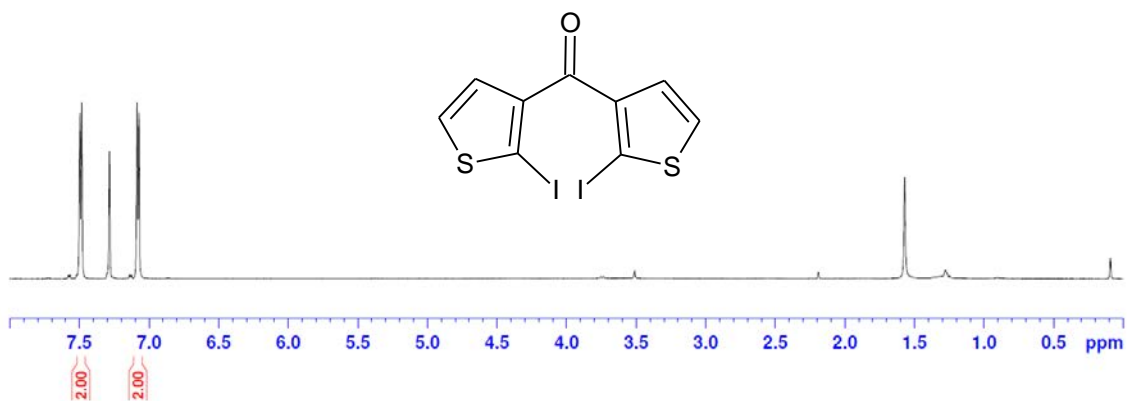
**Monomer synthesis: NMR spectra**

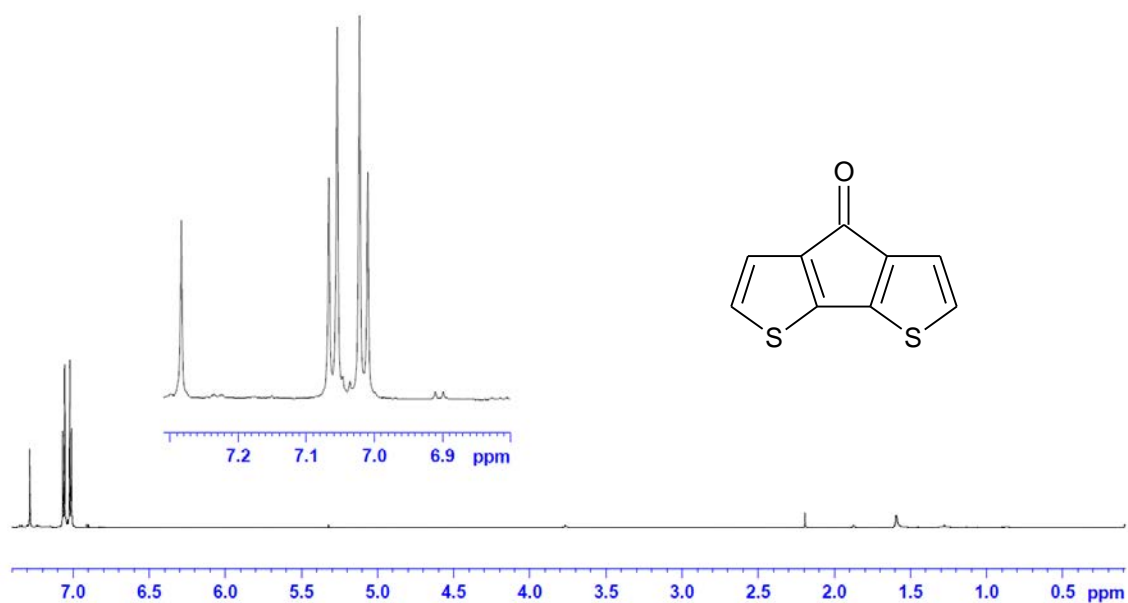
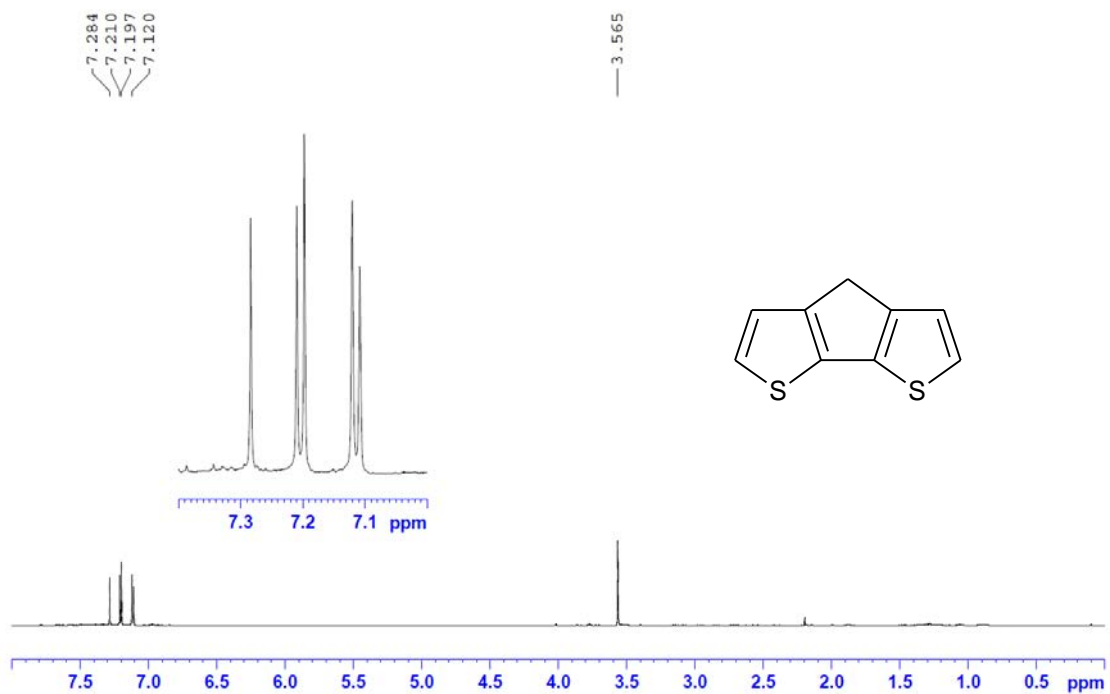
In this section, the NMR spectra obtained for each step during the synthesis route of the CPDT monomer with branched chains derivative are presented. The results were not discussed in this section once it was not the focus of this PhD thesis. The spectra were compared with the ones in the literature (mentioned in the section 2.3.1. of this thesis) in order to verify the success of each chemical reaction.

(a) and (b) *Bis(2-iodo-3-thienyl)methanol*

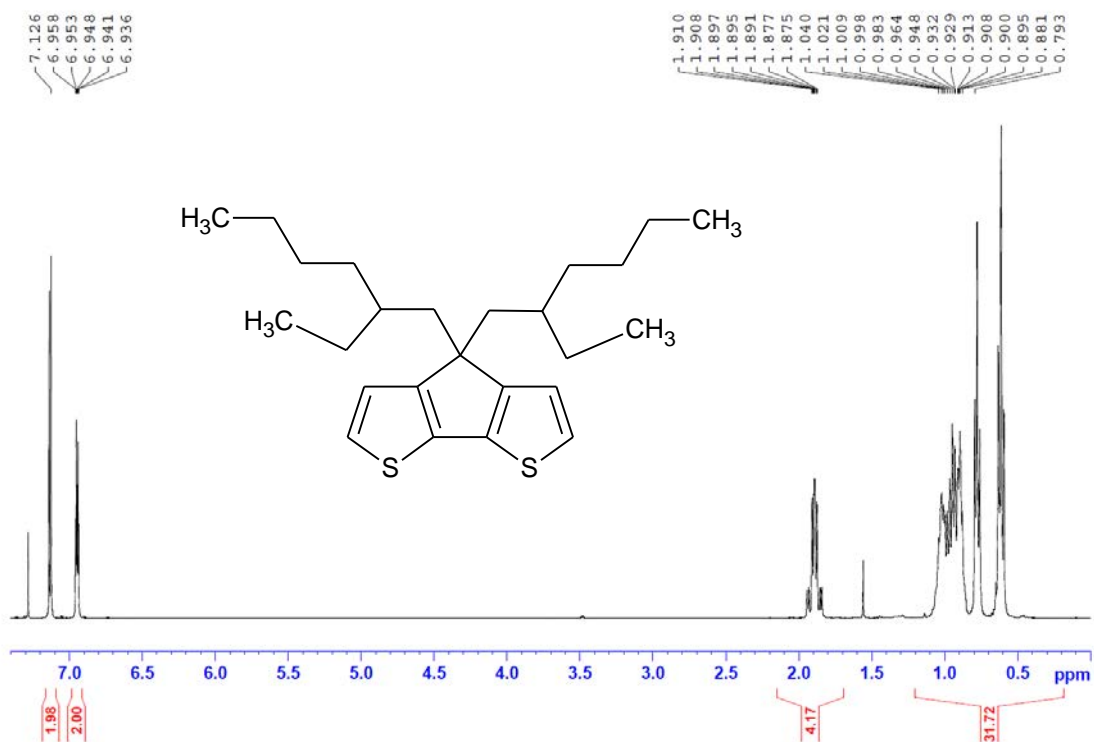


(c) *Bis(2-iodo-3-thienyl)ketone*

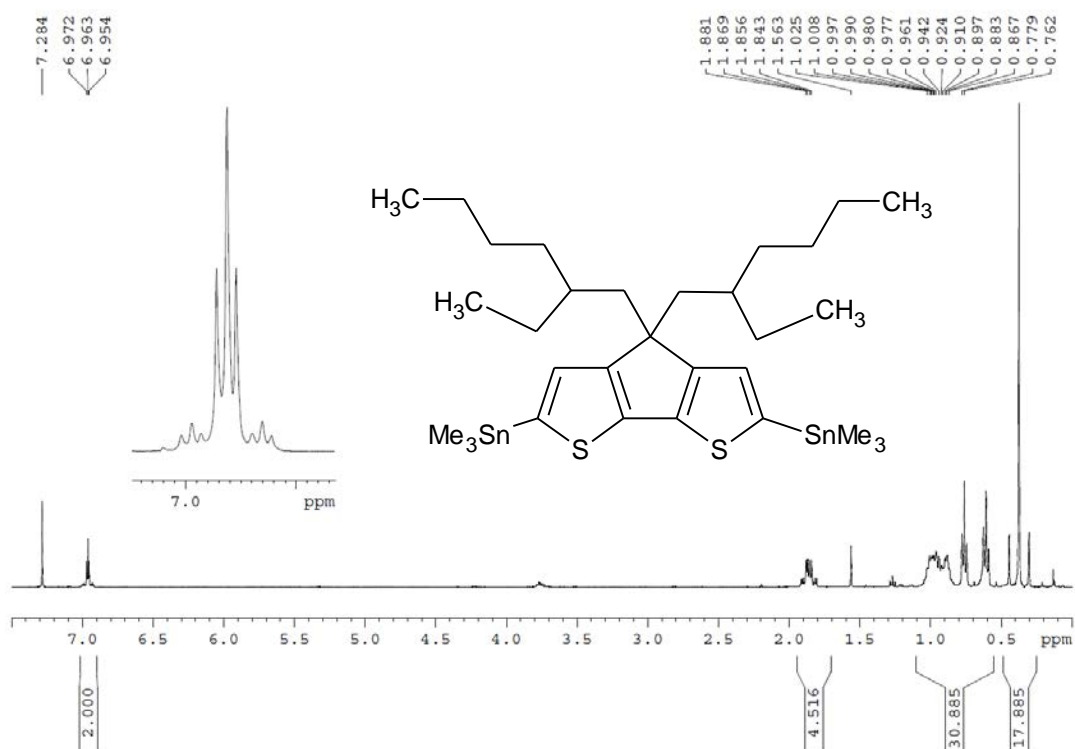


(d) 4*H*-cyclopenta-[2,1-*b*:3,4-*b'*]dithiophen-4-one(e) 4*H*-cyclopenta[2,1-*b*:3,4-*b'*]dithiophene

(f) 4,4-bis(2-ethylhexyl)-4H-cyclopenta[2,1-b:3,4-b']dithiophene



(g) 4,4-bis(2-ethylhexyl)-2,6-bis(trimethylstannyl)-4H-cyclopenta[2,1-b:3,4-b']dithiophene





ECOLE DOCTORALE :  
Sciences Exactes et leurs applications

LABORATOIRE :  
Equipe de Physique et Chimie des Polymères

MARIA LUISA BRAUNGER